Fall 12-17-2016

# A Visual Velocity Impedance Controller

Victor Nevarez

## Recommended Citation

Nevarez, Victor. "A Visual Velocity Impedance Controller." (2016). https://digitalrepository.unm.edu/me_etds/112

Victor Nevarez

*Candidate*

Mechanical Engineering

*Department*

This thesis is approved, and it is acceptable in quality and form for publication:

*Approved by the Thesis Committee:*

Dr. Ron Lumia, Chairperson

Dr. Rafael Fierro

Dr. Joseph Bishop

# A Visual Velocity Impedance Controller

by

**Victor Nevarez**

Bachelors of Science, Mechanical Engineering,
Massachusetts Institute of Technology, 2012

THESIS

Submitted in Partial Fulfillment of the
Requirements for the Degree of

Master of Science
Mechanical Engineering

The University of New Mexico

Albuquerque, New Mexico

December, 2016

# Dedication

*This work is dedicated to my parents and to Johanna Chong. Without them I doubt I would have ever come this far or pushed myself as much as I have. As much as I have struggled they have always been there to help me out and helped me push through.*

# Acknowledgments

I would like the thank everyone who helped in contributing the writing of this thesis. First of all, Dr. Ron Lumia for advising me through all these years and providing me with the invaluable research experiences over the years. More than any classes I have taken at UNM, the research experience and valuable lessons that Professor Lumia has given me are the most important things I have taken from the graduate program. I would like to thank my committee members, Dr. Rafael Fierro and Dr. Joseph Bishop, for everything they have taught me and for taking time to review this work.

I would like to thank Dave Vick for showing me how to use the various robots in the High Bay Area. I would also like to thank Tim Blada for showing me how to use the WAM's and for getting me started on making my own controller for the WAM. Without the work provided by time I would not have been able to finish this work at all.

Finally, I would like to thank my mom, dad, sister, and Johanna for all their support. Without them keeping me accountable I fear to think how much longer this work would have taken to finish.

# A Visual Velocity Impedance Controller

by

**Victor Nevarez**

Bachelors of Science, Mechanical Engineering,
Massachusetts Institute of Technology, 2012

M.S., Mechanical Engineering, University of New Mexico, 2016

## Abstract

Successful object insertion systems allow the object to translate and rotate to accommodate contact forces. Compliant controllers are used in robotics to provide this accommodation. The impedance compliant controller is one of the more researched and well known compliant controllers used for assembly. The velocity filtered visual impedance controller is introduced as a compliant controller to improve upon the impedance controller. The velocity filtered impedance controller introduces a filter of the velocity impedance and a gain from the stiffness. The velocity impedance controller was found to be more stable over larger ranges of stiffness values than the position based impedance controller. This led to the velocity impedance controller being more accurate and stable with respect to external forces. The velocity impedance controller was also found to have a better compliant response when tested on various insertion geometries in various configurations, including a key insertion acting against gravity. Finally, a novel kinetic friction cone compliance model is introduced for the velocity impedance controller. It was determined that the new compliance model provided a more reliable insertion than the standard insertion model by increasing the error tolerance for failure.

# Contents

# List of Figures

# Chapter 1

# Introduction

This chapter presents the velocity based visual impedance controller and introduces the object insertion problem to test the controller. The problem overview and the controller setup will be discussed in this chapter. This chapter also establishes how the rest of the thesis will be organized.

## 1.1 Problem

Compliant motion control is an important robotic technique for manufacturing. In particular, compliant motion control is useful when a robot must interact with a rigid environment, another robot, or a human. Object insertion is a great application to test a compliant motion controller. Compliant motion is needed because orientation errors can cause jamming or wedging during insertion.

This thesis will use a difficult key and hole insertion to demonstrate the capabilities of a new type of compliant motion controller. The proposed controller is a velocity filtered visual impedance controller. The key and hole insertion is used because of the precise position and orientation required.

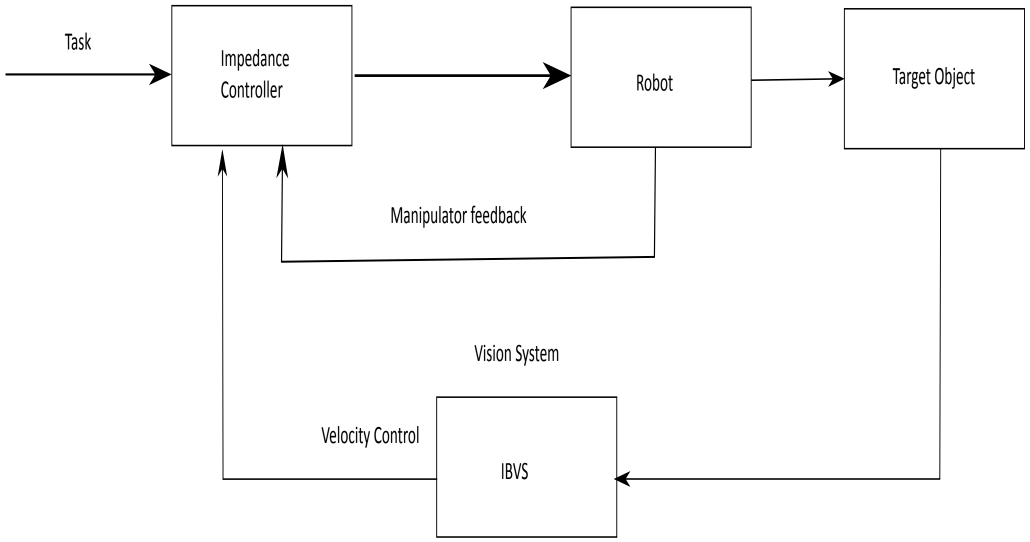

Figure 1.1: Basic Control Scheme.

The velocity filtered impedance controller will use image based visual servoing (IBVS) combined with an impedance controller. Figure 1.1 depicts the relationship between the IBVS and the impedance controller. With this velocity filtered visual impedance controller, a robot will insert a key and generate a friction cone during the insertion controlling the velocity of the manipulator. Friction cones are the space in which an applied force will not slip. The cone determines the maximum angle before slipping occurs. In robotics the friction cone is used as a configuration space model. This thesis will use a dynamic friction cone approach instead of this static friction cone. After modeling a kinetic friction cone for an insertion problem, a robot can learn the most effective path to travel and adjust its forces for a successful motion.

The hypothesis is that by using a velocity filtered visual impedance controller a robot is capable of extremely difficult object insertions such as key insertion. By using a velocity based approach the robot will be able to generate a kinetic friction cone for an improved object insertion compared to the position based position based impedance control.

## 1.2 Contribution

This thesis develops a reliable vision filtered impedance controller by using a fusion of an impedance controller and an image based visual servoing (IBVS) controller while introducing the new velocity filter to the controller. Using this velocity filtered impedance controller, this thesis will develop a method to build the novel kinetic friction compliance model for challenging insertions used in mechanical assembly. This thesis will also demonstrate the improvement in object insertions when using a velocity filtered impedance controller compared to the position based impedance controller.

## 1.3 Impact

Using a velocity based approach will improve upon the impedance controller by increasing the range of stability to higher stiffness values. This is important for object insertion since the positional and pose accuracy will ensure a successful insertion. As will be shown later, higher stiffness values will lead to more accurate motions and will also increase the insertion force needed for object insertion. This velocity based approach also ensures stability in the high stiffness environment that would be encountered during more difficult insertions such as the key insertion. As will also be shown, the position impedance controller can start to lose stability in these confined environments due to the friction forces. Using a velocity filtered impedance controller for difficult insertions, such as the key insertion, will not only show that it is a viable and more stable control method but will also show the practicality of a kinetic friction cone model.

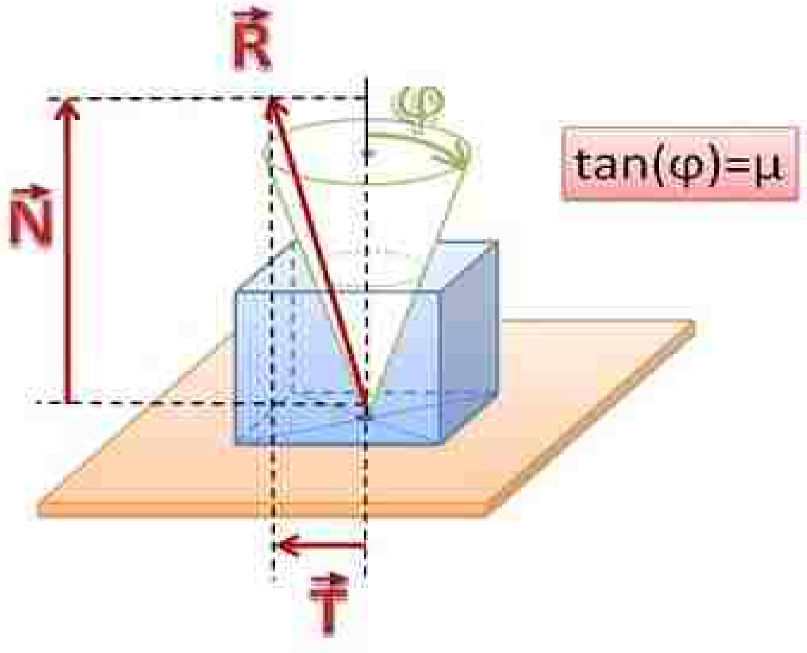

Figure 1.2: Basic Control Scheme [61]. Where R is the force vector, N is the vertical force contribution, and T is the horizontal contribution. $\phi$ is the friction cone angle and $\mu$ is the coefficient of static friction.

With the capabilities from the velocity impedance controller, it is possible to create a kinetic friction cone compliance model. A kinetic friction cone shares the same principles as the static friction cone, shown in Figure 1.2; however, with the kinetic friction cone we want the force vector to be outside of the friction cone. To do this the insertion force will need to be adjusted accordingly, as will be shown later. Using the kinetic friction cone compliance model and controlling the velocity to navigate through the insertion, it is possible to wiggle the object to the goal position.

Ultimately, this controller and kinetic fiction cone compliance model can be applied to a number of real problems including welding, grinding, dragging an object, and of course, object insertion.

## 1.4 Scope of Work

The focus of the thesis is to introduce a novel impedance controller. The work in this thesis is to expand upon well known position based methods for control and showcase a velocity based analog for the proposed controller. This thesis will also introduce a kinetic friction cone compliance model, modeled after the static friction cone, to prevent insertion failure. For the vision controller this work uses an IBVS controller to improve the impedance controller's accuracy. Using these velocity analogs in comparison with the position based methods this thesis will showcase the benefits of using a velocity based impedance controller.

## 1.5 Thesis outline

Chapter 2 presents the current state of the art in object insertion and impedance control. Chapter 3 describes the hardware used for the experiments. Chapter 4 defines the object insertion model as well as compares the difficulty of insertion for various geometries with respect to jamming and wedging, the two types of failure for object insertion. Chapter 5 defines the impedance controller, first modeling the controller and modeling the vision control. Next the chapter will demonstrate the simulation implementation of the model using *Simulink*, and then the results from the robot. At the end of chapter 5 the insertion results for the position impedance controller will be discussed. Chapter 6 defines the velocity impedance controller, again modeling the controller, showing simulation results, and then results from the robot. Chapter 6 results will compare the position impedance controller's responses from chapter 5 to the results from the velocity impedance controller. The end of chapter 6 will have insertion results from the velocity impedance controller and will compare these results with the insertions from the position impedance controller. Chapter 7 defines and models the kinetic friction cone model. In this chapter the compliance model will be defined and the velocity impedance controller stiffness will be optimized with respect to the accuracy of the robot. At the end of this chapter the compliance model will be tested against various insertions and compared to the previous insertion results from the velocity impedance controller. Chapter 8 concludes the thesis with a review of the research and the potential benefits for future work.

# Chapter 2

# Literature Review

The past twenty years has had a large push in robotics research to allow robots to replace humans in various dangerous tasks. These tasks range from bomb disposal to detecting environments with hostile threats. The issue is that these types of tasks are difficult to accomplish since the robot needs to be as capable as a human that would perform them. In these tasks a robot is likely to have to open a door. One of the most difficult but useful object insertions for a robot is a key insertion.

## 2.1 Literature Review

An important field of research previously discussed is the manipulation of unknown objects. Some of the most common objects that robots will encounter are doors. Most of the dangerous tasks in which robots would replace humans require mobility in human-made environments. To navigate through a room, a robot will have to recognize a door and interact with it to open it [26]. To open the door, the robot needs to apply a delicate amount of force and also has to be capable of compensating for various changes in the environment that it cannot detect such as a stiff door hinge.

For a robot to accomplish a task with fine motion, it needs to be capable of compliant motion. Compliant motion controllers can interact with objects passively or actively. Active compliance interacts with objects by controlling the external forces applied on the robot or using visual feedback.

### 2.1.1 Assembly

In the past ten years robotics in assembly has been focused on improving upon tasks currently completed by humans. The two main reasons to replace humans with robots is because of either the danger involved with the task, i.e., handling radioactive material, or improves upon the efficiency and time to complete a task. There has been interest in determining the most efficient use of multi-robotic production for the automotive industry [27]. There has also been work done in crowd sourcing swarm manipulation methods to determine how to improve cooperative manipulation in work spaces [3]. There has also been an increased focus in manipulation of small objects, as these tasks often prove difficult for humans [56].

Although many of these tasks can be accomplished by robots, there is still a significant difference in the accuracy and repeatability that humans can achieve. This is mostly due to the compliance humans provide when they interact with their environments. To address this there have been an interest in research in robotic assisted assembly. Some of these experiments include using robotic limbs to lift and assemble heavy objects through these supernumerary robotic limbs [40]. In one work, the human worker uses robotic limbs to assist in aircraft fuselage assembly [39]. There has even been interest in robots cooperating with humans to complete assembly tasks as well [12].

Although there is considerable research in cooperative robotic and human assembly, there is still a reluctance to introduce humans in robotic work spaces. This is due to most industrial robotic controllers being position based controllers. These types of controllers move straight to the task and adjust their position based on the error from the goal. Without compliance, the robot will collide with objects that may be in the path the robot is traveling. With compliance, the robot can soften the collision and become safer to use alongside humans.

### 2.1.2 Compliant Motion: Impedance Control

Compliant motion can be categorized in two ways: active or passive [25] [49]. Passive compliance does not require the robot to know how it is interacting with the environment but instead allows the hardware to naturally interact with objects. This can be a desirable compliant motion if the environment and objects are well-known. For object insertion, error corrective compliance is used since the contact forces always push the object towards the insertion goal [42]. Passive compliance may be the technique humans use to insert objects [15].

The issue with passive compliance is the limitations of its compliance, i.e., compliance in only a single dimension. As such, passive compliance is not typically used to interact with objects. Instead, active compliance is typically used in robotic systems. Active compliance differs in that it needs a sensor to detect the interaction with the environment to help control the motion. One of the few ways to achieve active compliance is to use a hybrid of force and position control [45]. Compliant motion is not limited to active or passive, there are hybrid types of compliant motions that are also used [51]. Typically these hybrid motions are decomposed into the active parts and the passive parts of the motion. These hybrid compliant controllers have even been used to grasp various objects [54].

Another technique is to use haptic controllers, which commonly rely on configuration spaces to provide force feedback [13, 31, 46, 11]. Haptic control relies on modeling the forces that the robot experiences; through this interaction the robot can perceive the forces. As such configuration spaces need to be created to limit the forces and directions in which the robot can interact in the environment. The friction cone is a configuration space representation of the overall stiffness of the environment when interacting with an object in various directions [31]. Another important compliance method that relies on modeling the stiffness of the environment is an impedance controller.

Impedance control is a concept popularized by Neville Hogan in 1985 [14]. The general idea was to treat the manipulator of the robot as an object that has impedance, in other words treat the manipulator as something with variable stiffness and damping. By changing the apparent stiffness and damping of the manipulator, it is possible to execute compliant moves. More formally, the impedance of the system is represented as a transfer function of the system that can either be a ratio of displacement over input force or of velocity to input force.

This type of controller uses the position, velocity, and output force of the manipulator. Using these multiple inputs, the robot is capable of interacting with external forces applied by the environment. Since the impedance is capable of interacting with external forces, it is capable of gross and fine motion [14]. The difficult task in using impedance controllers is determining the impedance for each task. There have been methods in how to use force references to improve the impedance controller [47], methods that use impedance controllers without torque feedback [21], and methods in varying the impedance depending on the environment [17].

There have been stiffness based tuning methods to improve the adaptability of robot-assisted rehabilitation [24], as well as non-linear adaptive impedance controllers also intended for rehabilitation purposes [36]. There have even been fuzzy adaptation impedance controllers used for peg in hole insertions [2]. The impedance controller has even been used with predictive controllers intended to prevent mechanical losses, i.e., losses from friction and external forces [10]. In terms of assembly based methods, there are impedance controllers that provide high-speed position and force responses for compliant microgrippers [57].

Various types of impedance control system uses different sensory feedback [44]. In particular, there are impedance controllers that use a vision system to maintain the desired contact with the robot and the object [32]. These visual impedance controllers typically estimate the position and the pose of the robot and object and provide a hybrid visual/force controller [22]. There are various other types of visual controllers that can be coupled with an impedance controller.

Velocity based impedance methods have been tested and found to be useful and stable [41, 8, 5]. Using a velocity based method insures that the steady state error will be zero. This type of impedance controller has been found to be stable in high stiffness environments using high damping values. This thesis will differ from these methods in that the velocity impedance contribution will filter the impedance force and the stiffness of the robot will act as a gain. Based on the stability models used from the position based impedance model [37] and also through impedance methods that have used integrator control [20] we have found that this method will also be able to improve upon the stability due to the stiffness being significantly larger than the damping.

### 2.1.3 Visual Servoing: Visual Impedance Control

Visual servoing consists of using information of the environment extracted by one or several cameras to control the movements of a robot [4]. This allows for a wide range of tasks that can be achieved such as object tracking, object manipulation, visual guided motion, and even object insertion [50]. Image based visual servoing is a field of research where control is based on feature points in the image plane [7]. This is a robust visual control method since the robot can account for disturbance and noise. IBVS can track the motion trajectories of objects in an image to execute tasks that other vision based controllers cannot accomplish due to image based errors [9].

The major disadvantage of visual control is that these camera internal parameters must be known through calibration. There is also the issue of depth. Since most environments are unknown, the typically 2D-sensor is not capable of extracting depth without some type of reference. Camera calibrations are broken into two categories: intrinsic calibration and extrinsic calibration. Intrinsic calibration determines the internal parameters of each camera, such as focal length and pixel height/width. Extrinsic parameters are the parameters that relate the objects in the environment, depth and rotation, back to the camera. This includes the transformation matrix from camera to the origin and the depths of feature points in the image.

Intrinsic camera calibration methods have been thoroughly researched and understood [60, 59, 52]. Typically calibration objects are well defined object, already known geometries. Camera calibration is done by taking multiple images of these calibration objects and determines the intrinsic parameters of each camera from these images. Extrinsic camera calibration is a bit more difficult since determining the environment's depth requires some sort of reference. The use of reference points or fiduciaries can simplify extrinsic calibration since these reference points are known and provide enough information in the image to determine the extrinsic parameters [16]. Extrinsic camera calibration in an unknown environment is much more difficult since known reference points cannot be used. There are methods that achieve this calibration by moving unknown detected objects in the environment and taking as many images as needed until the parameters are determined [58]. The issue with this type of method is that it tends to be costly computationally.

There are calibration methods that are capable of extracting both the intrinsic and extrinsic parameters online. In other words, it is possible to do calibration in unknown environments by navigating in the environment and simultaneously calibrating the vision system [1]. One particular method of online calibration is to use circular motions around a feature point to extract all calibration parameters [34]. Once a camera is fully calibrated to its environment, it is possible to accurately control the robot using any visual servoing technique. As mentioned before, there exist visual/force hybrid controllers, which allow the robot to detect and interact with various object in the environment [43].

Visual impedance controllers use the visual data and provide feedback from the environment to an impedance controller [33]. A visual impedance controller uses vision to determine position and orientation errors. Figure 1.1, shows the basic control scheme for a visual impedance controller. In this case the velocity is provided by vision instead of position. An example of a vision based impedance approach is to follow the contours of an object's edge [18]. By using an impedance controller, a robot performing edge tracking can smooth out the trajectories and can accomplish these motions at high velocities without sacrificing accuracy. Although there are velocity based impedance controllers, there are no velocity based visual impedance controllers.

Visual impedance controllers have also been used for the task of object insertion [53] [48]. These controllers are very useful for insertion because of the orientation required to properly insert an object. To prevent failure the initial orientation of the object must be within a certain tolerance. It is difficult to determine whether the object is within this tolerance without vision. Using these vision control methods the robot is capable of fixing the orientation errors in real time and improving the chances of a successful insertion.

### 2.1.4 Friction Cones

Object insertion is the one of the best methods to test a compliant controller. Object insertion has been shown to depend on how the objects interact with each other as they pass through different contact states [55]. The two types of failure during the insertion are known as jamming and wedging, shown in Figure 2.1. Wedging occurs when a contact force becomes compressive and holds the object in place. To avoid wedging, the orientation error of the object insertion must always be minimized.

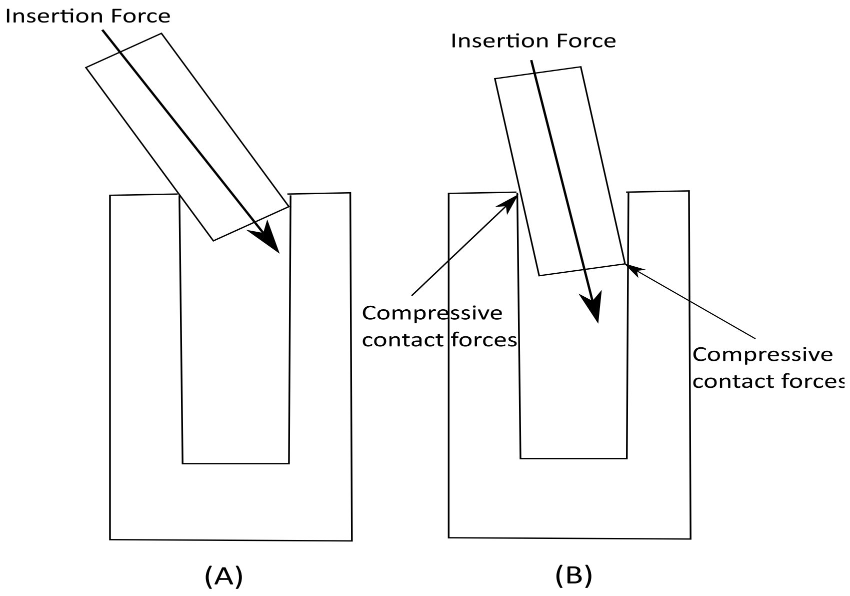

Figure 2.1: Modes of Failure Jamming (A) and Wedging (B)

Jamming occurs when the insertion force is misaligned with the insertion axis. To avoid this failure, the object needs to rotate to compensate for the misalignment[55].

One particular method to avoid both types of failures is to create friction cones. A friction cone is a 3 dimensional representation of the friction angle. The friction angle is determined as the maximum angle a force vector can have before slipping occurs [35]. This is shown in Figure 1.2. The friction cone was found to be bounded by the following relationship,

$$\tan(\theta) = \mu, \tag{2.1}$$

where $\theta$ is the friction angle defined by the force vector and $\mu$ is the coefficient of friction.

Friction cones in robotics are ranges created in configuration space that determine whether an insertion will be successful as long as the robot avoids entering this space [6]. By creating these regions, it is possible to know which motions will succeed with insertion and which will fail [38]. The concept of the friction cone is not limited to insertion. It has also been applied in grasping objects [30].

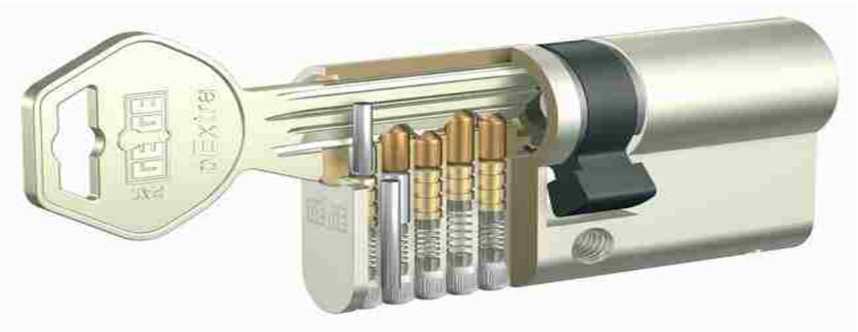

Figure 2.2: Key inserted in lock [23]

The friction cone is not limited to modeling the static friction limits; it can also be applied to Coulombic friction [29]. For this thesis we will introduce a kinetic friction cone that will model the kinetic friction the same way the friction cone models the static friction limits.

Key insertion is an extremely difficult object insertion task due to the geometric constraints. A door that may need to be opened by a robot may be locked, so the robot needs to be capable to insert a key and rotate it to unlock the door. Here lies the major problem; not only must the object be fully inserted, must be able to rotate after insertion. Figure 2.2 shows how the key must be aligned before being able rotate it to unlock it. There is similar work in rotating inserted objects into object with varying friction[19]. This work is important since the robot needs to be able to distinguish between when it is capable of rotating and when it is not.

## 2.2 Summary

Robotic assembly continues to grow as a field and will accelerate with the use of compliant controllers. The impedance controller was originally introduced when the hardware did not exist to realize the controller [14]. Now that the hardware exists, the impedance controller has been used to complete various assembly tasks. To improve upon the accuracy of the impedance control system the impedance controller has been used in various vision control systems. With the recent developments in visual servoing, the accuracy and capabilities of the impedance controller has improved and grown. Finally, through the use of configuration space models such as friction cones, the impedance controller has improved its compliance capabilities, which can be very useful for object insertion. The position based position impedance controller tends to go unstable in high stiffness environments normally encountered during insertion. The need to improve the stability of the impedance controller at high stiffness still exists.

# Chapter 3

# Hardware and Testing

The system developed and tested in this thesis consists of equipment from the Robotics Lab in UNM's South Campus MTTC building. The system consists of a Barrett Technology Whole Arm Manipulator (WAM), two cameras, reflective memory, a computer controller, and stationary objects for insertion. An example of the experimental setup for the key insertion is shown in Figure 3.1 .

## 3.1 Hardware

The WAM is a 7 degree-of-freedom robotic arm developed by Barrett Technology. The WAM communicates through reflective memory to a target computer, which controls the robot through a *Simulink* controller. For this thesis, a velocity based impedance controller was implemented in *Simulink*, compiled, and loaded onto a xpctarget through *Matlab*. For the xpctarget to communicate with the WAM the xpctarget communicates directly to the reflective memory using C/C++ wrappers. The xpctarget communicates with the reflective memory by reading and writing from specific memory addresses, called nodes. The WAM has an on-board computer that also reads and writes to the reflective memory. Specifically, the controller computer

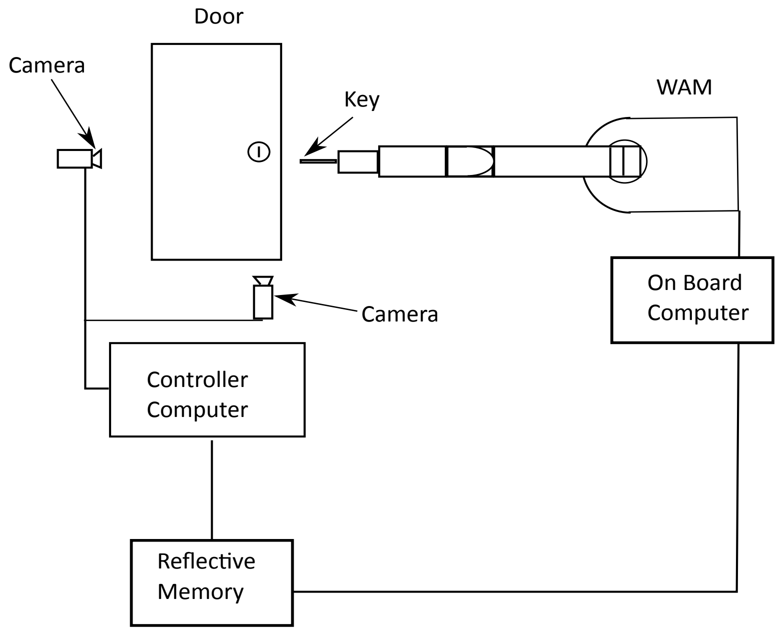

Figure 3.1: Experiment setup.

writes 6 stiffness, 6 damping, 7 joint torques, and 6 goal positions while the WAM's on board computer writes the 7 current joint torques and the 7 current joint angles of the WAM. The controller computer reads the goal positions, the current joint angles, and the current joint torque while the WAM's on board computer reads the stiffness, damping, motor currents, force, and joint torques.

The controller computer, the computer running the *Simulink* controller, has a 2.4 GHz Intel processor and eight Gigabytes of RAM. The controller computer simultaneously reads the WAM's position, calculates the next position in the trajectory, and also communicates with the vision systems to determine how to adjust the trajectory. For the vision systems, a Logitech c270 and c260 cameras were used. Both cameras have resolution up to 1280 × 720 and communicate via USB. To communicate to *Matlab*, additional drivers had to be installed using a webcam toolbox for image processing. The image processing done in *Matlab* sends the results to the impedance controller in *Simulink*, which sends the positional and compliance data to the reflective memory.

The WAM works in joint space; its on-board computer reads and writes its positions based on the angles and torques on each joint. However, the vision controller and impedance controller work in Cartesian space. The $7 \times 6$ Jacobian for the robot is already known and used to convert Cartesian torques $6 \times 1$ to joint torques $7 \times 1$. To determine the end effector with respect to the WAM, a homogeneous $4 \times 4$ transformation matrix is used. To avoid singularities, the rotation matrix is converted into quaternions. The quaternions and the translation vector are used for the path planning in the controller. For every clock cycle in *Simulink*, about 0.005 seconds, each of these parameters is calculated and communicated through the reflective memory.

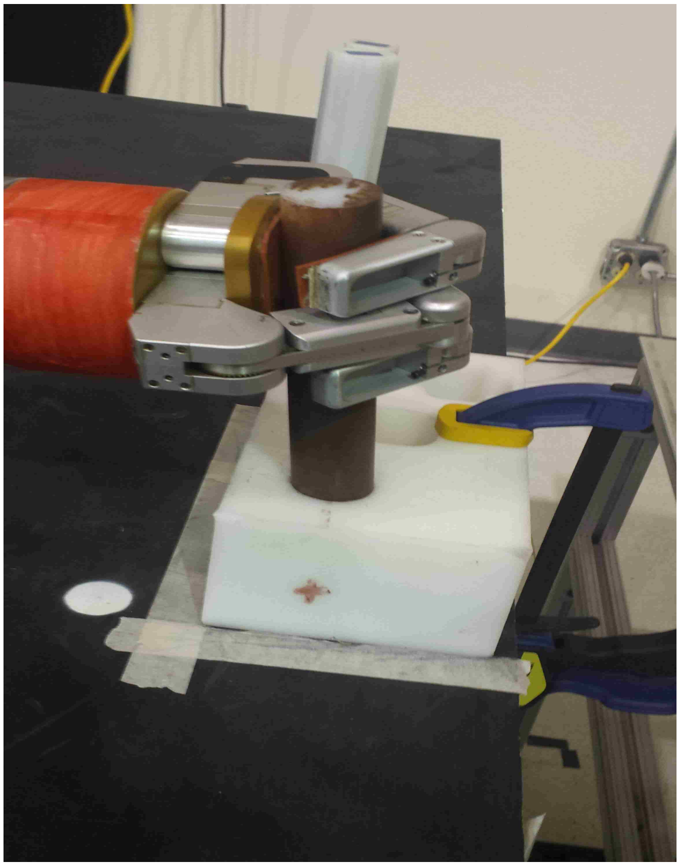

Figure 3.2: Experiment setup. Insertion of circular peg into fixed block.

For the object insertion the initial testing will be done on a circular peg-and-hole made out of ABS, shown in Figure 3.2. The circular peg is used as a baseline since this type of object insertion is one of the easier types of insertions, as will be shown in Chapter 6. Next, insertions will be done for the square peg and the cross peg. The cross peg will also be tested against gravity to shown the response of the controllers. The final type of object insertion will be done using a nickel silver key to be inserted inside a brass keyhole. The exact model and setup for this experiment will be further discussed in Chapter 7.

# Chapter 4

# Object Insertion

In this chapter we will first model an object insertion using the simple peg and hole model. We will then look into failure modes for the peg and hole model, particular jamming and wedging. To do this we will be using a peg and hole insertion model defined by Whitney. [55] Next we will look into expanding the simple axial-symmetric model to various insertion cross sections. We will expand upon the Whitney model for axisymmetric insertions and apply the same model to other geometries. Finally, we will look into applying this insertion model to the complicated geometry of a key and lock insertion.

## 4.1 Peg and Hole Model

To begin, this analysis we will be using a two-dimensional model because of the axisymmetric properties of a circular peg. The two-dimensional model captures all of the kinematics of the three-dimensional system, and later we will expand this model for non-axisymmetric geometries. Figure 4.1 demonstrates a two-dimensional progress of a peg insertion. In the first stage of insertion we have the robot making a gross motion to prepare for the insertion. In this stage the alignment correction

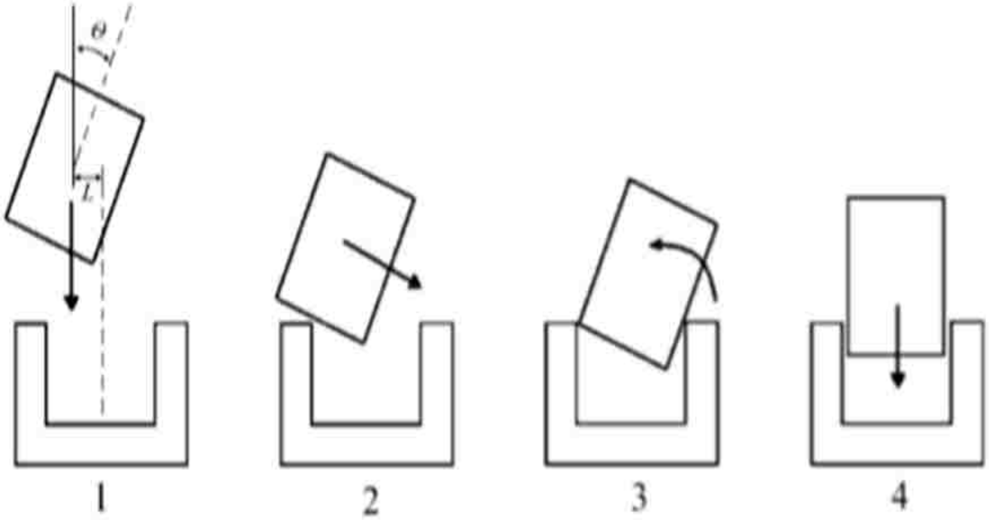

Figure 4.1: Chamferless insertion strategy. Stage 1 is the approach, 2 is the one-point contact, 3 is two point contact, and 4 is line contact and successful insertion [48]

begins, fixing these lateral and rotational errors play a large part to the success to the insertion. The next stage we begin to insert the peg into the hole. If the peg has a chamfer this will assist in guiding the peg into the hole. A chamfer peg will allow the peg to slide into the hole and correct for any additional lateral error. In the chamferless case, as will be the case in our testing, the peg must be angled as it is inserted to mimic this chamfer sliding. During this stage there will only be one point of contact between the peg and the hole. In the chamfer case the next stage will be the one point contact past the chamfer as the peg is inserted. This additional stage is shown in Figure 4.2. For both cases the next stage is the two-point contact stage. In this stage the peg comes into contact with the hole at two points. This is the most important stage as this is the likely point for failure, as jamming and wedging can occur at this stage. The final stage is a completed insertion.

To successfully insert an object the second, third, and fourth stages are the

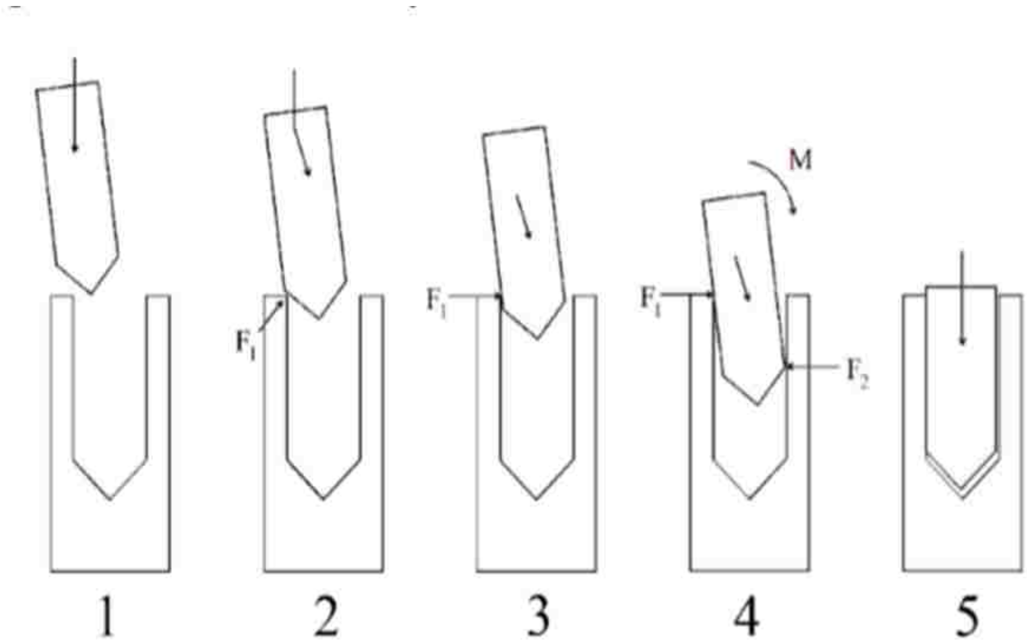

Figure 4.2: Chamfered insertion. There is one additional step for chamfered assembly, 2. chamfer crossing. [48]

most important for compliant control. We will soon explore the limitations in error for the two-dimensional case where an insertion can be successful. To determine these limitations we need to try to minimize the likelihood of jamming and wedging. Jamming occurs when the axial force inserting the peg is too far away from the axis of insertion. Jamming is avoided by designing the compliance of the peg to allow it to translate and align by a result of the moments generated during the two-point contact. Wedging occurs upon the onset of two-point contact if the contact forces create a compressive forces that deforms the peg instead of assisting in aligning it. Wedging is avoided by maintaining proper alignment of the peg and hole as two-point contact approaches. Figure 4.3 illustrates these two modes of failures for this two-dimensional model.

The success of the peg and hole insertion depends on keeping the insertion force aligned properly. To do this we need to engineer the compliance of the system to

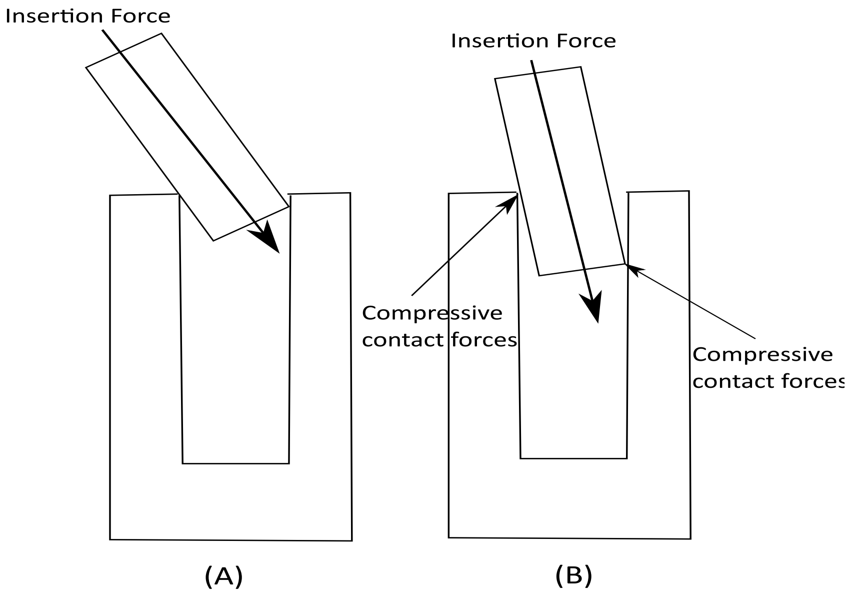

Figure 4.3: Modes of Failure Jamming (A) and Wedging (B)

allow the peg to be able to translate and rotate as needed to reject errors in the face of contact forces during insertion. To design this type of compliant system, we will treat the robot and peg as a system of linear springs. These linear springs can impose forces on the peg as a reaction to translation and rotational parts of the insertion. To fully model the degrees of freedom allowed by the robot and peg we will have six different stiffness values, 3 translational and 3 rotational. As will be shown in chapters 5-7, we can vary these stiffness values in each degree of freedom to improve the accuracy of the insertion and change the response from contact forces. However, in this case we will be modeling these stiffness values as springs acting against the environment.

To make this compliant model we will treat the robot and peg system as these six linear springs. Doing this we can model the compliant interaction between the peg and the hole during insertion.

$$F_{6X1} = K_{6X6}U_{6X1} \tag{4.1}$$

where $U$ is the displacement, $K$ is the stiffness matrix, and $F$ is a vector of external forces.

As can be seen from (4.1) the stiffness matrix contains 36 different stiffness variables to control while interacting with the environment. While this has been used in various systems , it is more desirable to simplify this stiffness matrix to a diagonal matrix. This makes modeling simple since we can now treat motion in each dimension as having two acting springs, a translational and rotational spring. For now we will start with the axisymmetric case where we can further simplify the model, we will discuss the modeling for the other geometry specific cases later. Since the circular peg has an axisymmetric insertion we can simplify the insertion model into a single dimension. Two assumptions for these insertion models are that the insertions will be slow enough for quasi-static interactions, and that the peg is stiff enough to be modeled as a rigid body. We will expand upon the quasi-static model such that we try to prevent these interactions when we start to look at the kinetic friction cone modeling in chapter 7.

This two dimensional model will start with the clearance between the peg and the hole. We will introduce a dimensionless factor called the clearance factor, this dimensionless factor provides a measure of clearance between the diameter of the peg and the diameter of the hole,

$$c = \frac{D - d}{D}, \tag{4.2}$$

where $D$ is the diameter of the hole and $d$ is the diameter of the peg.

We will begin to analyze the peg and hole model to prevent wedging. Wedging is

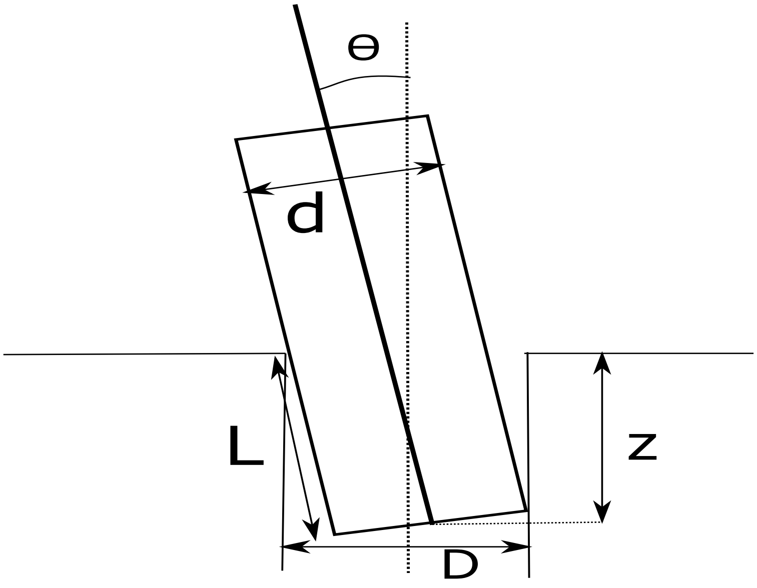

Figure 4.4: Diagram of chamferless peg partially inserted.

primarily a function of the initial error of the peg relative to the hole and insertion axis. To begin this analysis we need to determine the clearance angle between the peg and hole during this stage of insertion. Figure 4.4 shows a model of a peg at two-point contact, we can derive a model of the maximum amount of angular error as a function of depth during insertion,

$$L\tan(\theta) = cD, \tag{4.3}$$

where $L$ is the length of the peg currently inserted in the hole, which can be determined as $L = z\cos(\theta)$. This equation shows that the amount of lateral error allowed with this rotational error cannot exceed the clearance between the peg and the hole.

Equation (4.3) shows that the insertion depth and the rotational error are inversely proportional. As the depth of insertion increases the rotational error decreases which means the likelihood of a successful insertion increases. This means

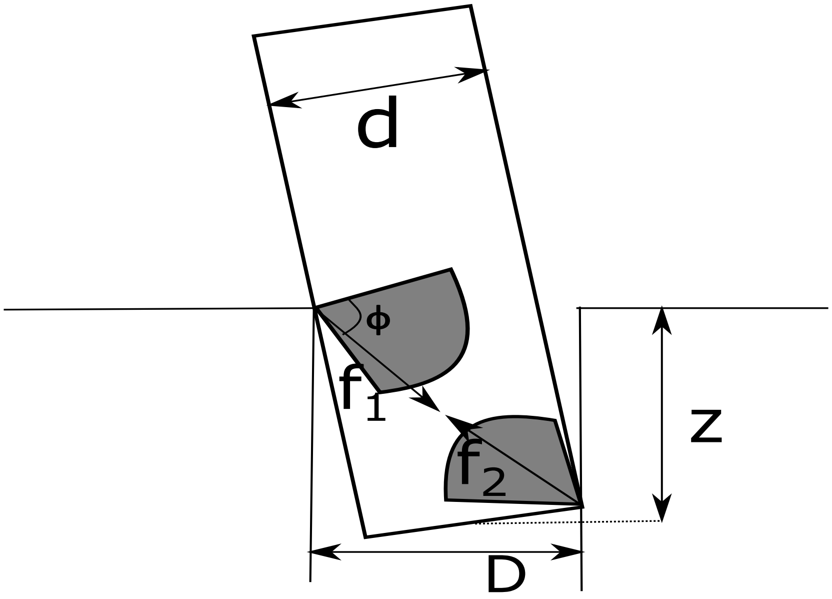

Figure 4.5: Diagram of a peg failing due to wedging. Wedging occurs when the two friction force vectors, $f_1$ and $f_2$, align forcing the peg to compress from the aligned forces.

that failure is most likely to occur during the initial parts of the insertion, since there is a larger range of allowable rotational error. For wedging to occur the contact forces become compressive and store energy in the peg from the deformation. These contact forces are largely friction limited so we can apply small friction cones to each of the contact forces. As defined before, friction cones are cones that model the space where the vectors of forces on an object will keep the object static. As long as the force vector at the point of contact remains in the friction cone, then the object will not move.

Figure 4.5 shows this wedging model with these friction cones at the two contact points. To cause this compression we need the friction forces to point towards each other. Figure 4.6 shows the relationship between the friction cone and the friction angle. We define the friction angle as $\tan(\theta) = \mu$. Using this relationship and that shown in Figure 4.6 we get the following relationship with the insertion depth and

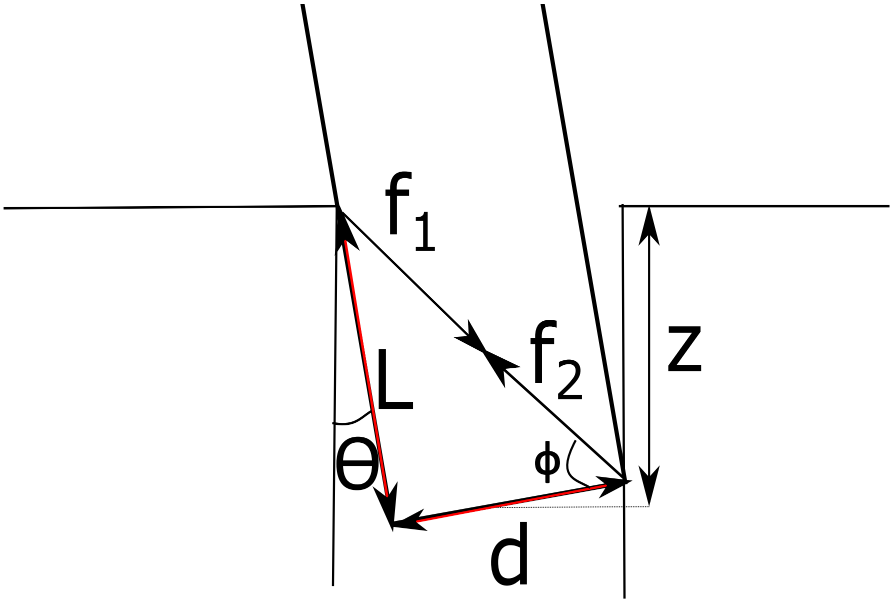

Figure 4.6: Diagram of aligned friction forces during wedging. Here we see the minimum angle needed to cause compression and the geometric relationship with the peg and the insertion depth.

the friction cone,

$$\mu = \frac{L}{d} = \frac{z\cos(\theta)}{d}. \tag{4.4}$$

Equation (4.4) defines the relationship between the friction at the contact points and the allowable rotational error for the depth insertion. Combining 4.4 and 4.3 we can rewrite the maximum rotational error as a function of the clearance factor,

$$\tan(\theta) = \frac{cD}{\mu d}. \tag{4.5}$$

Since this rotational error has to be as small due to the geometric constrains, we will use the small angle approximation to simplify (4.5),

$$\theta = \frac{cD}{\mu d}. \tag{4.6}$$

Equation (4.6) defines the maximum allowable rotational error before wedging if there is no lateral error present. If the rotational error exceeds the value from (4.6) then the friction force vectors will align and the forces will become compressive on the peg. Now that we have a rotational error model we need to define a maximum allowable lateral error. To do so, we will look at Figure 4.7, which shows the lateral error allowable for the chamfered case and the chamferless case. Where $R$ is the hole's radius and $r$ is the peg's radius,

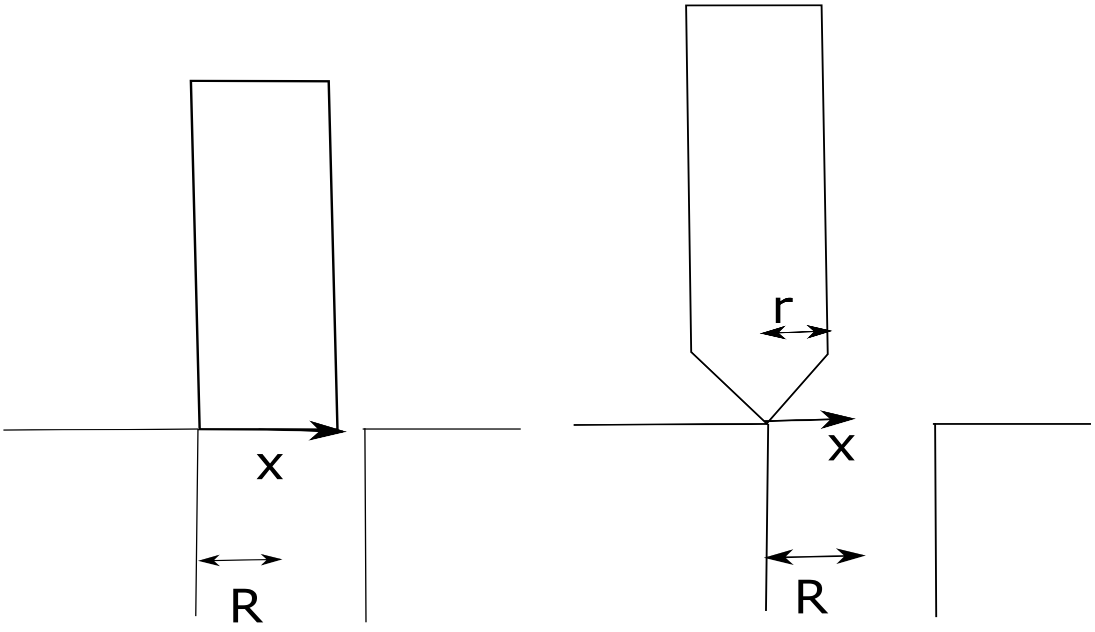

Figure 4.7: Here we see the maximum allowable lateral error for the chamferless case and the chamfered case. We can see that chamfer case will have a larger tolerable lateral error determined by the chamfer width.

$$-R < \epsilon < R \tag{4.7}$$

for the chamfered case where the chamfer width is the same as the peg's radius,

$$-(R-r) < \epsilon < R-r \tag{4.8}$$

for the chamferless case. In both cases $D = 2R$ and $d = 2r$.

We should note that this maximum lateral error cannot exceed the values from (4.7) or (4.8) since the peg will miss the hole regardless of rotational error. So for our failure model we define our bounds within (6.7) or (6.8) depending on the peg. As previously mentioned there is a relationship in which the lateral error contributes to the rotational error. Whitney [55] showed this relationship for the case of shallow insertion depths as the following,

$$\theta_{total} = \theta + S\epsilon, \tag{4.9}$$

where $S$ is defined as $S = \frac{L}{L^2+\frac{K_\theta}{K_x}}$, and where $K_\theta$ and $K_x$ are the rotational stiffness and the lateral stiffness, respectively.

Using equations (4.6) to (4.9) we now have a two-dimensional model that restricts the rotational error and translational error to prevent wedging. This two-dimensional model to prevent wedging is shown in Figure 4.8. We can see that wedging is constrained to the initial accuracy of the robotic system instead of the compliance of the controller. As such, wedging prevention is mostly related to the path planning during the insertion and less related to the compliance of the robot.

Moving on to the issue of jamming we will see that this is where the compliance controller plays an important role in the insertion. Jamming occurs because of the insertion force vector of the peg being unaligned from the axis of insertion. To determine these force limitation we will again look at the model derived from Whitney

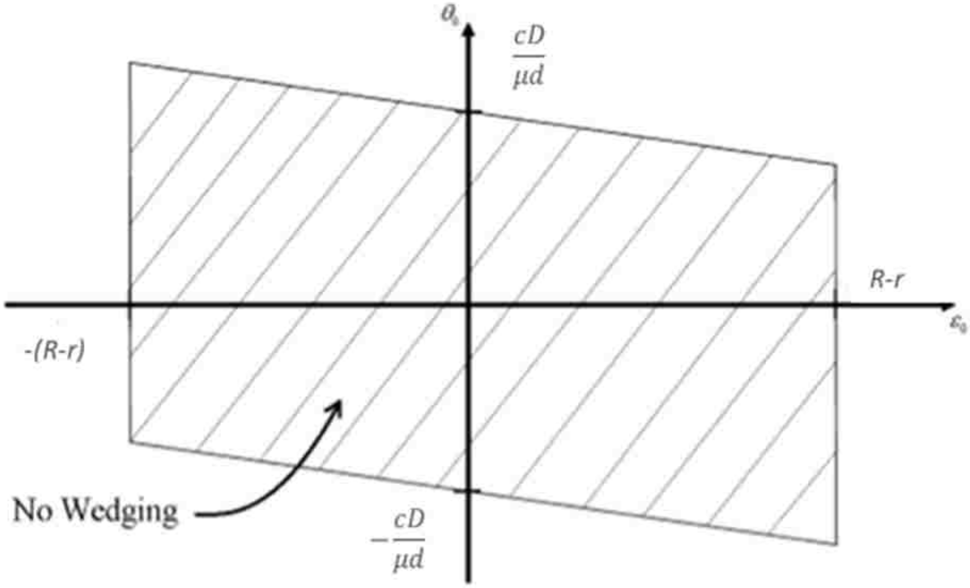

Figure 4.8: The wedging model for the chamferless case. The boundaries to prevent wedging are a function of geometry and friction.[55]

on jamming [55]. Figure 4.9 shows the jamming avoidance model with respect to contact forces $F_x$, $F_z$, and $M$.

The jamming diagram differs from the wedding diagram in that it changes with respect to insertion depth, $z$, and is constrained by insertion forces which can be controlled by a complaint controller. The depth relationship is due to its linear relationship with the introduced variable $\lambda$,

$$\lambda = \frac{z}{\mu D}. \tag{4.10}$$

From figure 4.9 and equation (4.10) we can see that the quadrilateral to prevent jamming will grow larger as the insertion depth increases. However the width of this quadrilateral does not increase since it is constrained by coefficient of friction. As we can see from the jamming diagram the success of the insertion is dependent upon the

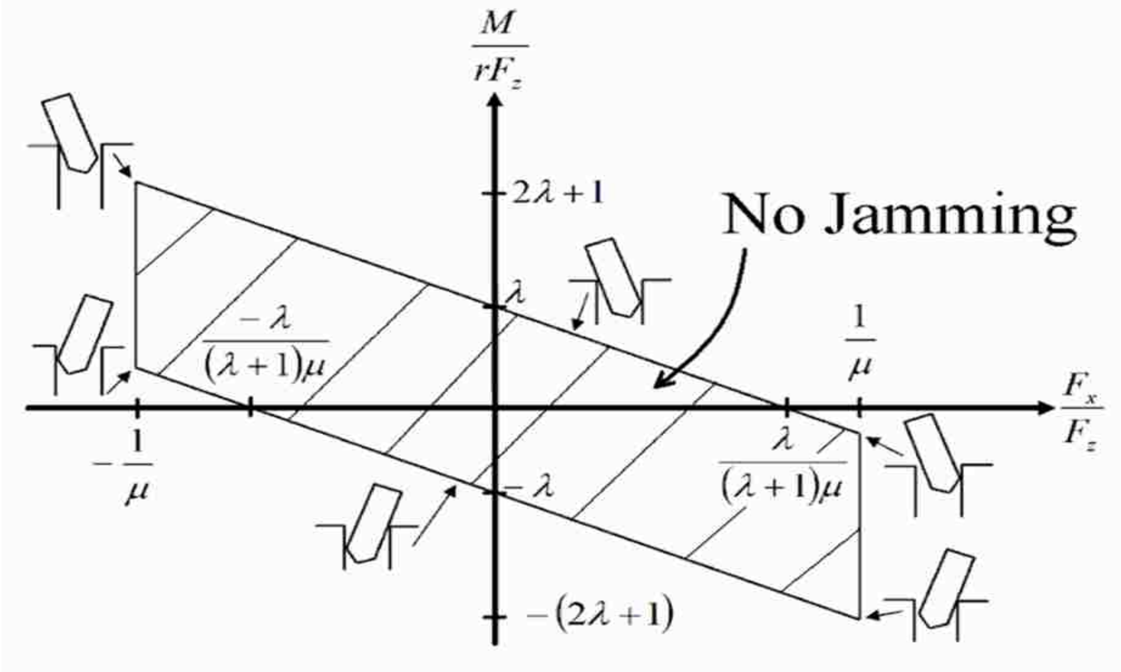

Figure 4.9: Jamming diagram as defined by Whitney. These boundaries expand in the vertical axis as the depth of insertion increases. [55]

force and moment relationships during insertion. These force and moment relations change during insertion so we need to define them for the three important stages of insertion. For the sake of our testing we will only focus on two stages: one-point contact and two-point contact.

To begin the one-point jamming force model we will use Figure 4.10 as a reference for our model. During one-point contact, the single contact point is the source of reaction forces and moments acting on the peg. Using Figure 4.10 we can see that the rotational error is simply $\theta$. The lateral error can be found as the following,

$$U = \frac{cD}{2} + L\sin(\theta) - z\sin(\theta). \tag{4.11}$$

Again we will use small angle approximation to simplify our model as well as define the initial error of the peg as $U_0 = \epsilon_0 + L\theta_0$. So our error model, combining

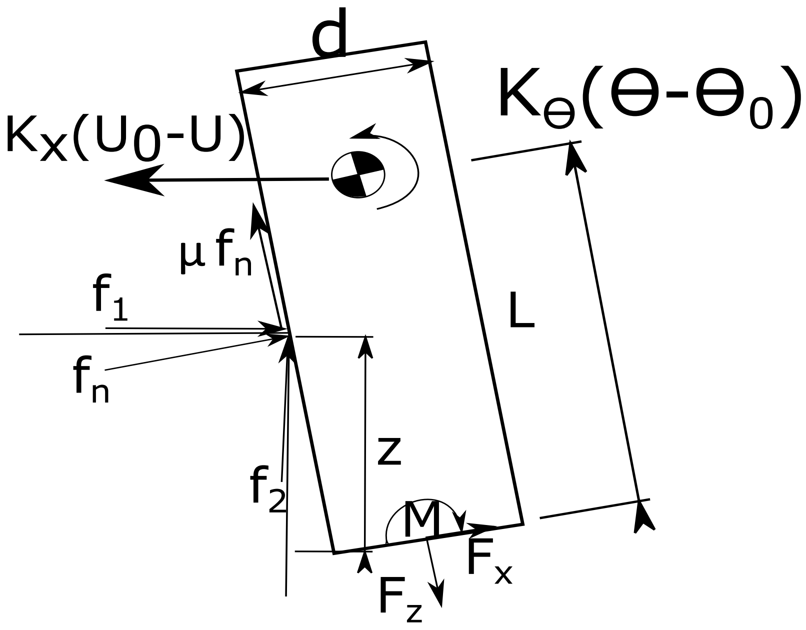

Figure 4.10: Force model for one point contact stage.

both the rotational error and the lateral error, becomes the following,

$$U_0 - U = \epsilon_0 - \frac{cD}{2} + L(\theta_0 - \theta) + z\theta. \tag{4.12}$$

To find a force relationship to represent the errors independently, $U$ and $\theta$, we will treat the reaction forces as quasi-static forces. Doing this we will have the reaction forces shown in Figure 4.10. These friction reaction forces are the only external forces exerted on the peg during insertion.

$$f_1 = f_N[\cos(\theta) + \mu\sin(\theta)] \tag{4.13}$$

$$f_2 = f_N[-\sin(\theta) + \mu\cos(\theta)] \tag{4.14}$$

Now we will find the relationship between these contact forces and the forces and moments applied to the peg.

$$
\begin{aligned}
F_x &= -f_1 && (4.15)\\
F_z &= f_2 && (4.16)\\
M &= f_1[L\cos(\theta) - z] + f_2[\frac{D}{2} - \frac{cD}{2} + z\theta - L\theta] && (4.17)
\end{aligned}
$$

We can simplify the moment further since we have been applying the small angle approximation throughout our analysis. When we make this assumption we can simplify the acting contact force contributing to the moment as one dimension and relate it to a simple moment arm. This is an important simplification since this allows us to separate the rotational and lateral error.

$$M = f_2\frac{d}{2} \qquad (4.18)$$

Now that we have a physical relationship between the contact forces, let us look at the compliance force acting on the peg and the robot. To do this we will be using our compliance model including our stiffness variables. We should note that the insertion force, $F_z$, will be a constant force during the insertion.

$$
\begin{aligned}
F_x &= -K_x(U_0 - U) && (4.19)\\
M &= LK_x(U_0 - U) + K_\theta(\theta_0 - \theta) && (4.20)
\end{aligned}
$$

Using these values Whitney found the forces and moments to be the following [55].

$$F_z = \frac{\mu K_x K_\theta(\epsilon_0 - \frac{cD}{2} + L\theta_0)}{K_x(L - z - \frac{\mu d}{2})(L - z) + K_\theta} \tag{4.21}$$

$$F_x = - \frac{K_x K_\theta(\epsilon_0 - \frac{cD}{2} + L\theta_0)}{K_x(L - z - \frac{\mu d}{2})(L - z) + K_\theta} \tag{4.22}$$

$$M = \frac{L K_x K_\theta(\epsilon_0 - \frac{cD}{2} + L\theta_0)}{K_x(L - z - \frac{\mu d}{2})(L - z) + K_\theta} - K_\theta \left[\frac{K_x(L - z - \frac{\mu d}{2})(\epsilon_0 - \frac{cD}{2} + L\theta_0) + K_\theta\theta_0}{K_x(L - z - \frac{\mu d}{2})(L - z) + K_\theta} - \theta_0\right] \tag{4.23}$$

Where $F_Z$ is the insertion force, $F_X$ is the lateral force, and $M$ is the moment. Now we have force and momentum equations entirely with respect to geometric constants, depth, and the compliance stiffness we have a model to control the jamming. Reviewing figure 4.9 the horizontal dimension is $\frac{F_x}{F_z}$ and the horizontal axis is $\frac{M}{rF_Z}$. As we can see the horizontal axis from equations (4.21) and (4.22) is simply the friction constant, which is not a concern for jamming since the insertion force is expected to be much larger and should not be the jamming limitation. Instead the vertical axis will be the focus for jamming prevention. When plugging in equations (4.23) and (4.21) into the ratio we get an equation of the form of $\frac{M}{rF_Z} = a(z)$. This is simply a function and geometric constants, there is no depth dependence for this stage of insertion.

Finally we will look at the two point contact case. Figure 4.11 shows the geometry and model of a peg in two point contact. This model does not require the static model as the one-point contact model as the system is fully geometrically constrained. Instead we will use the constraint for wedging introduced by equation (4.3) and modify it to reflect the constraints from the wall.

$$R = \frac{z}{2}\theta + \frac{d}{2} \tag{4.24}$$

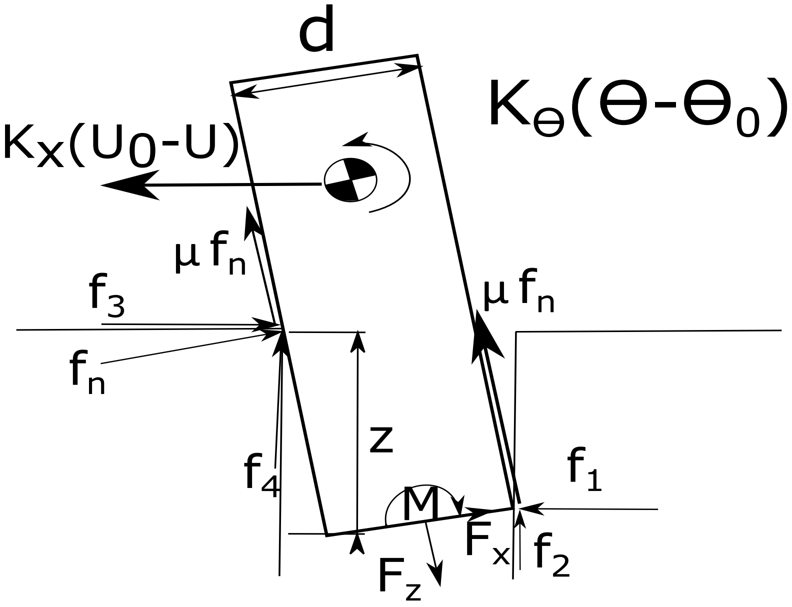

Figure 4.11: Force model for two point contact stage.

The maximum rotational error is found simplifying (4.3) with the small angle approximation $\theta = \frac{cD}{z}$. Finding the lateral error is similar for the one-point contact case.

$$U_0 - U = \epsilon_0 + \frac{cD}{2} + L(\theta_0 - \theta) \tag{4.25}$$

Determining the insertion force, lateral force, and moment requires a different force model because of the second point of contact. Using this two-point error model Whitney found the forces and moments to be the following [55].

$$F_x = -K_x L(\theta_0 - \frac{cD}{z}) - K_x(\epsilon_0 + \frac{cD}{2}) \tag{4.26}$$

$$M = (K_x L^2 + K_\theta)(\theta_0 - \frac{cD}{z}) + K_x L(\epsilon_0 + \frac{cD}{2}) \tag{4.27}$$

$$F_z = \frac{2\mu}{z}[(K_x L^2 + K_\theta)(\theta_0 - \frac{cD}{z}) + K_x L(\epsilon_0 + \frac{cD}{2})] \\ + \mu(1 + \frac{\mu d}{z})[-K_x L(\theta_0 - \frac{cD}{z}) - K_x(\epsilon_0 + \frac{cD}{2})] \tag{4.28}$$

Again for this model, when we look at preventing jamming we want to focus on $\frac{M}{rF_z}$. In this case there is now a compliance relationship. This jamming parameter has the following form $\frac{M}{rF_z} = b(z, \frac{K_\theta}{K_x})$. This means that the compliance ratio is now a control parameter for this jamming model.

Now that we have a model to prevent jamming using compliance control we need to be able to distinguish the difference between the different stages, particularly between one-point to two-point contact. Whitney [55] has determined the depth at which two point contact begins.

$$z_{2-point} \cong \frac{cD}{\theta_0} \tag{4.29}$$

We can also use Whitney's derivation for when the two point contact becomes a line contact [55].

$$z_{end} \cong \frac{K_\theta}{K_x}\frac{\theta_0}{\epsilon_0 + \frac{cD}{2}} - z_{2-point} \tag{4.30}$$

Again we see the important compliance factor $\frac{K_\theta}{K_x}$ for insertion. We can see that this factor will be our controllable parameter to improve the quality of insertion. We will now expand upon Whitney's peg insertion model and look at object insertions for different geometries of insertion. All of the relevant force and moment equations will change slightly for certain parameters but the overall models will not change significantly for the axisymmetric case.

## 4.2 Insertion Geometry Analysis

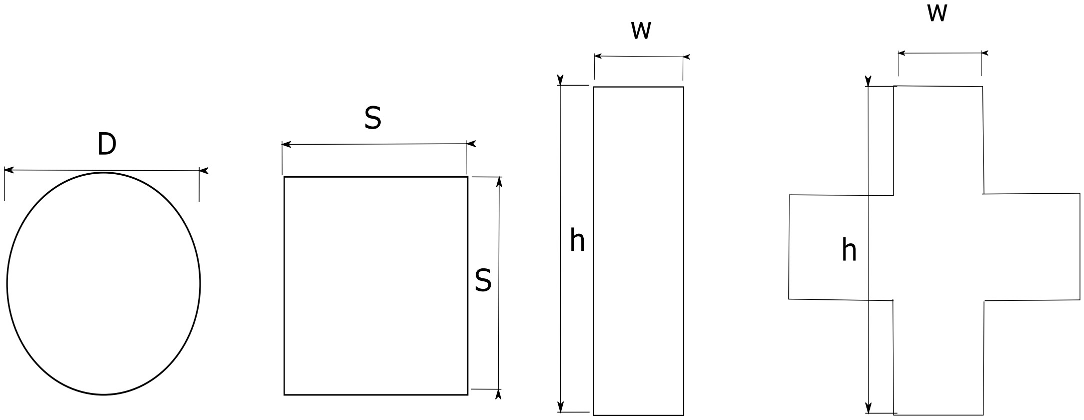

Figure 4.12: Cross section of the extra geometries that will be compared to the axisymmetric case (circular cross section).

For this section we will look at three additional geometries for insertion. Figure 4.12 shows the different cross-section geometries that we will be exploring: a square, a rectangle, and a cross. In the previous case for the circular cross section, the axisymmetric case, we did not need to define an exact axis. Now we will define all cross-sections axis as shown in Figure 4.12. As for the wedging and jamming diagram dimensions we will have to extend the models to both planes, the $x - z$ and $y - z$ plane. We will limit our comparison between the geometries to the limits in error for wedging and jamming, Figures 4.8 and 4.9. We will also limit our analysis to pegs without corners. Corners require additional analysis for the wedging diagrams as they will require multi-dimension analysis instead of the simplified model we will be using. This additional analysis has been done for the square case by Meitinger [28].

To begin our analysis we need to define a metric to compare the different geometries. The best metric to set constant for all geometries would be the surface area of the hole. This is because of regardless of the geometry there will be the same number of points in contact at the same depths. Since the depths will be identical for all geometries we will focus on looking at the perimeter for each geometry and set these permiters equal to each other. Starting with the circular cross sections as a base we have the following relationship.

$$\pi D = 4S = 2h + 2w = 8h - 4w \tag{4.31}$$

where $D$ is the diameter for the circle, $S$ is the square length, $h$ is the height of the rectangle, and $w$ is the width of the rectangle. We will determine all of these parameters in terms of $D$ and apply all of the previous jamming and wedging models to each of the geometries. To simplify the rectangle and cross cases we will make the width $w$ some fraction of the height, $w = h/k$, which will be treated as a known constant. From this we get the following effective lengths for each cross section.

$$\begin{aligned} H &= \frac{\pi}{4} D \approx .79D && (4.32)\\ h_{rect} &= \frac{\pi}{2 + \frac{2}{k}} D && (4.33)\\ h_{cross} &= \frac{\pi}{8 - \frac{4}{k}} D && (4.34) \end{aligned}$$

We can see that if $k = 1$ we will get back the same relationship for a square so we will determine the lower bound for the rectangle and the cross. Doing this we find the following inequalities.

$$\frac{\pi}{2}D > h_{rect} > \frac{\pi}{4}D \tag{4.35}$$

$$\frac{\pi}{8}D < h_{cross} < \frac{\pi}{4}D \tag{4.36}$$

From this we can also determine the bounds on the width. For both cases as k approaches infinity we see that the width approaches zero. The respective inequalities for the width are as follows.

$$0 < w_{rect} < \frac{\pi}{4}D \tag{4.37}$$

$$0 < w_{cross} < \frac{\pi}{4}D \tag{4.38}$$

Note that the left sides of (4.35)-(4.38) correspond to the same limits, where $k \to 0$, as well as the right side, where $k = 1$.

We can also apply these same constraints on the peg. For these three geometries we would get the same values with respect to the peg's diameter $d$. From this we can extend this model to compare the jamming and wedging for each geometry. Starting with wedging we have the lateral error limit for the circular cross-section as $\epsilon = \frac{D-d}{2}$ and the rotational error was $\theta = \frac{CD}{\mu d}$. We can see from these equations that for wedging the only change in the limits will be in the lateral error; this is because the clearance factor will not change for any of these cases.

Since the change in limit will be some factor we will treat the new lateral error as $\epsilon_{square} = a\epsilon$, for the case of the square $a = \frac{\pi}{4}$. Figure 4.13 shows these change in lateral error for the three cases with respect to the circular cross section. From figure 4.13 we can see that the area where no wedging occurs is also scaled by the same factor depending on geometry. This means that there is even less allowable

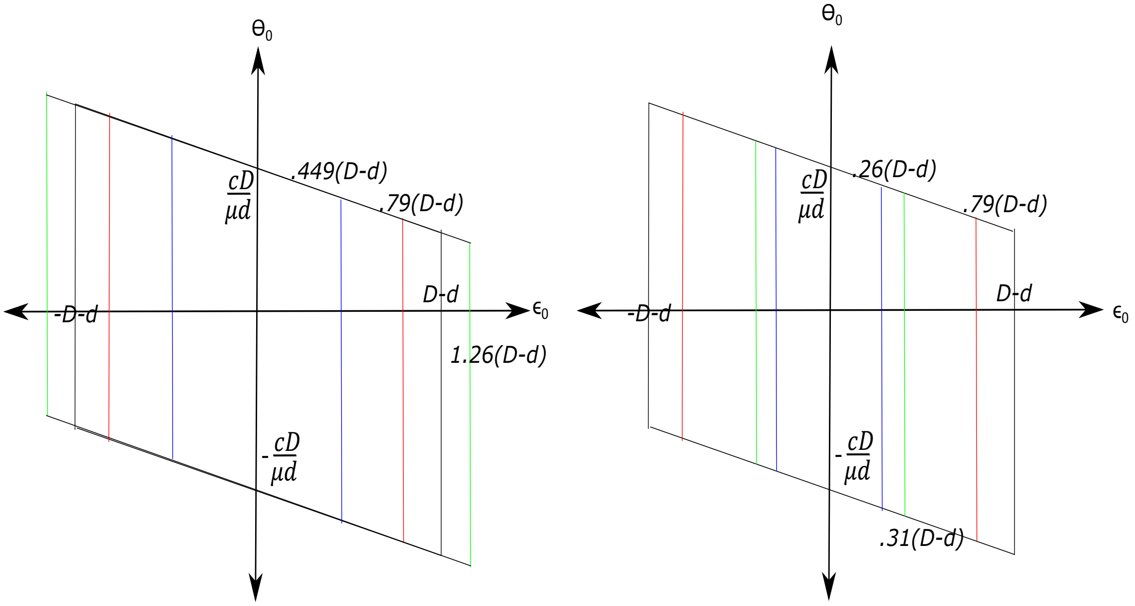

Figure 4.13: Change in the wedging diagram for the various geometries. The black line is for the circle, the red line is the square, the green line is the rectangle, and the blue line is the cross. The two graphs correspond to the wedging for the two different planes. These graphs correspond to when $k = 4$.

errors for a successful insertion. We will again use this area of no wedging as a base for the other geometries. However, this only applies to one plane, $x - z$ or $y - z$, so we will have to find the area with respect to both planes. Recall that the width is defined as a friction of height, $w = \frac{h}{k}$

$$A_{square} = \frac{\pi}{4} A_{circ} \quad A_{square} = \frac{\pi}{4} A_{circ} \tag{4.39}$$

$$A_{rect} = \frac{\pi}{2 + \frac{2}{k}} A_{circ} \quad A_{rect} = \frac{\pi}{2k + 2} A_{circ} \tag{4.40}$$

$$A_{cross} = \frac{\pi}{8 - \frac{4}{k}} A_{circ} \quad A_{cross} = \frac{\pi}{8k - 4} A_{circ} \tag{4.41}$$

We can see that for the square and the cross geometries the area for no wedging is smaller than that for the circular cross section. The one exception is that in one dimension for the rectangle there can be an area that is larger than the circle baseline, so long as $k > \frac{2}{\pi-2}$. The issue is that the area for the other dimension, width or height, will then be less than $\frac{\pi}{2} - 1 \approx .57$ of the circle's area. So even if we make one dimension easier for insertion compared to the circular cross section we significantly increase the difficulty for the other dimension. For the wedging it is easy to see that the circular cross section is the easiest geometry for insertion, the next being the square which has 79% of the success area. To determine whether the rectangle or the cross is the more difficult insertion we find the Euclidean distance.

$$A_r = \frac{\pi}{2+\frac{2}{k}} A_{circ} \sqrt{\frac{k^2+1}{k^2}} \tag{4.42}$$

$$A_c = \frac{\pi}{8-\frac{4}{k}} A_{circ} \sqrt{\frac{k^2+1}{k^2}} \tag{4.43}$$

From this it is clear that the rectangle insertion will be easier than a cross insertion. With this wedging analysis, we see that the accuracy of the position and pose of the insertion is more important for these different geometries.

Next we will look at how these different geometries affect the success with respect to jamming. To do this we will use Whitney's jamming parameter, $\lambda = \frac{z}{\mu D}$, for the case of a circle. Figure 4.9 shows that the horizontal axis will be bounded by the friction so it will not change. To find these new jamming parameters we will scale $\lambda$ using the relationship from equations (4.32)-(4.34).

$$\lambda_{square} = \frac{4}{\pi}\lambda \tag{4.44}$$

$$\lambda_{rect} = \frac{2+\frac{2}{k}}{\pi}\lambda \tag{4.45}$$

$$\lambda_{cross} = \frac{8-\frac{4}{k}}{\pi}\lambda \tag{4.46}$$

From this we see the opposite relationship as wedging; the geometries that require more accuracy to prevent wedging are easier to prevent jamming. This is because smaller holes for insertion will assist the object being inserted. The issue with this is that a smaller clearance parameter means an even more likely chance for wedging to occur. This also means that the area for the jamming cross section will be larger than the circles jamming for the more complicated geometries.

Since we will be controlling the compliance of the robot we should expect less difficulty of insertion once the one-point contact stage is reached. We should expect significant difficulty preventing wedging for these additional geometries. In other words, initial insertion for complicated geometries will pose greater difficulty but once wedging is prevented the insertion will be easier.

## 4.3 Key Insertion Modeling

Continuing to use the geometry models from the previous section we will begin at looking how to model a keyhole geometry. Figure 4.14 shows the geometry for a keyhole. As in the previous section we will look particularly at the increased difficulty in wedging. We will again constrain the surface area of the geometry to be equal to the cross section of the circle case.

To simplify the keyhole model, the keyhole will be a combination of rectangles. For the model in figure 4.14 the thinnest width, $t_w$, is the only factor that affects

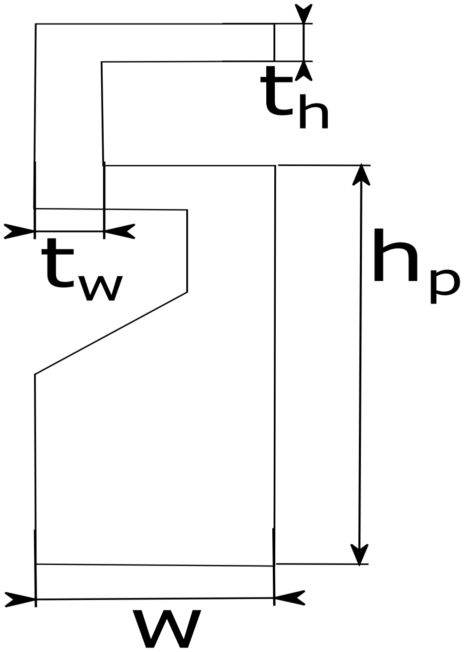

Figure 4.14: Cross section of key hole model

the surface area for the keyhole. This means the height and width of the simple keyhole geometry will be a function of this parameter. We will define this width as a percentage of the width.

$$t_w \quad = \quad a * w \tag{4.47}$$

where $a$ is between the values of (0 1) and $h$ is the total height of the rectangle and $w = \frac{h}{k}$ is the total width.

We define the surface area for the keyhole and the circle cross section as the following.

$$\pi D = 2(h + \frac{5h}{k} + \frac{4a}{k}) \tag{4.48}$$

which means that wedging bounds for the height and the width now become .

$$\frac{\pi}{2}D > h_{rect} > \frac{\pi}{4(3-2a)}D \tag{4.49}$$

$$0 < w_{rect} < \frac{\pi}{4(3-2a)}D \tag{4.50}$$

In the case that $a = 1$ the key hole becomes a rectangle and has the same bounds as our rectangle geometry. However, since $a$ ranges from (0 1) we can see that the wedging bounds are smaller than the rectangle geometries. In the case where $a \to 0$ the wedging bounds get three times smaller than the rectangle case. From these bounds we can see that the key hole insertion can be as difficult as the rectangle case or three times more difficult.

Similar to the jamming relationship defined in the previous section, the jamming parameter will become much larger now. Again we will be using the Whitney jamming parameter $\lambda = \frac{z}{\mu D}$. In this case, wedging becomes three times more difficult. The jamming will then be as easy or three times easier.

$$\lambda_{keyhole} = \frac{2(1 + \frac{5-4a}{k})}{\pi}\lambda \tag{4.51}$$

From this key hole model we can see that the wedging model has become significantly harder than the rectangle model as well as the cross model, but the jamming is easier than the rectangle model. In actuality this keyhole insertion is much more difficult since the corner effects have been ignored and the key hole was simplified to this geometry. We will be using this simplified rectangle model for our insertion model as we complete our key insertion.

# Chapter 5

# Visual Position Impedance Controller

As discussed in Chapter 2, there are many different control strategies for compliance controllers. This thesis will focus on impedance control; impedance control is a method that allows the robot to change its impedance and admittance of the environment through contact with the environment. An impedance controller is capable of simultaneously managing a relationship between the position and velocity of the robot's end effector and the forces applied by the environment. Some impedance controllers also provide the additional benefit of eliminating the need for inverse kinematics when used on redundant robots, i.e., robots with more than 6 DOF. This chapter will first discuss the position based impedance controller introduced by Hogan [14], along with a vision system to be used with the controller. Then simulation results of the controller will be shown using various stiffness values for the modeled robot. The controller will move to specified points to test the accuracy, along with the improved accuracy provided by the vision system. Finally the controller will complete various object insertions and we will analyze the controller responses during these insertions.

## 5.1 Impedance Controller Modeling

This section presents the theory used in modeling the standard Hogan impedance controller, the position based impedance controller. The first step in designing an impedance controller is defining a relationship between the force output and the resulting displacement of the end effector in Cartesian coordinates. This requires the robot to have joints that are controlled by commanded torques, $T$, encoders capable of reading joint angles, $\theta$, and known forward kinematics, $L$, of the robot to transform each joint position to the end effectors Cartesian position, $X = L(\theta)$. For a robot that has these capabilities, the impedance controller will be capable of following a desired trajectory with reasonable performance as well as interacting with external forces from the environment. The benefit of this type of controller is the ability to transition between stiffness values during contact and when there is no contact. The effective stiffness is a control gain that defines the relationship between the Cartesian position and the control force applied by the end effector. The effective stiffness $K$ has the following relationship with the force applied to the end effector

$$F = K[X_0 - X] \tag{5.1}$$

where $X_0$ is the actual position for the end effector and $X$ is the goal position.

Equation (5.1) is clearly similar to the force model for a spring, $F = Kx$. From this we can see that we can model the robot's end effector as a combination of six linear springs for the six DOF in Cartesian space. We typically break up this stiffness into the positional stiffness, $K_x$, and the pose stiffness, $K_\theta$.

Next we need the Jacobian matrix $J(\theta)$. The Jacobian matrix is a matrix that relates the robot's joint velocities to the Cartesian velocity, $dX = J(\theta)d\theta$. From the virtual work principle, the joint torques can be related to the force necessary to carry out the desired motion by using the Jacobian's transpose, $T = J(\theta)^T F$. Combining these definitions with equation (5.1) we can relate the Cartesian position to the joint torque.

$$T = J(\theta)^T K[X_0 - X] \tag{5.2}$$

Equation (5.2) relates the joint torque to the desired stiffness with the associated trajectory for the end effector. Since this only includes the relationship to the position we need to introduce the similar relationship between the force applied by the end effector and the velocity of the end effector. As the position relationship paralleled to a spring stiffness, the velocity relationship will be similar to damping $B$. The damping of the end effector can also be controlled to modify the robots response to velocity errors. This force and velocity relationship is shown in equation (5.3).

$$F = B[V_0 - V] \tag{5.3}$$

where $V_0$ is the actual velocity and $V$ is the goal velocity.

The above relationship with the Jacobian matrix can also be used to relate the velocity to the joint angular velocity, $V = J(\theta)\omega$. We can again use the principle of virtual work to relate the torque to the force and again combine these relations with (5.3).

$$T = J(\theta)^T B[V_0 - V] \tag{5.4}$$

This controller model is not finished yet because the controller has no means of compensating for the robot's own weight. Next we introduce a gravity compensation model to keep the robot from falling under its own weight. The impedance controller also accounts for the inertial effects from the robot's limbs. To simplify modeling these extra terms, the robot is assumed to follow rigid body motion. This allows the controller to use predefined mass and moments about the link. To do this we model the robots mass, $M$, and the inertia, $I(\theta)$, matrices for the impedance controller. The mass and inertia information for this robot is already well defined and determined by the manufacturer. However, the WAM is a redundant robot, has an extra degree of freedom, so we need to use a null space controller. The null space controller makes it possible to use an invertible Jacobian, $J^{-1}$, and limit the torque model to six joints. Combining the position, velocity, inertia, and mass into a single control equation yields an equation to define the torque by each joint of the robot using desired positions and velocities.

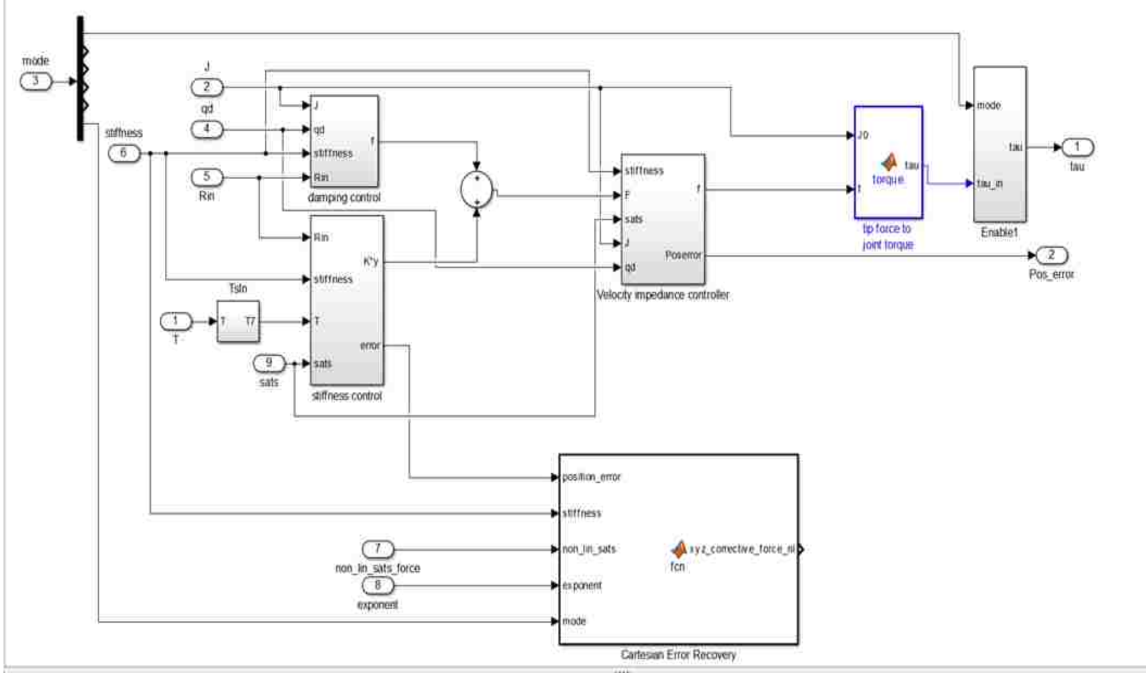

Figure 5.1: This Impedance Controller includes the additional velocity impedance term. We can see the damping forces and the stiffness forces being sent to the velocity impedance controller which outputs the force to be converted to torque for the robot

$$
\begin{aligned}
T &= I(\theta)J^{-1}M^{-1}K[X_0 - X] + I(\theta)J^{-1}M^{-1}B[V_0 - V] + I(\theta)J^{-1}M^{-1}F \\
&+ S(\theta) + V(\omega) - J^T(\theta)F + C(\theta,\omega) - I(\theta)J^{-1}(\theta)G(\theta,\omega) \qquad (5.5)
\end{aligned}
$$

where $S(\theta)$ is the gravity compensation, $V(\omega)$ is the velocity dependent torques, $G(\theta,\omega)$ is the accelerative coupling terms, and $C(\theta,\omega)$ is the inertial coupling terms [14].

In equation (5.5) the values are either known, controllable, or actively determined values. The two control parameters, $K$ and $B$, will be varied for performance specific values. As such, the two parameters also get written into the reflective memory for the robot's onboard computer to use. This allows the control computer to vary these parameters as needed.

With this we have a full model for our impedance controller, which we will implement in *Simulink*. Figure 5.1 shows the structure of the impedance controller. The *Simulink* model that implements the impedance controller, gravity compensation, and null space controller is shown in Figure 5.2. This model is compiled in *Simulink* and sent through the xpctarget to the reflective memory which is sent to the WAM target computer at a rate of 200Hz.

## 5.2 Vision Modeling

The vision system will be integrated into the control scheme as shown in figure 5.3. Here we have the vision controller correct any errors during motions. Later in this chapter we will compare the response between the impedance controller without the vision system and with a vision system.

Before we can begin using a vision controller we need to ensure that our camera is

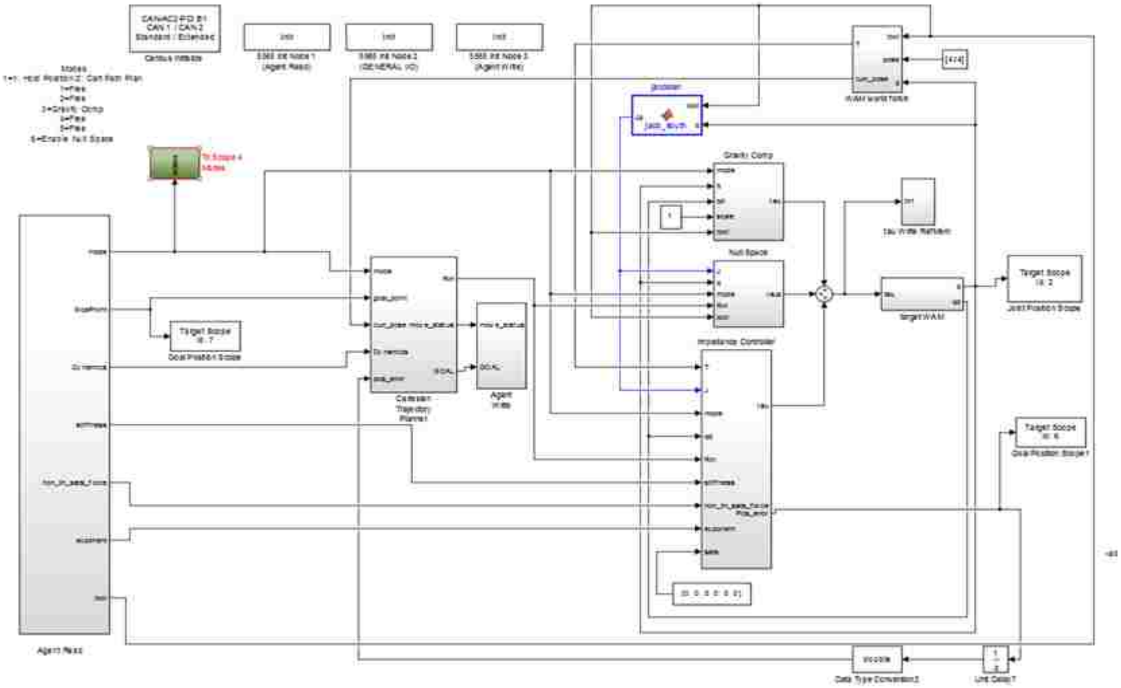

Figure 5.2: This is the entire controller including the gravity compensation and a null-space controller. This also includes blocks where the Jacobian and forward kinematics are determined.

completely calibrated. As mentioned in 2.1.3, camera calibration can be done using a calibration tool. Matlab provides an easy to use camera calibration app that requires more than 10 images taken from the camera at various distances and orientations. In our case both cameras are stationary and the calibration object is moved for each image. All of the intrinsic calibrations are completed prior to the experiments. For the extrinsic parameters, the depth of objects from the camera, we also have an accurate knowledge of the setup ahead of time. To improve the vision controller's accuracy, the extrinsic parameters will be determined by the geometric constraints of the robot hand. Using these constraints we can have an accurate estimate of the depth as the robot's depth will change during the motion.

The intrinsic parameters are the focal length $f$ and the principal point $(u_0, v_0)$, with respect to the pixel coordinate system. Here we treat the focal length as a

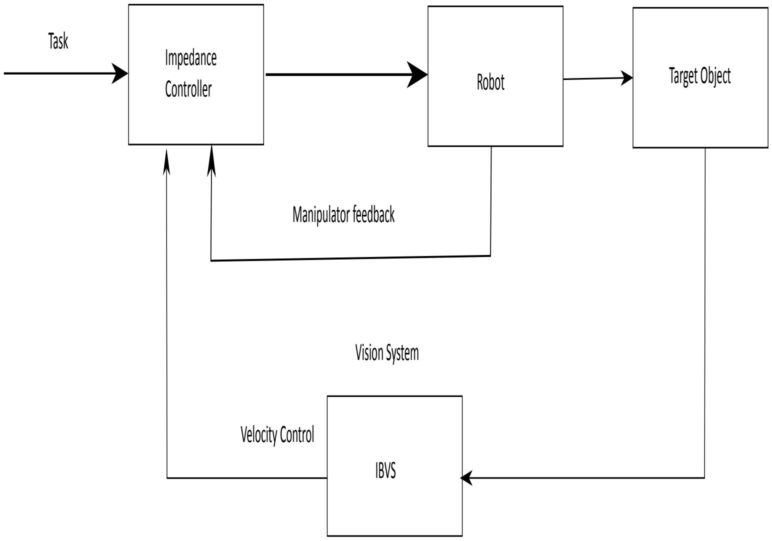

Figure 5.3: Vision controller integrated with the impedance controller

vector $[fx, fy]$ to also represent the pixel width and height scaling with the focal length. We will define the depth of the camera as $Z$, as well as the pixels along the width $u$ as $X$ and the pixels along the height $v$ as $Y$. Figure 5.4 shows the geometry between the two coordinate systems. The following equation can represent the global position from the pixel point.

$$X = \frac{u - u_0}{Zf_x},\ Y = \frac{v - v_0}{Zf_y} \tag{5.6}$$

Now that we have a way to control the positions of the robot with vision we need to work on controlling the pose with vision. We are going to need to implement some feature detection tools to determine the orientation of our objects that we will insert. For feature detection we will use the method of subtracting the current image to a base image to detect any new objects in the image. When we do this we can convert a grayscale image, an image where each pixel is indexed from 0 to 255, into a

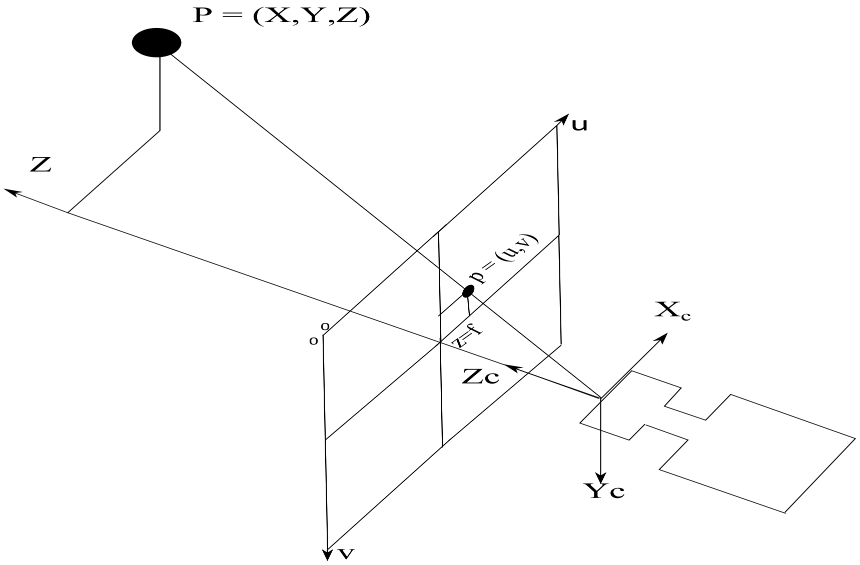

Figure 5.4: Camera coordinate systems. The global point is (X,Y,Z) and the image location is (u,v).

binary image. With the binary image we can detect regions and determine features from these regions such as area, centroid, bounding box, eccentricity, and major and minor axis.

To determine the orientation of the peg we will use the region feature to determine the orientation similar to finding the centroid and bounding box. Doing this in Matlab, we create an ellipse around the major axis, the long diagonal of the bounding box, and the minor axis, the short diagonal length. The orientation is determined by the angle made between the u-axis, or the horizontal axis, to the major axis. For simplification the angle is from $[-\frac{\pi}{2},\ \frac{\pi}{2}]$. For example, Figure 5.6 highlights the ellipse around the detected peg. In this example the angle was found to be around $-83°$, or 1.45 radians.

From this angle we can determine the orientation offset, and since we know the

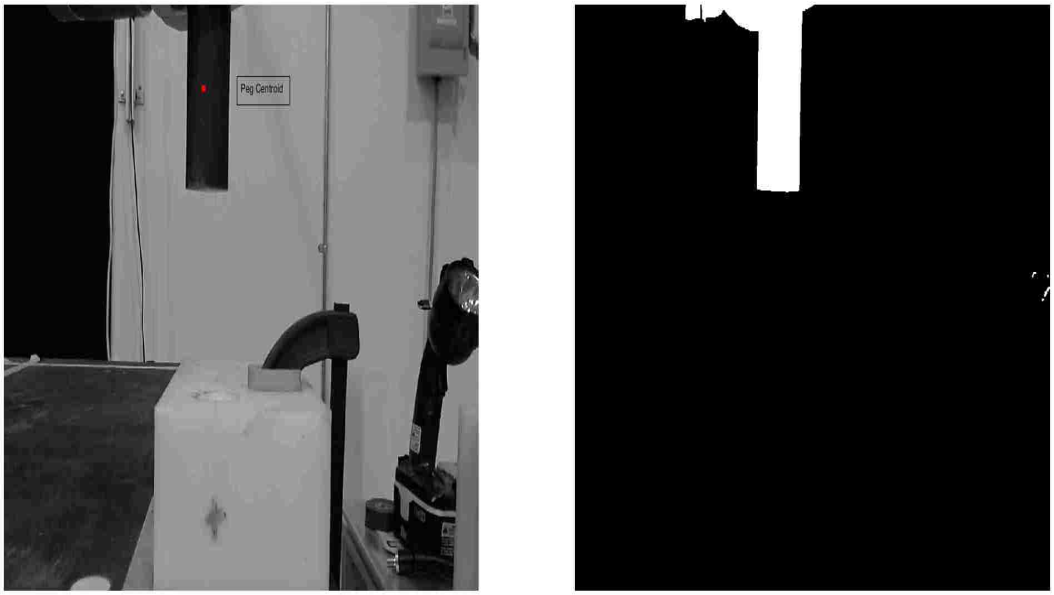

(a) Image with Peg and Centroid detected

(b) Binary image of peg detected

Figure 5.5: The images show the peg being detected and the region where all the parameters including the centroid location are being determined.

camera's location with respect to the WAM, we can now implement a vision controller that will integrate with the impedance controllers.

## 5.3 Controller Simulation of Single Joint

For this section we will simulate the impedance controller response for a single joint. We will treat a single joint as an actuator with inertia, $I_a$, and internal friction, $B_v$, or $F = I_a s^2 + B_v s$. From this simple model we can expand the single joint model to the rest of the robot. We will be testing the effects of a straight forward impedance controller, i.e., no feedback filter function.

Figure 5.7 has a simulink model of the position impedance method without the

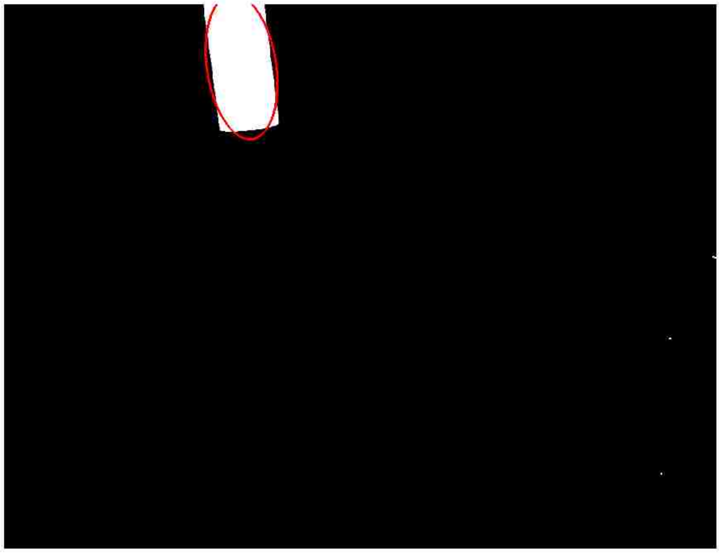

Figure 5.6: Ellipse highlighting detected peg.

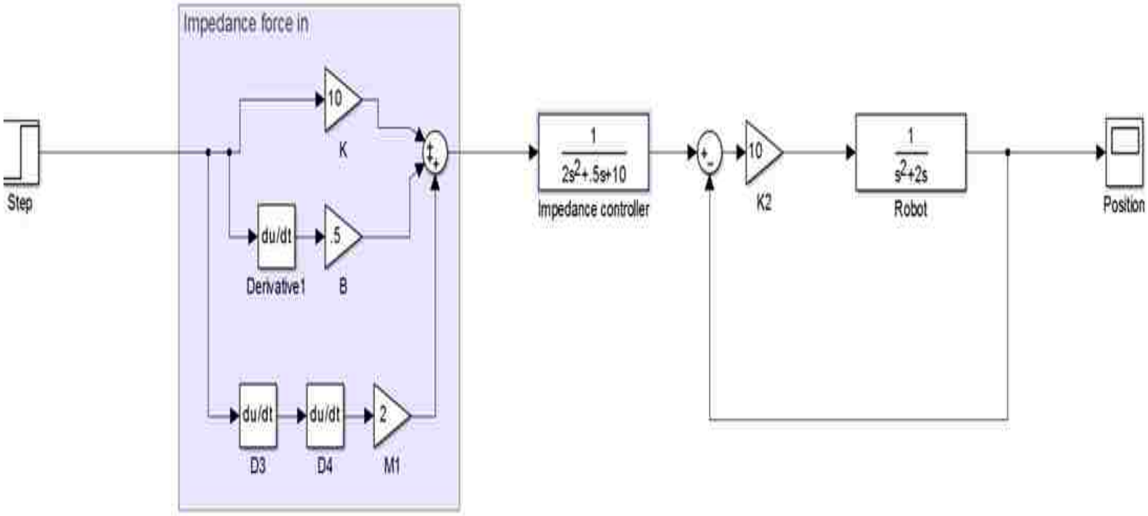

Figure 5.7: The simulation model for the position impedance method. Note there is no feedback function. Impedance controller is directly applied to the joint. In this model the environment is not acting on the controller.

environment acting on the controller. In this example the stiffness is $K = 10$, the damping is $B = 0.5$, the mass is $M = 2$, the inertia $I_a = 1$, and the internal resistance is $B_v = 2$. This model is for pure simulation purposes as the actual robot has varying inertias and unknown internal resistances for each joint. This simulation model is simply to test the controller's response without the environment acting on the controller and with the environment acting on the controller. Figure 5.8 shows the controller model with the environment acting on the controller. In this model we are treating the environment as a mass-spring-damper system

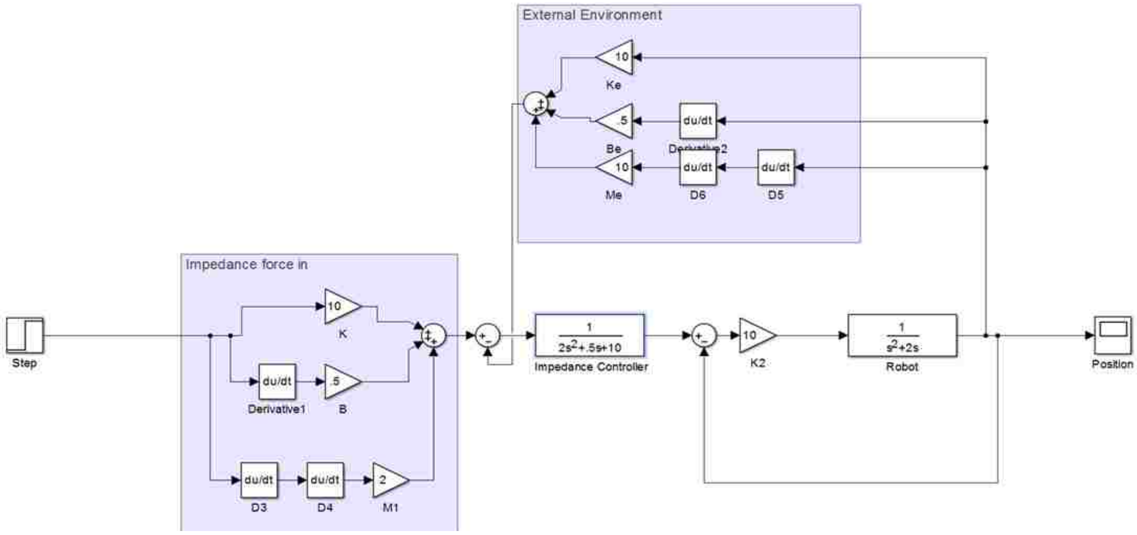

Figure 5.8: The simulation model for the position impedance method. Note there is no feedback function. Impedance controller is directly applied to the joint. In this model the environment is acting on the controller.

Using these simulation models we can find the Laplace transformation for both cases.

$$\frac{x_{out}(s)}{x_{goal}(s)} = \frac{k_p}{I_a s^2 + B_v s + k_p} \tag{5.7}$$

for the response without the environment acting on the controller. And the response with the environment acting on the controller is the following.

$$\frac{x_{out}(s)}{x_{goal}(s)} = \frac{k_p(Ms^2 + Bs + K)}{I_aMs^4 + I_aBs^3 + [k_p(M + M_e) + BB_v]s^2 + k_p(B + B_e)s + k_p(K + K_e)} \tag{5.8}$$

where $M_e$ is the environment's mass, $B_e$ is the environment's damping, and $K_e$ is the environment's stiffness. From (5.7) the impedance controller will always be stable with steady state error. This response is the ideal 2nd order response from a joint and is easily controllable. However, (5.8) shows that this controller will have trouble with the environment acting back on the controller. Using the Routh-Hurwitz stability criterion we see that (5.8) remains stable when $\frac{M_e}{M} + \frac{B^2B_v}{k_p} > \frac{B_e}{B}$ and when $B[k_p(M + M_e) + BB_v](B + B_e) > Mk_p(B + B_e)^2 + B^2I_a(K + K_e)$. Looking at the first stability criterion, we see that the ratio between the environment's mass to the controller's mass needs to be larger than the damping ratio. From the second stability criterion, we see that a high stiffness environment will also cause the controller to become unstable.

We will now look at the response from both responses, starting with the response without the environment.

From Figure 5.9, we get the expected second order position response. This is to be expected since (5.7) is the standard 2nd order response. Now let us look at the response of the controller with the environment acting on the controller

Figure 5.10 shows the response with environment parameters $M_e = 10, B_e = 0.5$, and $K_e = 10$. Here we see that although the system is stable the response is slow and chatters. The main difference with this model, (5.8), compared to the model without the environment, (5.7), is that the controller is capable of actively varying the stiffness and damping terms during the motion. This is a very important aspect of the impedance controller as this changes the location of both the poles and zeros in (5.8). The issue with this controller, as shown from the second stability term, is that if the robot or the environment has high stiffness the controller will go unstable.

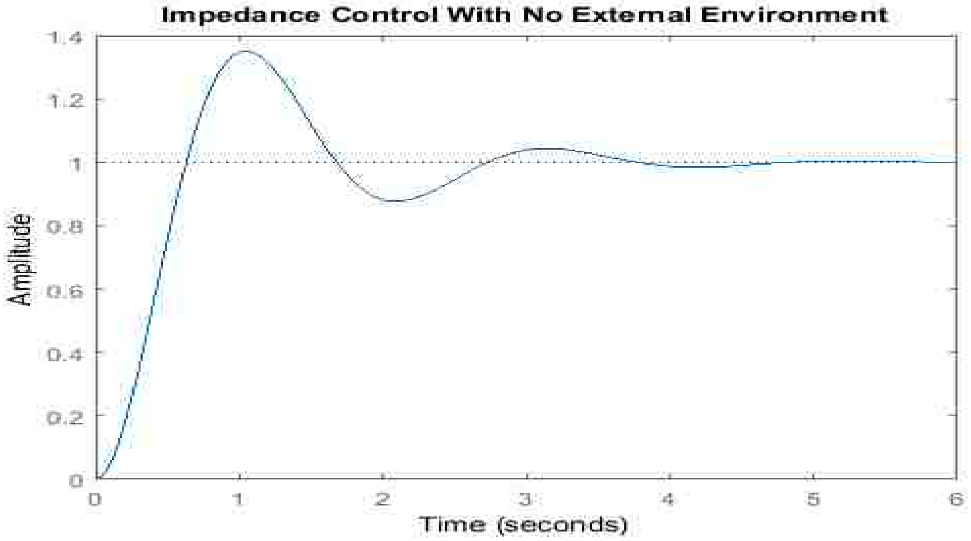

Figure 5.9: The impedance controller response without environment.

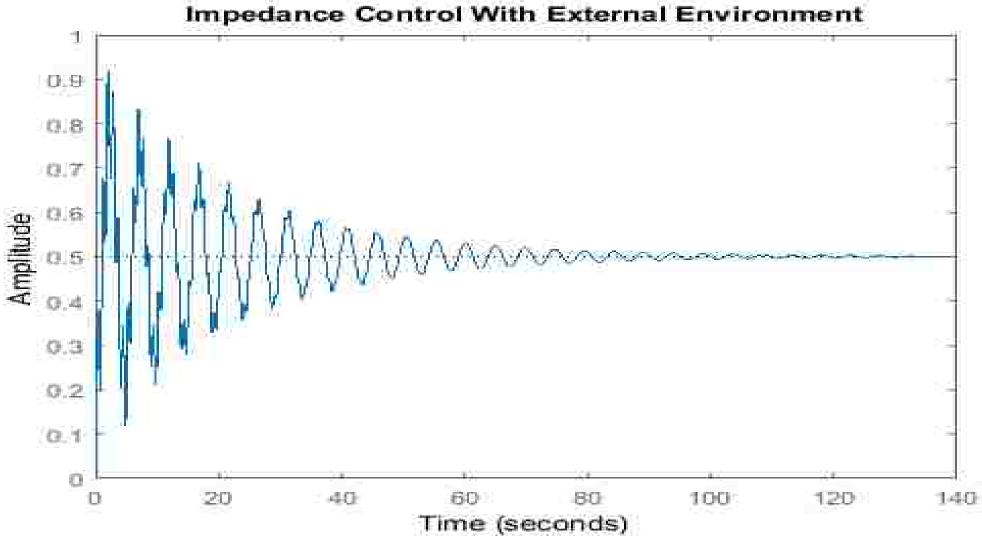

Figure 5.10: The simulation model with environment acting on controller.

Figure 5.11 shows a response of the controller when the environment's stiffness is changed to $K_e = 100$.

Here we see out system going unstable by increasing the stiffness of the environ-

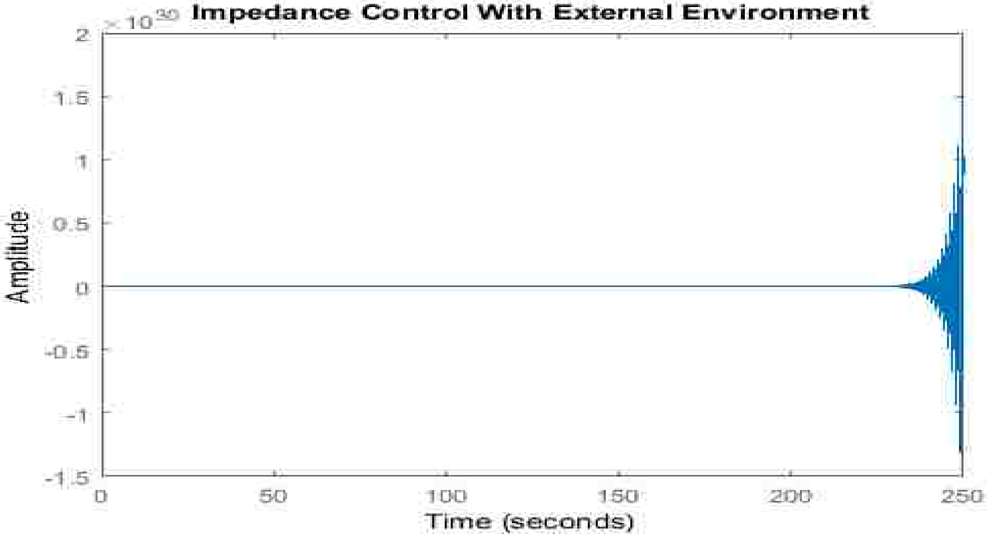

Figure 5.11: Unstable response from an environment with high stiffness.

ment acting on the robot. Using the stability criterion we see that if we decrease the impedance stiffness, i.e, become more compliant, we will be able to maintain stability. By varying these parameters we can account for the environments we will interact and change these impedance parameters.

## 5.4 Controller Response

For this section we are going to compare the different responses of the position impedance controller. Before we start with the analysis of the impedance controller we will be using stiffness and gain values that have been tested. [48] In this thesis the WAM position impedance controller was found to maintain stability at positional stiffness of $K_x = K_y = K_z = 1000$ and pose stiffness $K_{\theta x} = K_{\theta y} = K_{\theta z} = 1$. As for the damping, varying the damping causes the response to be unpredictable so the author found the following values to be the best: $B_x = 15, B_y = 10, B_z = 5$ and $B_{\theta x} = B_{\theta y} = B_{\theta z} = 0.1$. We will use these same stiffness values to later compare both the position and velocity impedance methods.

### 5.4.1 Non-Contact motion

For the first experiment we are going to look at the position impedance controller and velocity impedance controller response to the same goal. Since both controllers will not start at the exact same location in space, the distance from the starting point to the goal point will be scaled. First, let us look at the response of the controller's position.

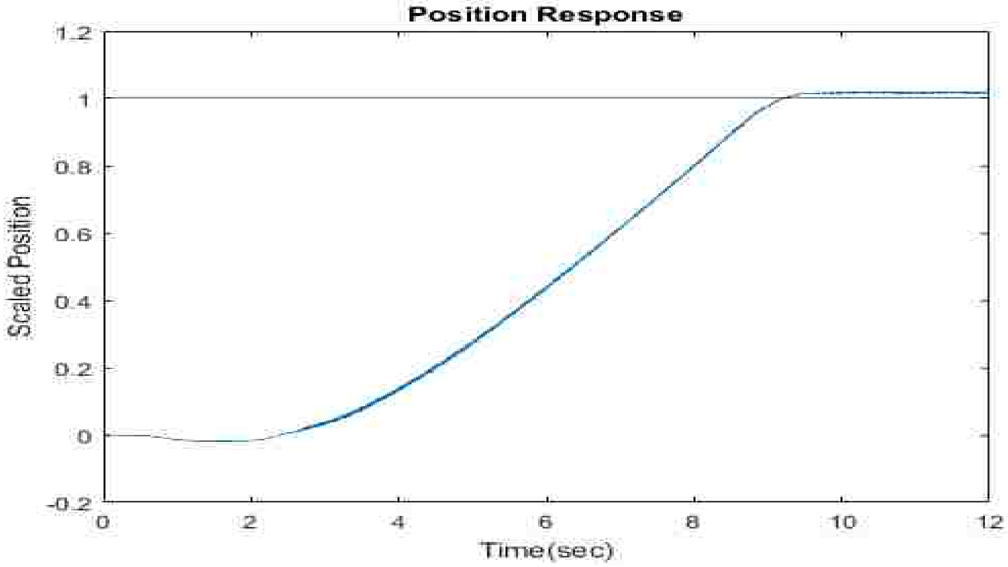

Figure 5.12: The scaled position response of the position based impedance controller (blue) and the goal (black).

In Figure 5.12 we see the response of the position impedance controller. The positional stiffness values for the controller are: $K_x = K_y = K_z = 1000$, and the pose stiffness values are: $K_{\theta x} = K_{\theta y} = K_{\theta z} = 1$. The damping values for the controller are: $B_x = 15, B_y = 10, B_z = 5$ and $B_{\theta x} = B_{\theta y} = B_{\theta z} = 0.1$. These values were chosen since these values are the largest stiffness values where the controller response was still stable. The impedance controller has some visible chattering in its response which shows that these stiffness values are the highest this controller can handle. This chattering is also visible in the Figure 5.10 only the response from Figure 5.12 seems overdamped, likely due to the gravity affecting the controller (which is not modeled in the simulation results).

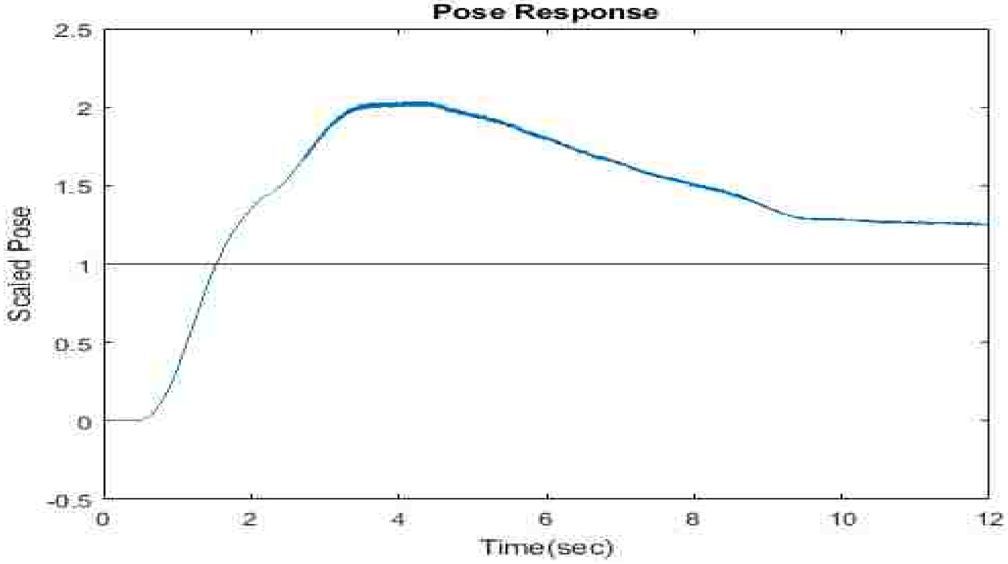

Figure 5.13: The scaled pose response of the impedance controller (blue) and goal (black).

Now let us look at Figure 5.13 which shows the response of the robot's pose, or orientation. We see that this response has more overshoot than the position response and also has a significant amount of steady state error. The error of the pose response is 25%, which is significant when compared to the 1% error from the position response. It has been found that larger stiffness values improve the accuracy response of the controller[48], but with the current standard model these stiffness values are the largest values where the controller is still stable.

Next we are going to look at the controller's response in the dimensions gravity acts against, in this case the $Z$ and $\theta_y$ axis. Figure 5.14 shows both of these responses side by side and we can see that the positional accuracy has less than a 1% of error but again the pose is bad, with 24 % error. In fact, the $\theta_y$ dimension is where most of

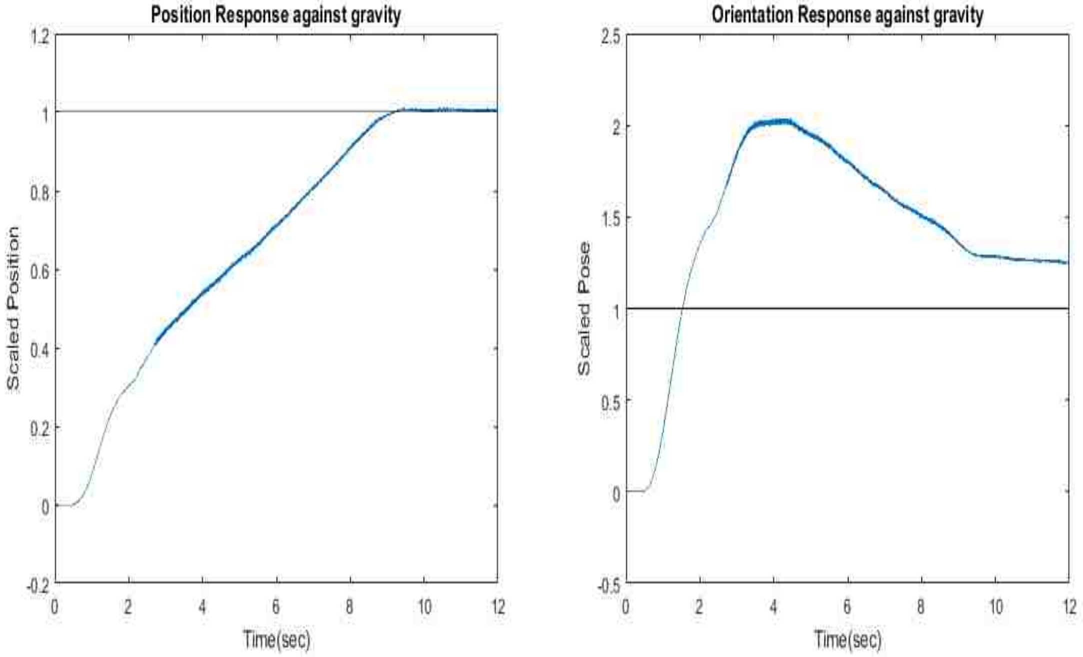

(a) Position response against gravity

(b) Pose response against gravity

Figure 5.14: Scaled response of movements against gravity.

the error from the rotational response. As this is a significant amount of rotational error we will need our vision system to be able to overcome these pose errors in order to have a system that can successfully insert an object without wedging. The pose error can also improve by increasing the stiffness; however, these stiffness values are the largest values where the robot can maintain stability.

### 5.4.2 External Force Response

Next we are going to test the controller by finding the response of the controller when it collides with an object in its path. For this experiment the WAM's hand will run into a secured block that is unable to move, i.e., high stiffness and large mass environment. The robot will continue to plan its path as if the object is not there for this experiment. Because of this we should expect a somewhat linear response after the initial collision. Again in this case we will use the same initial stiffness and gain values from the previous response experiment. We will also look at the response from both controllers at high stiffness values to compare the responses.

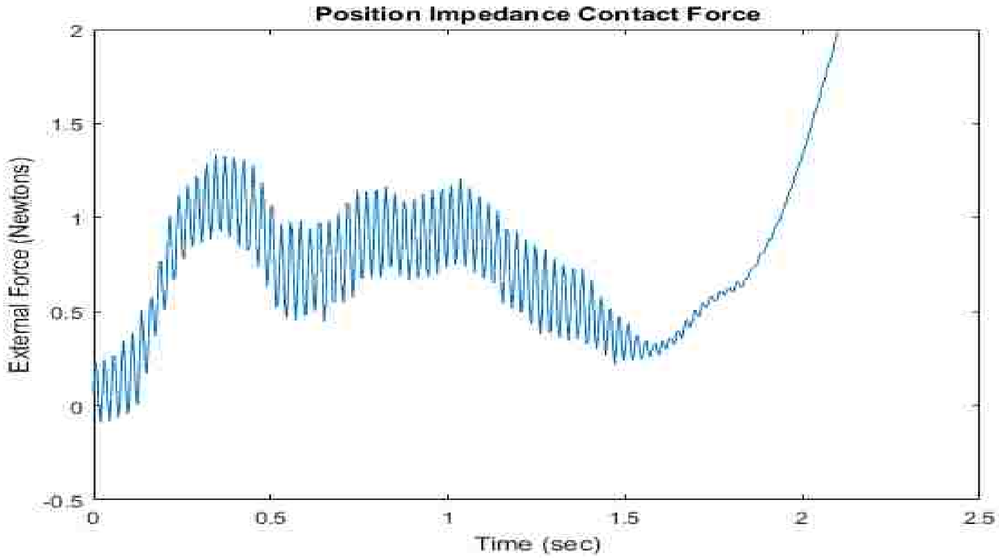

Figure 5.15: The position impedance controller contact force. The stiffness values were set at $K_x = K_y = K_z = 800, K_{\theta x} = K_{\theta y} = K_{\theta z} = 0.1$

The response of the position impedance controller with an object in its path is shown in Figure 5.15. When the robot has initial contact with an object at $t = 0$, the controller nearly becomes unstable. We see noticeable force chattering from the collision, where the robot hand chatters against the object and eventually stabilizes. Eventually the controller recovers and can maintain the disturbance force response. We also see a similar chattering in the robot that was modeled in the position response in simulation. For this response the stiffness was decreased from the previous 1000 value to 800 because the response becomes unstable at the higher stiffness. Figure 5.16 has the position impedance controller response making the same motion with a collision but at the high stiffness of 1000.

What we see in Figure 5.16 is a stable initial contact with the object but then the force quickly becomes unstable. This is expected, as the simulated control response

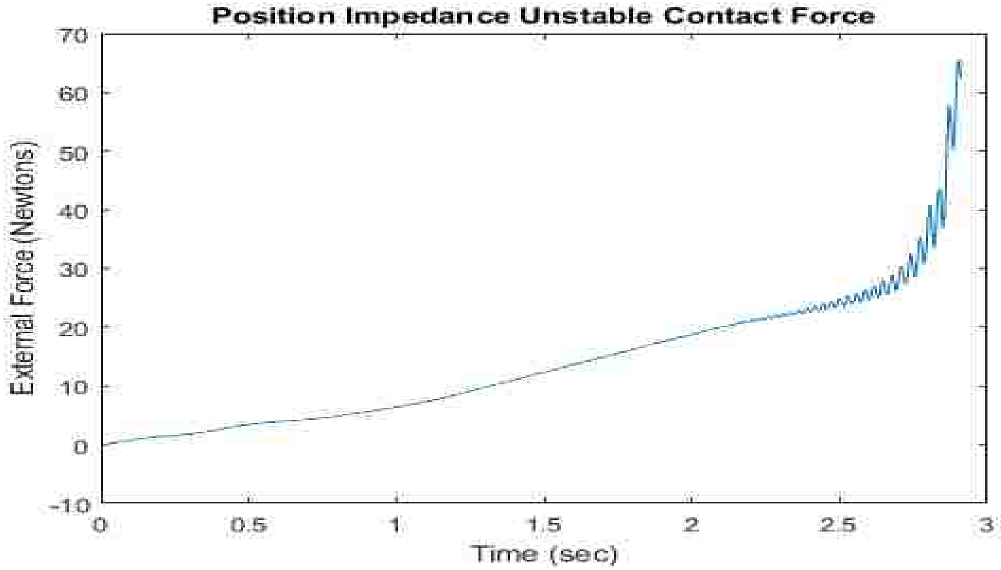

Figure 5.16: The position impedance controller unstable contact force. The stiffness values are set at $K_x = K_y = K_z = 1000, K_{\theta x} = K_{\theta y} = K_{\theta z} = 0.1$

with the environment acting on the controller loses stability when interacting with a high stiffness environment. If a high stiffness environment acts on the controller, the controller needs to decrease its stiffness to maintain stability. This is very important for object insertion since the inserted object will end up making contact with the hole. The frictional forces from the hole will also provide this kind of resistance that can cause the controller to become unstable.

### 5.4.3 Vision Control Response

We will now use the vision system as discussed in section 5.2 to correct the large pose errors. In Figure 5.12, we found the pose error to be mostly from the motions made against gravity. As such, we will focus on the response of the position and orientation moving against gravity.

First, let us look at the the response of a visual impedance controller. In Figure 5.17 we can see that the position acting against gravity loses some accuracy; however,

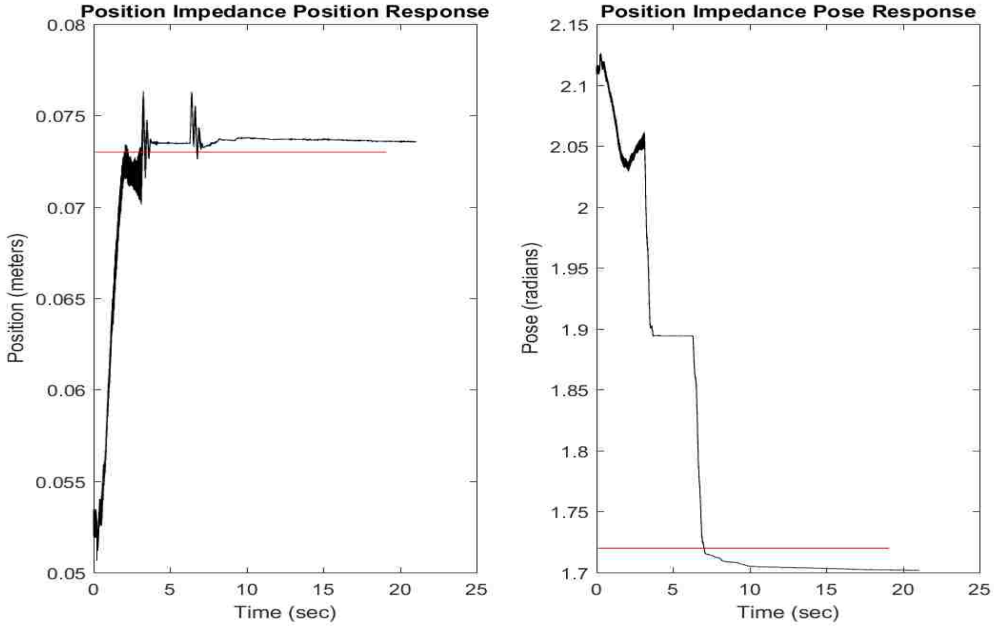

Figure 5.17: Visual position impedance controller response. Stiffness values were set the same as Figure 5.12.

we can see the tremendous improvement in the pose accuracy. We have a large error at the initial impedance response, almost 20%, but with the vision controller the error decreases to less than 1%. The important thing to notice is that we do sacrifice some positional accuracy for pose accuracy but the gain in pose accuracy is important to avoid wedging when inserting objects.

## 5.5 Insertion Testing

In this section we tested insertions for three geometries; circle, square, and cross geometry. Figure 5.18 shows the top view for these three holes that we will be testing, along with their dimensions. For these three insertions we will be looking at insertion with gravity acting along the direction of the insertion force, and insertion with gravity in the direction of the lateral force.

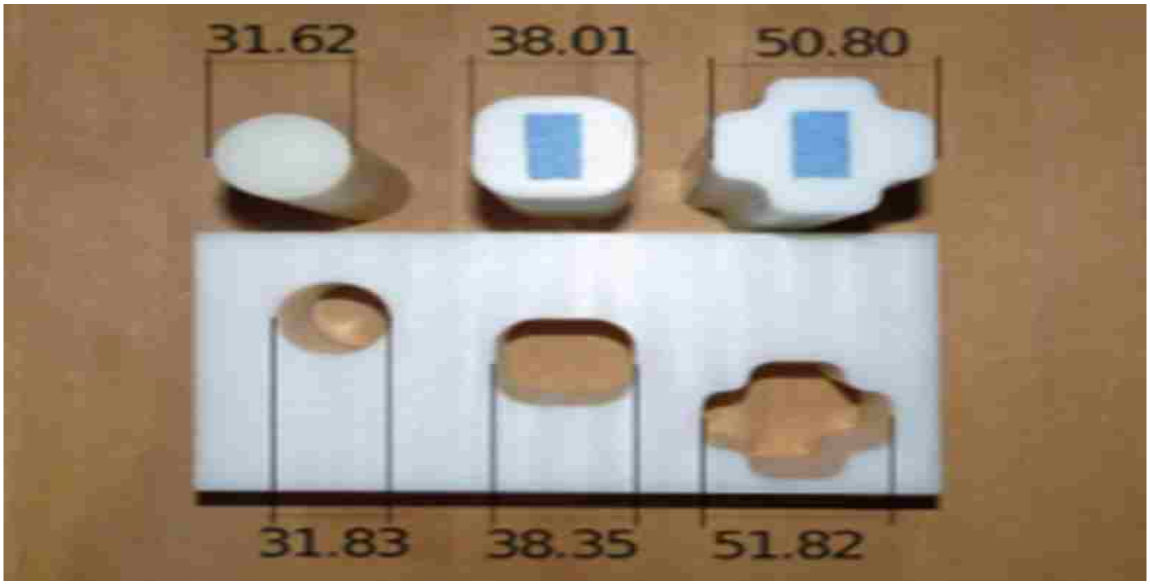

Figure 5.18: Image of testing geometries taken from Gilli *et al.* [11]

As discussed in the previous section, the important compliance parameter is $\frac{K_\theta}{K_x}$. In order to decrease the $\frac{M}{rF_z}$ parameter to avoid jamming we need to decrease $\frac{K_\theta}{K_x}$ as much as possible. The issue with decreasing $\frac{K_\theta}{K_x}$ is that we need to either sacrifice stiffness in pose, leading to more rotational error, or increase the positional stiffness, risking stability. Since the position impedance controller has limited stability we will use its stiffness stability range to define this compliance ratio. After testing the range of stability for the position impedance controller it was found that rotational stiffness of $K_\theta = 0.1$ was the largest possible stiffness during insertion. It was also found that the positional stiffness of $K_x = 500$ is the smallest stiffness where the position error is less than 10%. As such we will define our compliance parameter as the following.

$$\frac{K_\theta}{K_x} = 0.0002 \tag{5.9}$$

For the rest of this thesis we will keep this compliance factor the same for both controllers. For the velocity impedance controller, we will use the same compliance factor but we can increase the stiffness values for both parameters since the controller has a large range of stability, as shown in chapter 4. For the position impedance controller the stiffness values are $K_X = K_Y = K_z = 500$ and $K_{\theta X} = K_{\theta Y} = K_{\theta Z} = 0.1$.

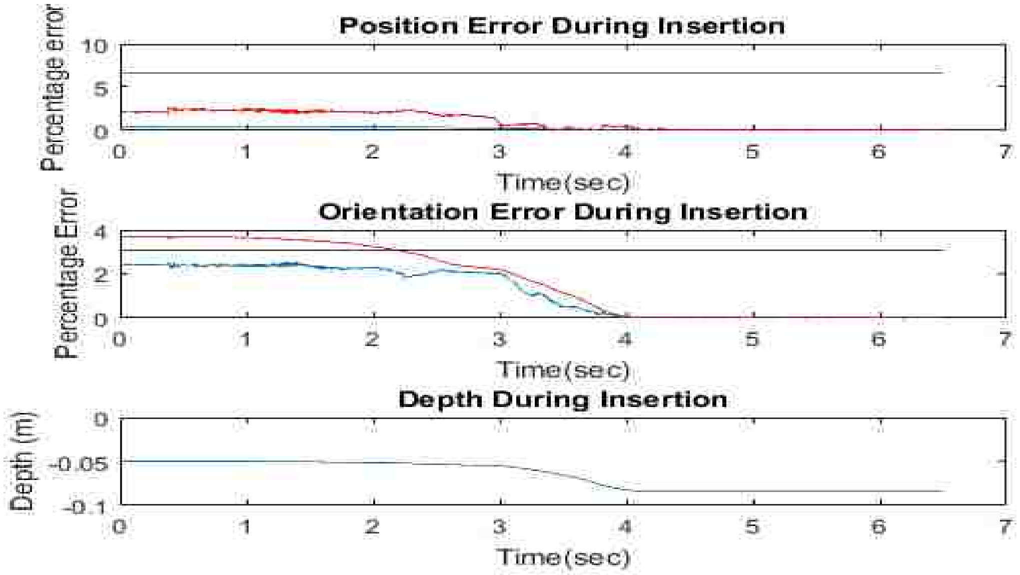

Figure 5.19: Circular peg insertion error. The top graph shows position error, the middle graph shows orientation error, and last graph is the depth during insertion. The red lines correspond the $Y$ and $\theta_Y$ for the top and bottom graphs, respectively. The blue line corresponds to the $X$ and $\theta_X$ coordinate. The black horizontal lines are the maximum allowable wedging value.

### 5.5.1 Circular Peg Insertions

For the first experiment we did the insertion with the circular peg. For this peg we expect fewer wedging issues than the other controllers but for the likelihood of jamming to increase. The controller kept failing from the initial onset of two-point contact, in order to successfully insert the peg it needed to be manually assisted to minimize the initial error for insertion. Figure 5.19 shows the percentage error of

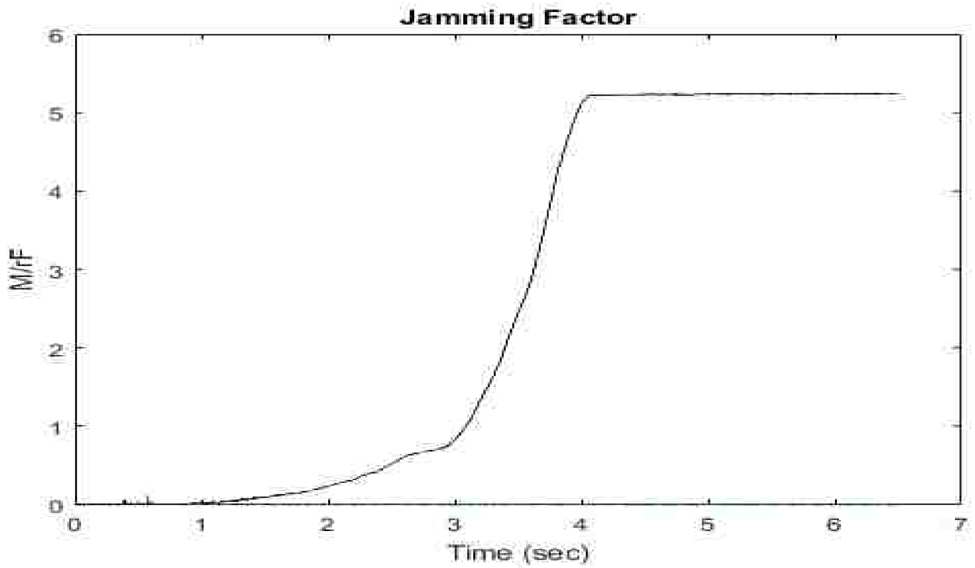

Figure 5.20: Jamming parameter response during insertion. The black line is the jamming parameter varying with the depth and blue line is the jamming response during insertion.

the impedance controller for the circular peg insertion. The black lines correspond to the wedging models maximum allowable error while the red and blue lines are the actual responses. Figure 5.20 shows the jamming parameter, $\frac{M}{rF_z}$, response of the controller during the insertion.

From Figure 5.19 we see that even with manual assistance that the initial error interferes with the insertion until the errors become smaller than the maximum wedging error for that dimension. From Figure 5.20, we see the interval for the largest jamming parameters is during the initial insertion. This is likely the point where the insertion switches from one point contact to two point contact. From the response of these two failure types it appears that the impedance controller has the largest issue with wedging. Since the impedance controller can vary its compliance, jamming failure is minimized and less likely to occur. Wedging, on the other hand, is controlled by the accuracy of the system. As we have seen from the previous section, without a vision controller our impedance controller cannot reliably achieve

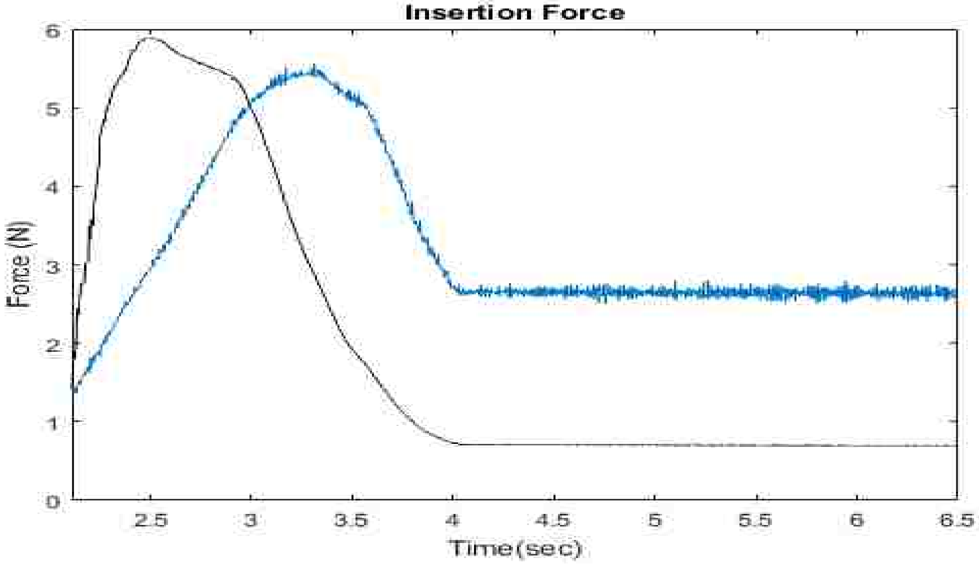

Figure 5.21: Insertion Force response during insertion. The black line is the modeled insertion force and blue line is the actual insertion force response.

this level of accuracy to prevent wedging. As we will see with the next insertions the positional errors will get larger and the prevention of wedging will get more difficult, as modeled in section 4.2.

Figure 5.21 shows the insertion force response along the modeled insertion force response. From Figure 5.21 we can see that the insertion force does indeed follow a similar profile to the insertion force but at some delay. We should also note that steady state force, where the model levels off, is smaller than the actual response. This may be due to the fact that the peg is still experiencing a frictional force resisting the peg or there are extra forces acting on the peg. We expect all of the insertion force response to behave this way. We should also note that in all three figures the response of the robot has slight chattering during motions, which was visible in our simulation results with an external environment.

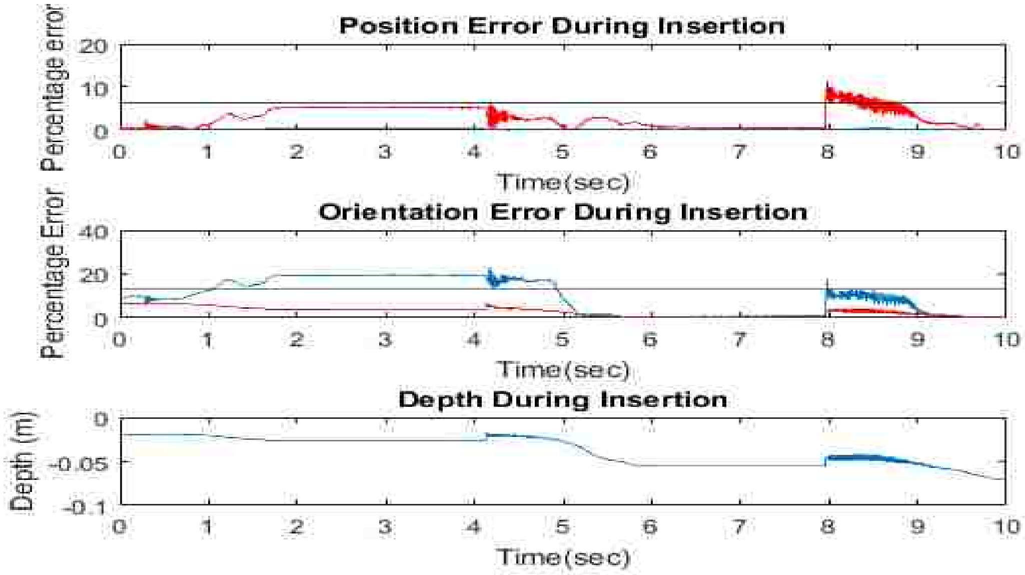

Figure 5.22: Square peg insertion error. The top graph shows position error, the middle graph shows orientation error, and last graph is the depth during insertion. The red lines correspond the $Y$ and $\theta_Y$ for the top and bottom graphs, respectively. The blue line corresponds to the $X$ and $\theta_X$ coordinate. The black horizontal lines are the maximum allowable wedging value.

### 5.5.2 Square Peg Insertion

Figure 5.22 is the impedance controller error during insertion for the square peg. Here we see a unique situation where the controller begins to insert but fails and stops. After the orientation error drops below the maximum modeled error the insertion starts again and the peg moves once again. As we will be seeing for all the insertion response for this impedance controller, the chattering during the motions is the largest during the initial motions likely due to the fact that this is when the peg experiences the largest resistance from the environment. Figure 5.23 shows the jamming parameter response of our controller. Again we see that the jamming is not an issue during the insertion. However, the jamming parameter has increased in response during this insertion, which does not follow the model from section 4.2

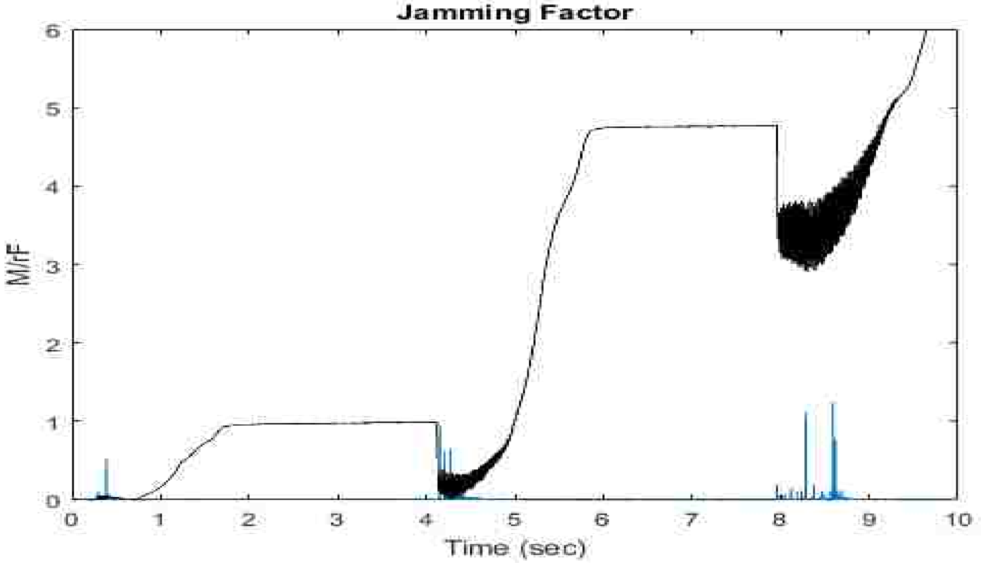

Figure 5.23: Jamming parameter response during square peg insertion. The black line is the jamming parameter varying with the depth and blue line is the jamming response during insertion.

where we would expect the jamming response to decrease. This is likely due to the fact that the large spikes are at the locations where the controller response is the noisiest.

As for the insertion force, Figure 5.24 shows the insertion force response along with the modeled response. This time the insertion force response appears to have less of a delay but this time it has an overshoot of the insertion force. Again the steady state force is larger for the actual response compared to the modeled response. During this insertion it is clearer that the chattering is the most distinct as the robot experience larger insertion forces and starts to stabilize as the insertion force decreases.

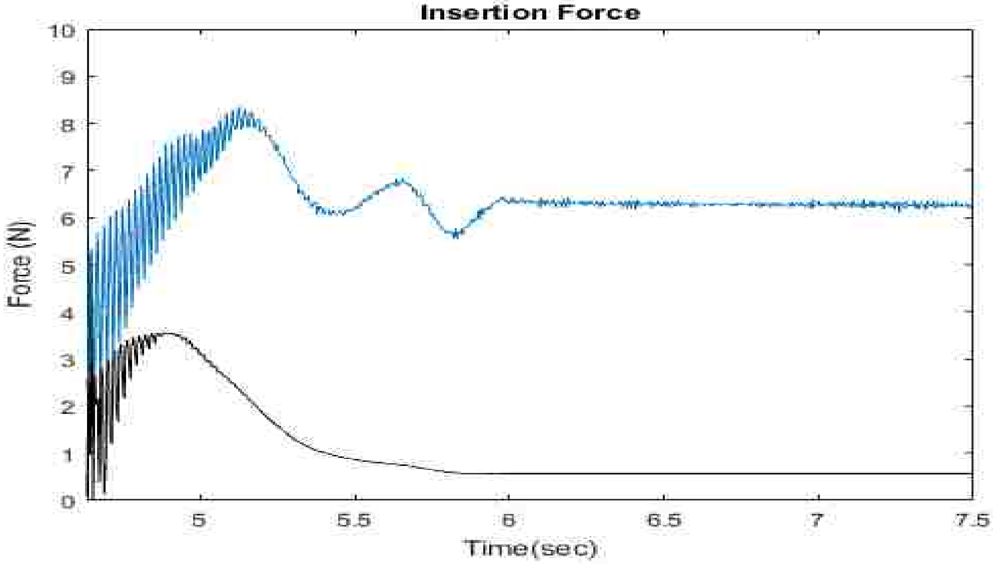

Figure 5.24: Insertion Force response during square peg insertion. The black line is the modeled insertion force and blue line is the actual insertion force response.

### 5.5.3 Cross Peg Insertion

Figure 5.25 shows the impedance controller response to the cross peg insertion error. From section 4.2 we expect the cross insertion to have the most difficulty during wedging and we see this in Figure 5.25. This time the position error is preventing the peg from insertion. It is worth noting that the clearance factor, $c = \frac{D-d}{D}$, is about two times larger for this insertion, $c = 0.0197$, compared to the circular peg, 0.0066. The jamming model and response are shown in Figure 5.26. Here we see no jamming response when compared to the maximum allowable jamming model. This is expected since preventing jamming for the cross insertion should be the easiest from the section 4.2 model.

As for the insertion response, Figure 5.27 shows the response for the cross insertion. This insertion response is interesting because the insertion doesn't begin until the third attempt, which can be seen in Figure 5.25. Here we see three different modeled forces response with the third finally finishing with a successful insertion.

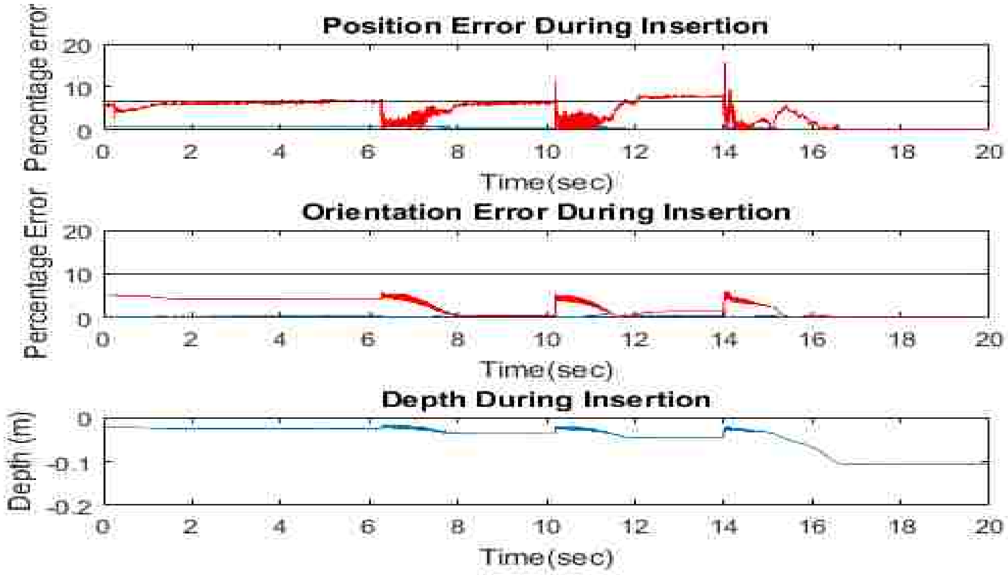

Figure 5.25: Cross peg insertion error. The top graph shows position error, the middle graph shows orientation error, and last graph is the depth during insertion. The red lines correspond the $Y$ and $\theta_Y$ for the top and bottom graphs, respectively. The blue line corresponds to the $X$ and $\theta_X$ coordinate. The black horizontal lines are the maximum allowable wedging value.

In the actual response we again see large overshoots in force and even larger chattering during the initial force responses. On the third attempt the peg is successfully inserted and the insertion force follows the model up until the end where it settles at a much larger value then the model. This force insertion model does follow the other models in that the actual insertion force is much larger and settles at larger values than modeled.

### 5.5.4 Cross Insertion against Gravity

Figure 5.28 shows the insertion errors for the cross peg insertion where gravity is acting the lateral direction of the peg. We can see how this additional external effect the insertion from Figure 5.28. After the second insertion attempt the insertion

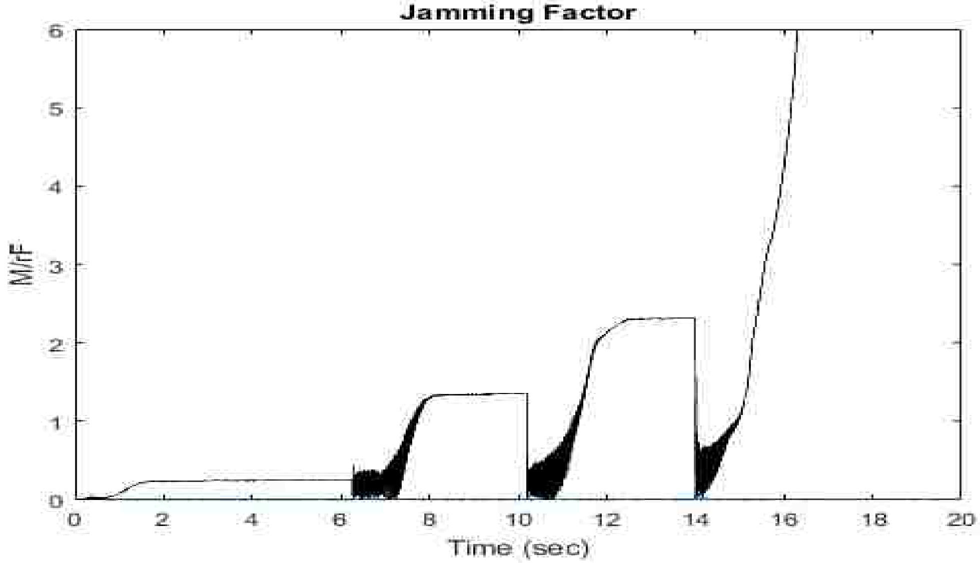

Figure 5.26: Jamming parameter response during cross peg insertion. The black line is the jamming parameter varying with the depth and blue line is the jamming response during insertion.

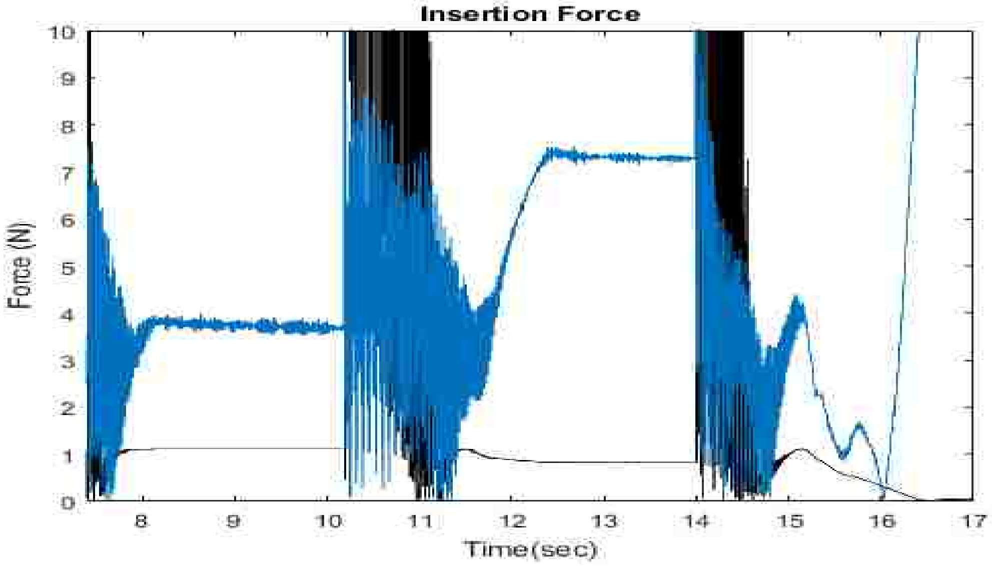

Figure 5.27: Insertion Force response during cross peg insertion. The black line is the modeled insertion force and blue line is the actual insertion force response.

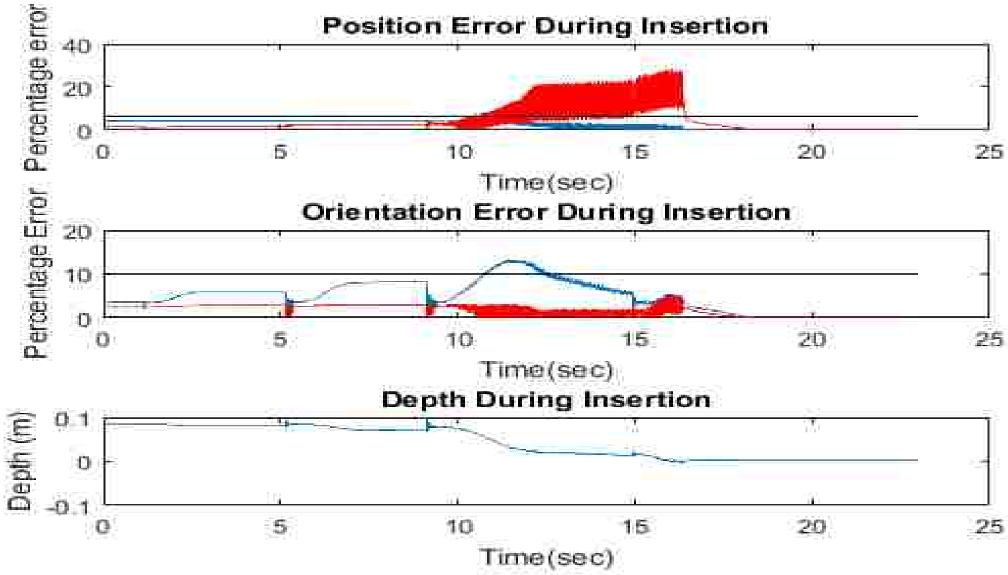

Figure 5.28: Cross peg insertion against gravity error. The top graph shows position error, the middle graph shows orientation error, and last graph is the depth during insertion. The red lines correspond the $Z$ and $\theta_Z$ for the top and bottom graphs, respectively. The blue line corresponds to the $X$ and $\theta_X$ coordinate. The black horizontal lines are the maximum allowable wedging value.

begins and starts to wedge, likely due to gravity pulling down on the peg. As we have seen from the simulation results, an increase in the stiffness of the environment causes our controller to become unstable. Eventual the force becomes large enough to complete the insertion. Figure 5.29 shows the jamming parameter response during this insertion. As suspected the jamming parameter grows significantly when the controller starts to become unstable. Even though jamming is not an issue during this insertion it is also affected by insertions against gravity.

In Figure 5.30 we will only be looking at the force during the insertion. We again see a delayed insertion along with a very noisy response. We also see a very significant overshoot in the response. All of these changes are due to the fact that the insertion model does not account for gravity acting on the peg. From this we can see that the majority of the insertion is to overcome the additional frictional force

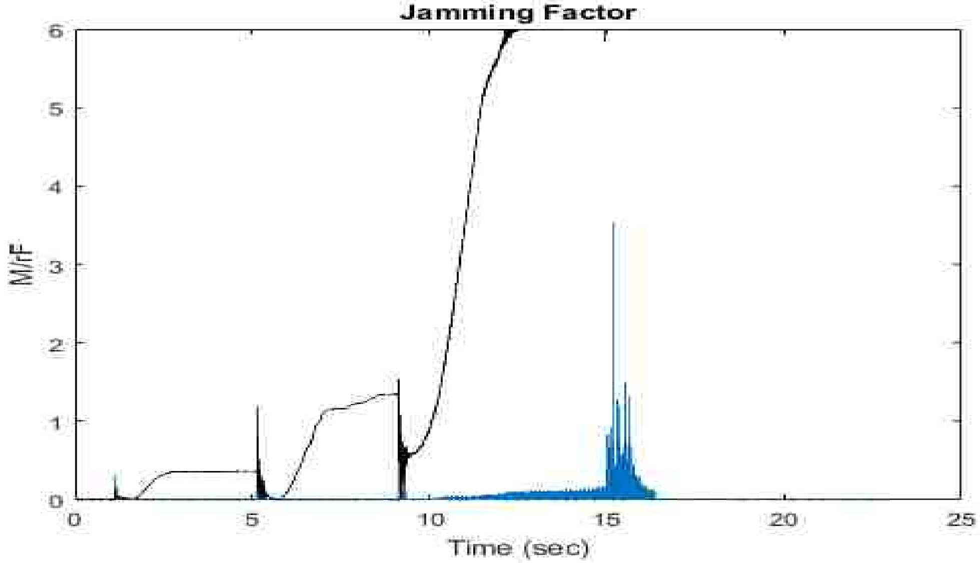

Figure 5.29: Jamming parameter response during cross peg insertion against gravity. The black line is the jamming parameter varying with the depth and blue line is the jamming response during insertion.

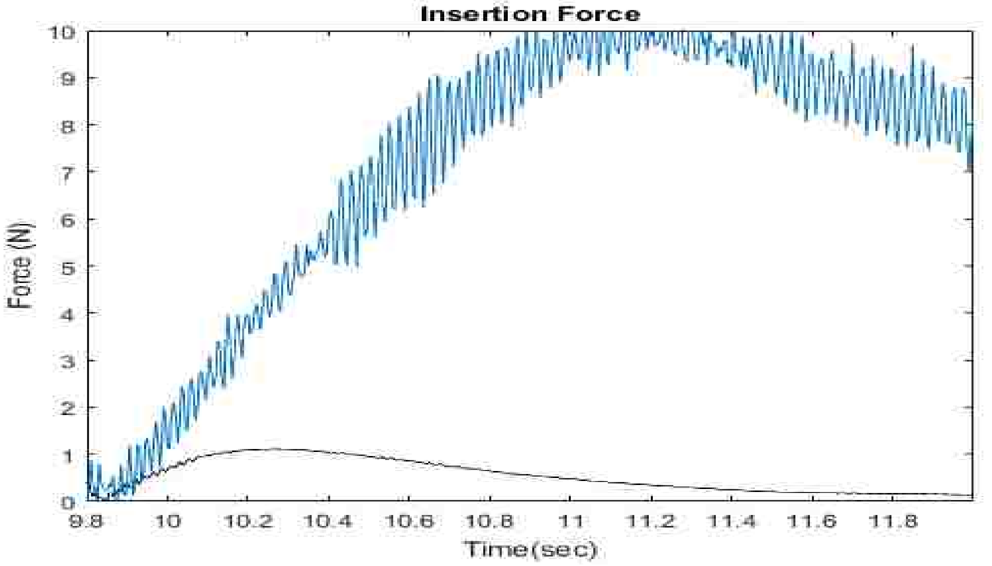

Figure 5.30: Insertion Force response during cross peg against gravity insertion. The black line is the modeled insertion force and blue line is the actual insertion force response.

from gravity pulling down on the peg.

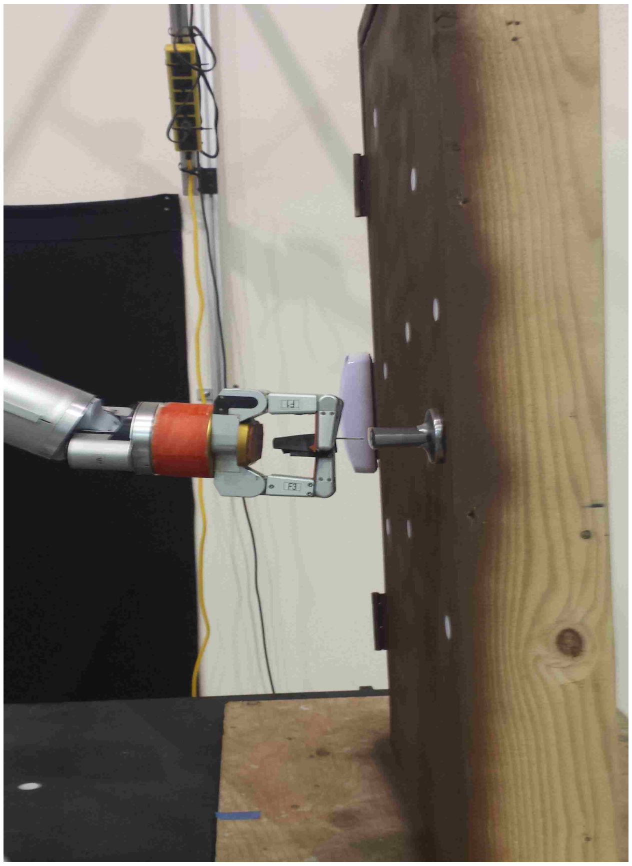

Figure 5.31: WAM holding key to be inserted into keyhole

### 5.5.5 Key Insertion

For the key insertion test we had to use a different setup. Figure 5.31 shows the WAM holding a key to be inserted.

Looking at the percentage errors we see fewer issues with the key insertion in the orientation, shown in Figure 5.32. Typically the orientation causes the most error but this is not the case. Since the key is lighter and shorter, the gravitational force from holding the key up against gravity is not as significant as compared to the cross insertion against gravity. The biggest source of error for this insertion comes

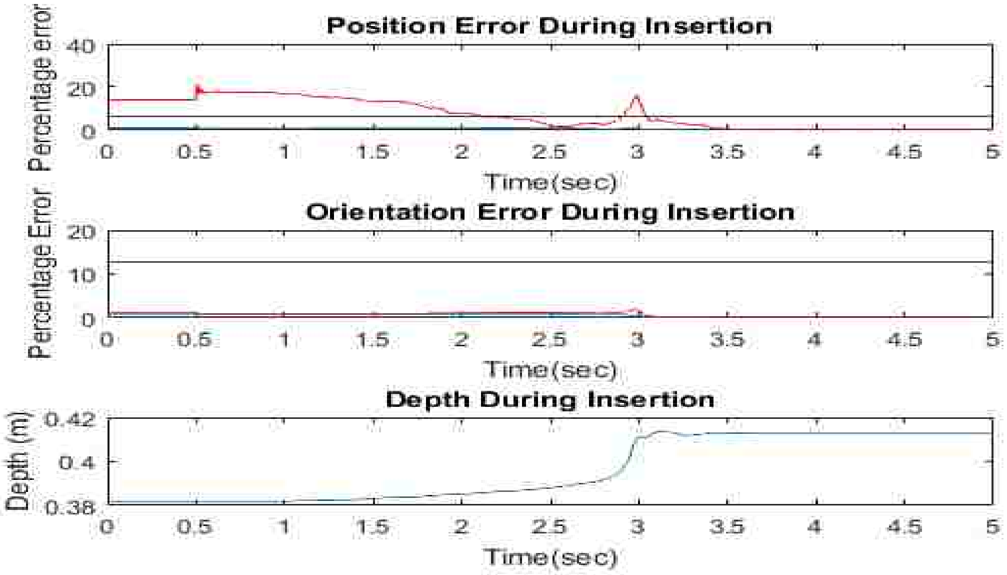

Figure 5.32: Key Insertion. The top graph shows position error, the middle graph shows orientation error, and last graph is the depth during insertion. The red lines correspond the $Y$ and $\theta_Y$ for the top and bottom graphs, respectively. The blue line corresponds to the $Z$ and $\theta_Z$ coordinate. The black horizontal lines are the maximum allowable wedging value.

from the horizontal alignment of the key, the $Y$-axis. As seen in the key insertion model, the more complicated geometry allows for more potential wedging failures, as jamming becomes less likely. We can see the point the error in the $Y$-axis spikes up the error in the orientation drops and the insertion depth increases rapidly. This is the keyhole geometry assisting the compliant controller with the insertion.

Figure 5.33 shows the jamming response for the key insertion. As we expected from all the other insertions, the jamming parameter only spikes during the initial motion before the insertion begins. Afterwardsthere is nearly no response. Again this is due to the very compliant nature of the impedance controller. As for the insertion force we get a very different response than expected. Figure 5.34 shows the insertion response for the key insertion. In this insertion force response we not only get a large overshoot when compared to the model but we also get a significant

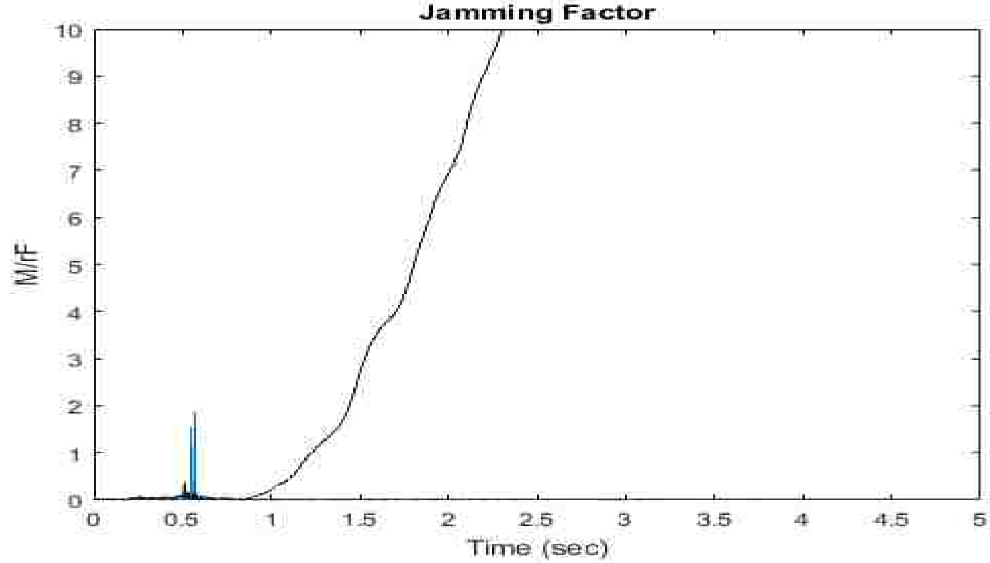

Figure 5.33: Jamming parameter response during key insertion. The black line is the jamming parameter varying with the depth and blue line is the jamming response during insertion.

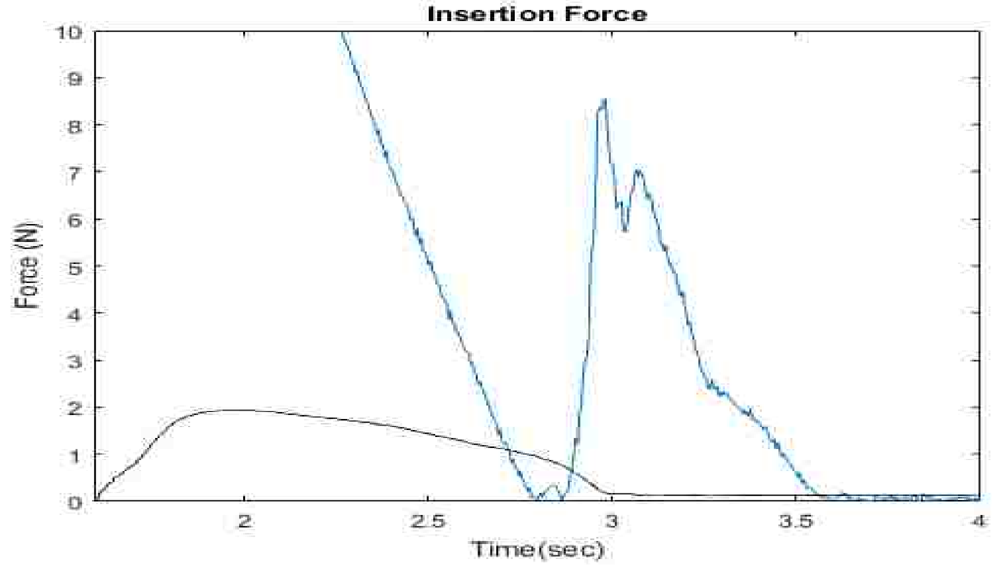

Figure 5.34: Insertion Force response during key insertion. The black line is the modeled insertion force and blue line is the actual insertion force response.

delay in the with respect to the model. This delayed insertion force response may be from the complicated keyhole geometry aligning the key before insertion begins. This would also account for the additional insertion force required for the insertion.

## 5.6 Summary

In this chapter we introduced the standard Hogan impedance controller, also know as the position based impedance controller. We modeled and simulated this controller's response when interacting with the environment. We then introduced a vision system to improve the accuracy of the controller. Finally we used the position impedance controller to successfully insert objects into multiple geometries. We will be this position based impedance controller as the baseline for comparison when the velocity based impedance controllers of Chapter 6 and 7 are introduced.

Through these various insertions we have seen the usefulness of the impedance compliance controller. With the compliance from an impedance controller jamming is avoided by controlling the compliance parameters. As for the wedging, so long as the initial insertion errors are minimized (which can be done through a vision system) the compliance of the controller can allow the inserted object to align itself for a successful insertion. We did see instances when the stiffness of the environment was too large and the controller nearly became unstable. The insertion forces for all the insertions tended to be larger than modeled. This is expected since the insertion model assumes the force interactions to be quasi-static when they are actually more dynamic.

# Chapter 6

# Velocity Filtered Impedance Controller

In this chapter we build off the previously described impedance controller and introduce the velocity filtered impedance controller. We will then model the controller and simulate the controller, comparing the stability and response with the position based impedance controller. Then the two controllers will be compared based on the same controller responses, single motion, external force, and visual control. Finally, the two controller responses will be compared for all object insertions.

## 6.1 Velocity Filter Impedance Model and Simulation

The impedance controller introduced earlier in chapter 5 is a straightforward method that does not use any state feedback. For the straightforward case the error terms can be made small by using a very stiff position controller. This has been shown to improve the accuracy of the controller [48], but as we have shown increasing the stiffness of the controller will also cause the controller to go unstable.

For the velocity impedance control method we will be using an impedance filter of $\frac{1}{Bs}$ and the impedance feedback is $Ms^2 + K$ [41]. Figure 6.1 shows the control model with the included impedance filter and impedance feedback. As seen in Figure 6.1 we are running our controller on a single joint model. We will use the same modeling parameters for our simulation as the position based impedance controller. We will also be looking at the response with and without an external environment. However, for this model we will be changing the gain $k_p = K$, where $K$ is the stiffness of the impedance controller.

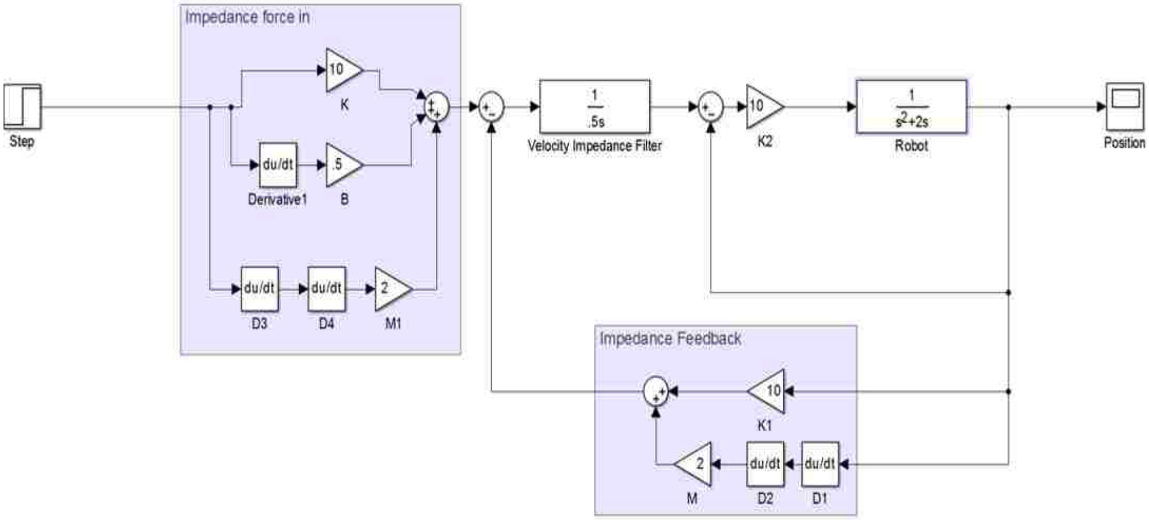

Figure 6.1: The simulation model for the position impedance method. Note there is a feedback function with the velocity impedance acting as a filter to the impedance force in. In this model the environment is not acting on the controller.

Using this simulation models we can find the Laplace transform for the case of no external environment and with an external environment.

$$\frac{x_{out}}{x_{in}} = \frac{K(Ms^2 + Bs + K)}{I_a Bs^3 + (KM + BB_v)s^2 + KBs + K^2)} \tag{6.1}$$

for the response without the environment acting on the controller. The response

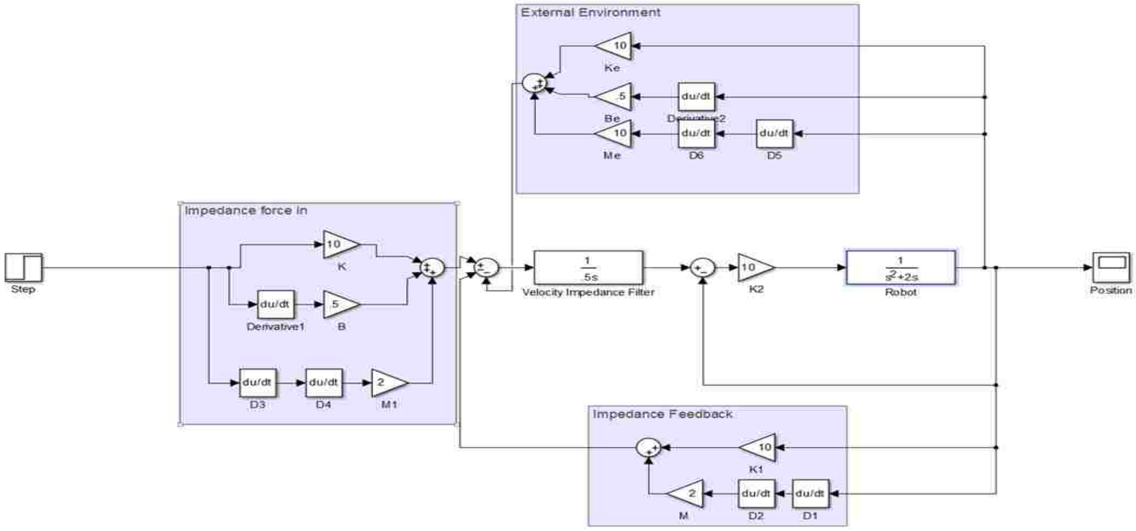

Figure 6.2: The simulation model for the velocity impedance method. Note there is a feedback function with the velocity impedance acting as a filter to the impedance force in. In this model the environment is acting on the controller.

with the environment acting on the controller is the following.

$$\frac{x_{out}}{x_{in}} = \frac{K(Ms^2 + Bs + K)}{I_aBs^3 + (K(M + M_e) + BB_v)s^2 + K(B + B_e)s + K(K + K_e))} \tag{6.2}$$

From (6.1) and (6.2), we have a third order system for both controllers. Again we are treating the environment as a mass-spring-damper system. Using Routh-Hurwitz stability criterion for third order systems, we get stability for (6.1) when $M + \frac{BB_v}{K} > I_a$ and stability for (6.2) when $[(M+M_e)+\frac{BB_v}{K}](B+B_e) > I_aB(K+K_e)$. Now let us compare these stability criterion with the benchmark for the position based impedance controller.

For the velocity based impedance controller with no external environment we saw that the position based method was always stable and the velocity impedance method requires $I_a < M + \frac{BB_v}{K}$. This means that at higher stiffness values the mass of the robot needs to be larger than the inertia of the joint. The stiffness of the controller also affects the location of the 2 zeros of the system and the gain.

For the velocity based controller with an external environment we saw that the position based method had two stability requirements: $\frac{M_e}{M} + \frac{B^2 B_v}{K} > \frac{B_e}{B}$ and when $B[K(M + M_e) + BB_v](B + B_e) > MK(B + B_e)^2 + B^2 I_a(K + K_e)$. For the velocity impedance controller the only requirement is $[(M + M_e) + \frac{BB_v}{K}](B + B_e) > I_a B(K + K_e)$. For the position based impedance controller there is an additional stability requirement for the ratio of the mass of the environment to be larger than the ratio of the damping. This does not exist for the velocity impedance controller. This gives us the freedom of also using the damping of the impedance controller as a compliance parameter. In this type of mass-spring-damper model, the mass of the environment is the mass of what is acting against the robot. For example, if the robot was to push a block along a table the mass is only of the block. However, if the robot were to push the block into the table the mass would include both of the objects.

Both controllers, become unstable at high stiffness values for the robot or the environment. The major difference is at which point that threshold is reached for each controller. To find this threshold we will define the velocity impedance stiffness at the point of marginal stability, $(K + K_e)_v = \frac{[(M+M_e)+\frac{BB_v}{K}](B+B_e)}{I_a B}$. After doing this we get the following relationship between the stiffness threshold between the velocity impedance and the position based method.

$$\frac{K}{I_a B}(K + K_e)_v - \frac{MK(B + B_e)^2}{B} > (K + K_e)_s \tag{6.3}$$

where $(K + K_e)_v$ is the stiffness for the velocity impedance and $(K + K_e)_s$ is the stiffness for the position impedance. We should note that the improvement in stability does not depend on the mass of the environment. From (6.3) we can see that the stability threshold for the velocity impedance will be larger than the position based method.

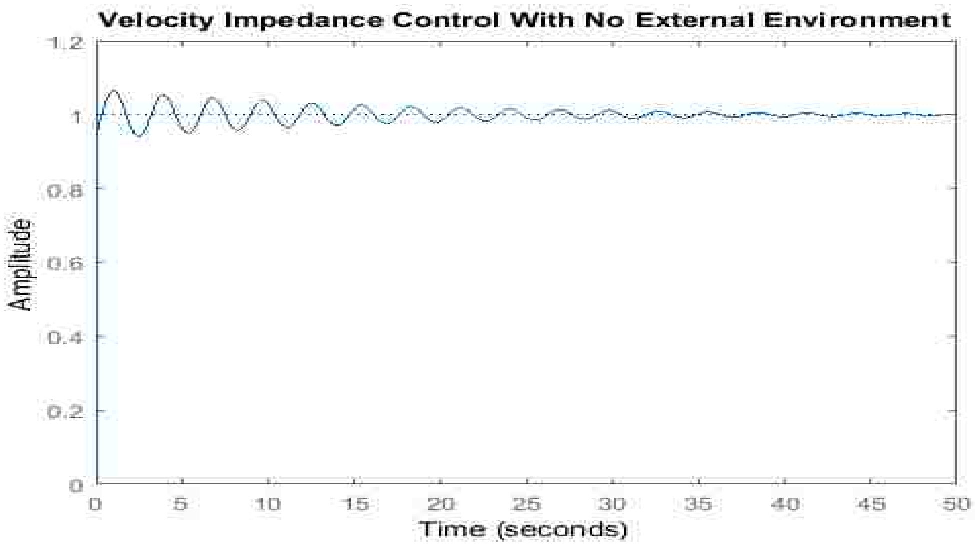

Figure 6.3: The velocity impedance controller response without environment.

### 6.1.1 Simulation Results

Now that we have seen the difference in stability for both methods let us look at the difference in simulated response between both controllers. To do this we will be using the same modeling parameters as the position impedance controller simulation model from section 5.3. These parameters are $M = 2, M_e = 10, B = 0.5, B_e = 0.5, K = 10, K_e = 10, I_a = 1$, and $B_v = 2$.

First let us look at the response of the velocity impedance controller to the ideal case of no environment acting on the controller. Figure 6.3 shows the response from the velocity impedance controller from the ideal case. From this image we see that the controller has a very fast rise time but there is a long settling time due to the ringing from the response.

To compare this ideal controller response with the position based impedance controller response we will look at Figure 6.4. In this figure we see that the ideal case has for the position based impedance controller has a slower rise time but a

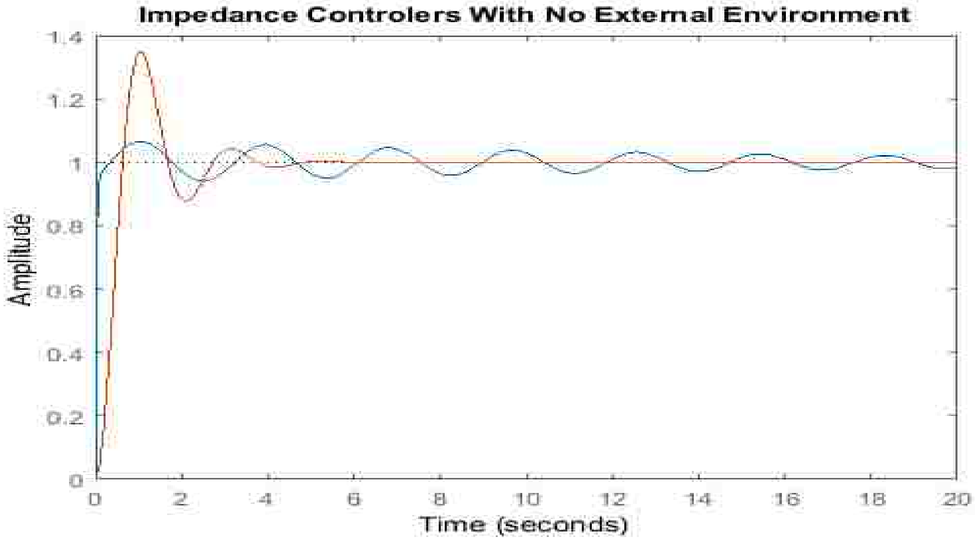

Figure 6.4: Both controllers response without environment. The blue line is the velocity impedance controller and the red line is the position based impedance controller

significantly faster settling time than the velocity impedance controller. For motions made with no environment acting on the robot we would expect the position based impedance controller to be the better controller with the faster settling time.

Now we will look at how the velocity impedance controller responds with an external environment acting on the controller, in Figure 6.5. As we expected the response of the system has a significant amount of ringing but it also has a stable response that settles quickly. To see how this response compares to the position impedance method we will look to Figure 6.6.

In this response we see that the position impedance method has some additional frequencies in its response when compared to the velocity controller's response. We also see that over time the velocity impedance controller starts to respond slower than the position method. From these simulation results we can expect the position impedance controller to have the faster response compared to the velocity impedance controller. However, we can expect more stable responses from the ve-

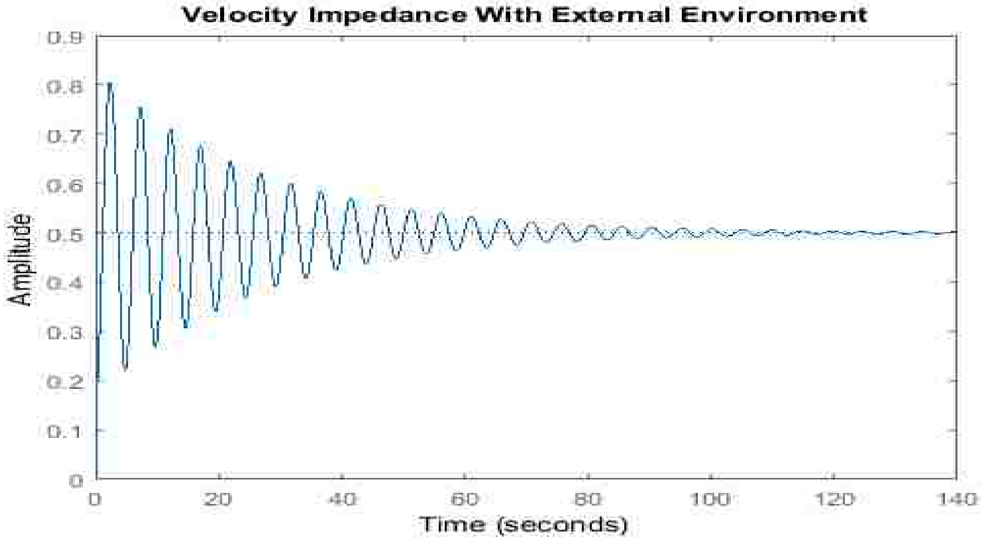

Figure 6.5: The velocity impedance controller response with environment.

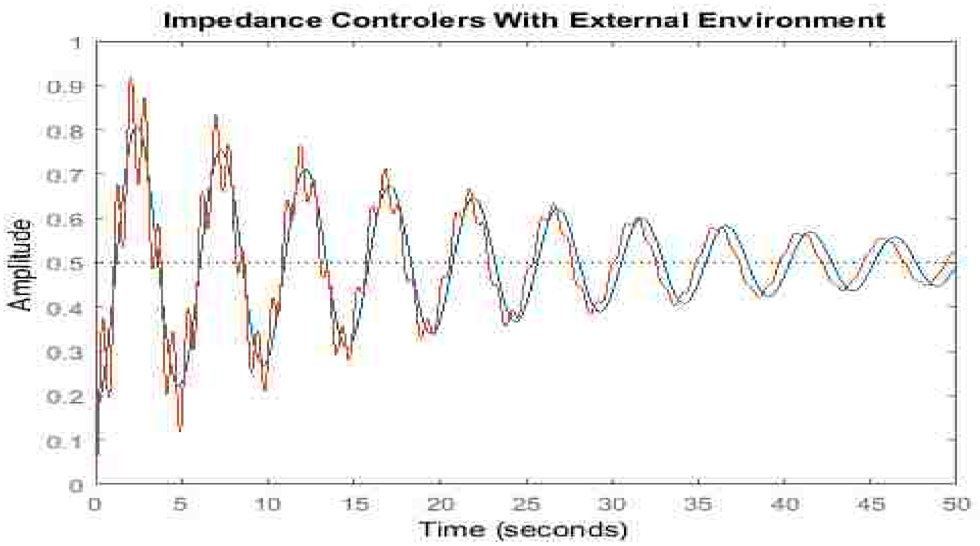

Figure 6.6: The impedance controllers response with environment. The blue line is the velocity impedance controller and the red line is the position based impedance controller

locity impedance controller when interacting with external forces.

Now let us look at the response of the velocity impedance controller when we

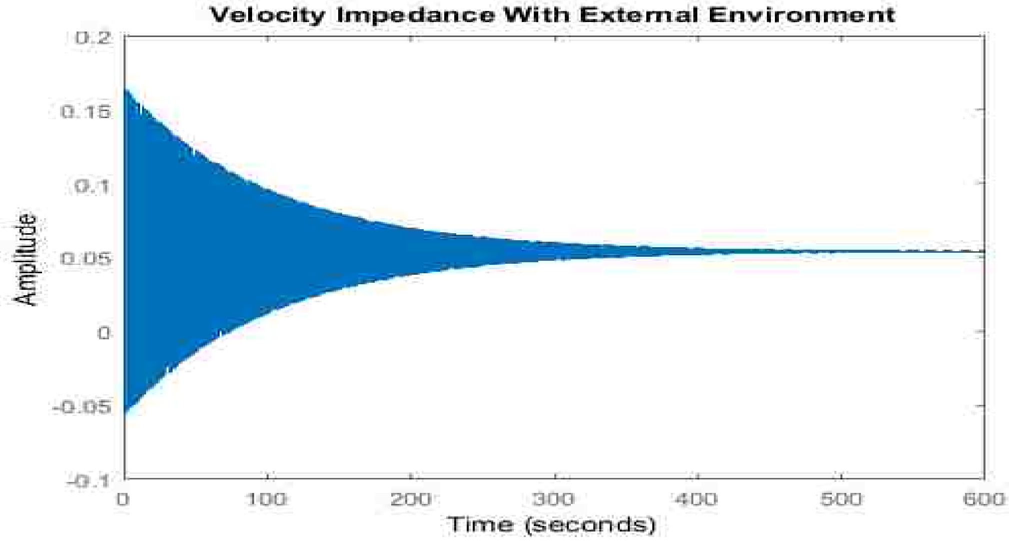

Figure 6.7: The velocity impedance controller response from a high stiffness environment.

increase the stiffness of the environment to the same high stiffness as done at the end of section 5.3. Here the environment stiffness is increased to $K_e = 100$. Figure 6.7 shows the velocity impedance controller response to the increased environment stiffness. As we have determined from our stability analysis the controller is still stable but we can see a significant amount of ringing in the controller.

Now let us compare the stable response from the velocity impedance controller to the unstable response of the position impedance controller, show in Figure 6.8. In this response we see that position impedance controller becomes unstable immediately and that the velocity impedance controller will maintain stability. From figure 6.7 we know that the velocity impedance method will continue to ring until it converges after a very long time.

As we have seen from these simulation results we can expect the position based and the velocity impedance controller to have similar accuracy with respect to position error. We do expect that the position impedance controller will reach its goal

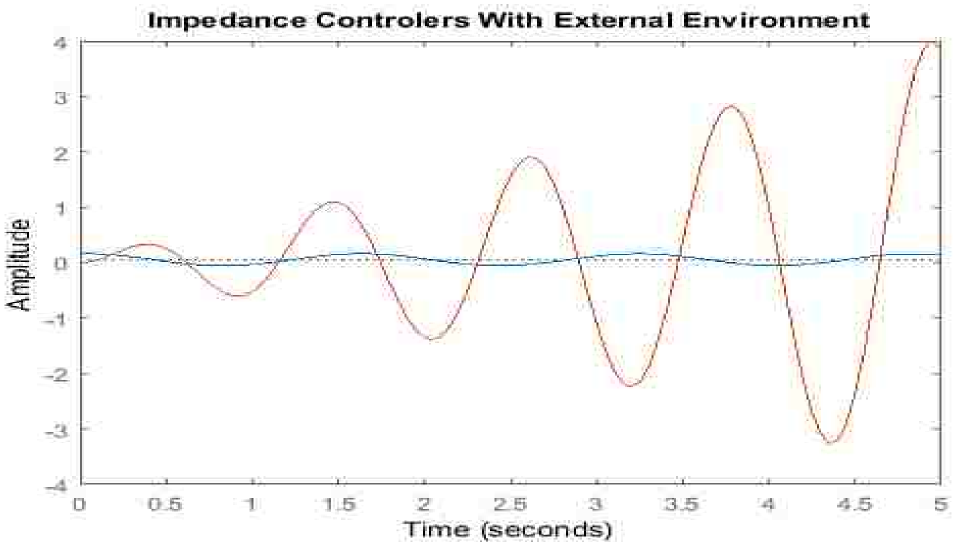

Figure 6.8: Both controllers response to a high stiffness environment. The blue line is the velocity impedance controller and the red line is the position based impedance controller, which is clearly unstable.

faster than the velocity impedance controller in both the ideal case and in the case with a low stiffness environment. When interacting with high stiffness environments, we expect the velocity impedance controller to maintain stability and to respond similarly. As for the position impedance controller we have to worry about maintaining stability in many of these environments, as we have seen for the object insertions for this impedance controller.

## 6.2 Controller Response

In this section we will be looking at the response from the velocity impedance controller. First we will look at the response of the controller to a specified position. Next we will look at the controller's response when the robot collides into an object. Finally we will be looking at the improvement in the controllers response with a vision system added into the controller. For each experiment we will also be comparing the responses from the velocity impedance controller to the responses from the position based method.

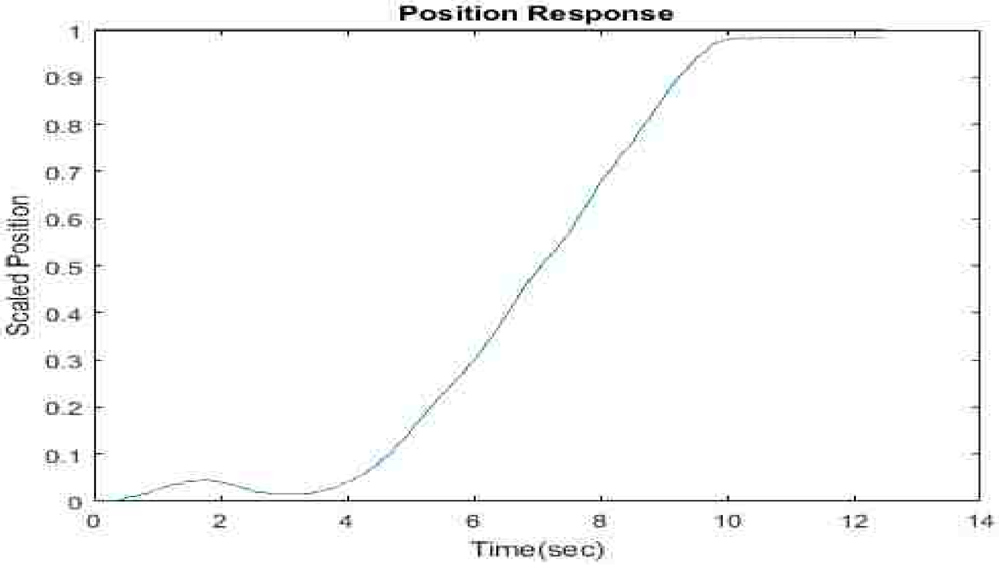

Figure 6.9: The velocity impedance controller pose response. The black line is the goal and the blue line is the response.

### 6.2.1 Non-Contact Motion

For this experiment we sent both impedance controllers to the same goal position. We will scale the motion based off the goal position due to the fact that both controllers will not be starting in the same exact position. Figure 6.9 shows the position response of the velocity impedance controller.

The positional stiffness values for the controller are: $K_x = K_y = K_z = 1000$, and the pose stiffness values are: $K_{\theta x} = K_{\theta y} = K_{\theta z} = 1$. The damping values for the controller are: $B_x = 15, B_y = 10, B_z = 5$ and $B_{\theta x} = B_{\theta y} = B_{\theta z} = 0.1$. These are the exact same compliance parameters used with the position based impedance controller. From Figure 6.10 we can see that the position response is very accurate and close to the goal position with some steady state error. As for Figure 6.11, we

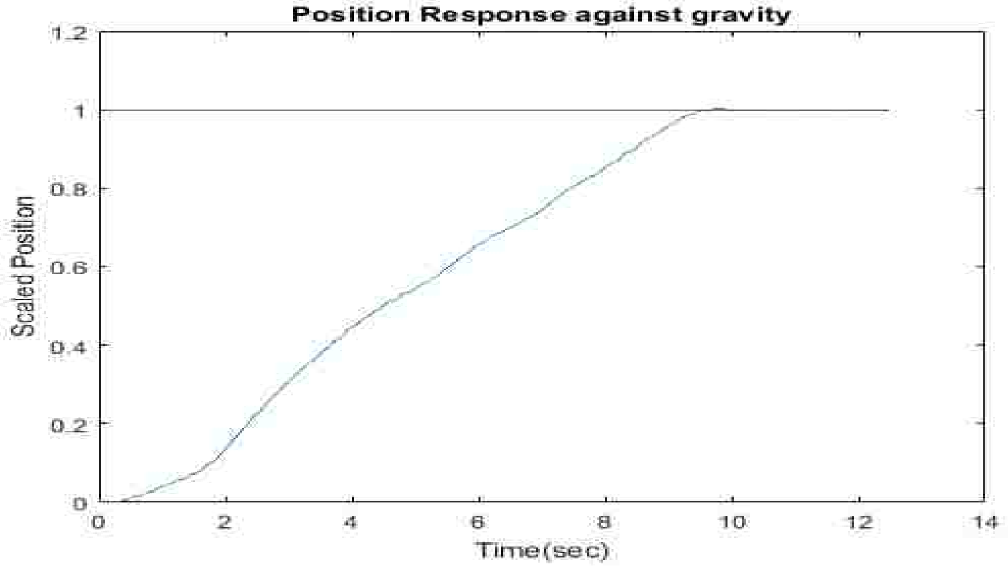

Figure 6.10: The velocity impedance controller response of the position in the direction of gravity. The black line is the goal and the blue line is the response.

see that there is some significant steady state error in the pose.

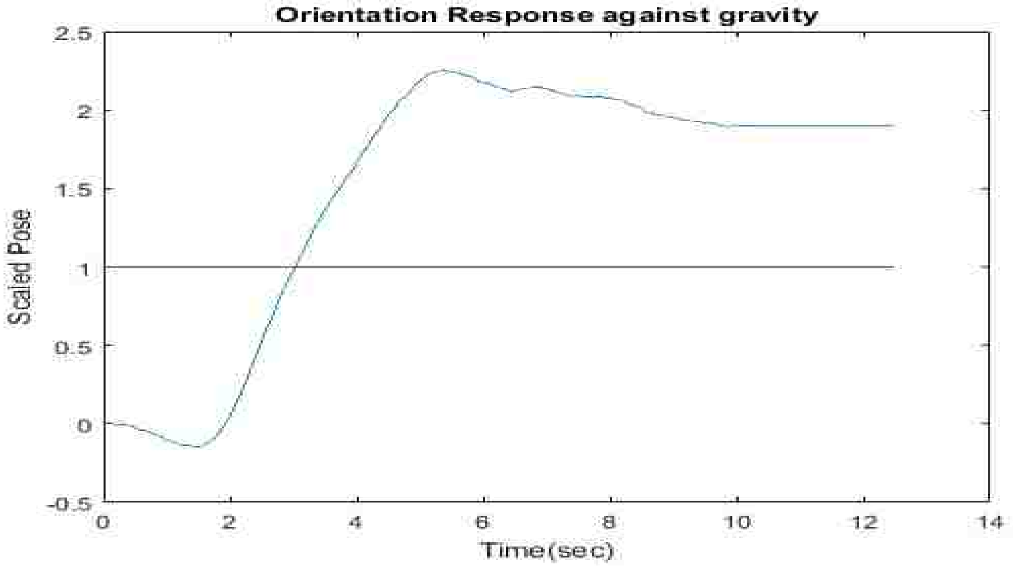

Figure 6.11: The velocity impedance controller pose acting against gravity. The black line is the goal and the blue line is the response.

To compare the velocity impedance controller response with the position based impedance controller we will look at Figures 6.12 and 6.13 for the position and the pose response, respectively. Comparing the two impedance controllers we see that the position impedance controller has the faster and more accurate response. This is to be expected when comparing the simulation responses. In the case of Figure 6.12 we see that the position errors for the two controllers are relatively similar; whereas, Figure 6.13 shows a significant difference in the accuracy of the two controllers.

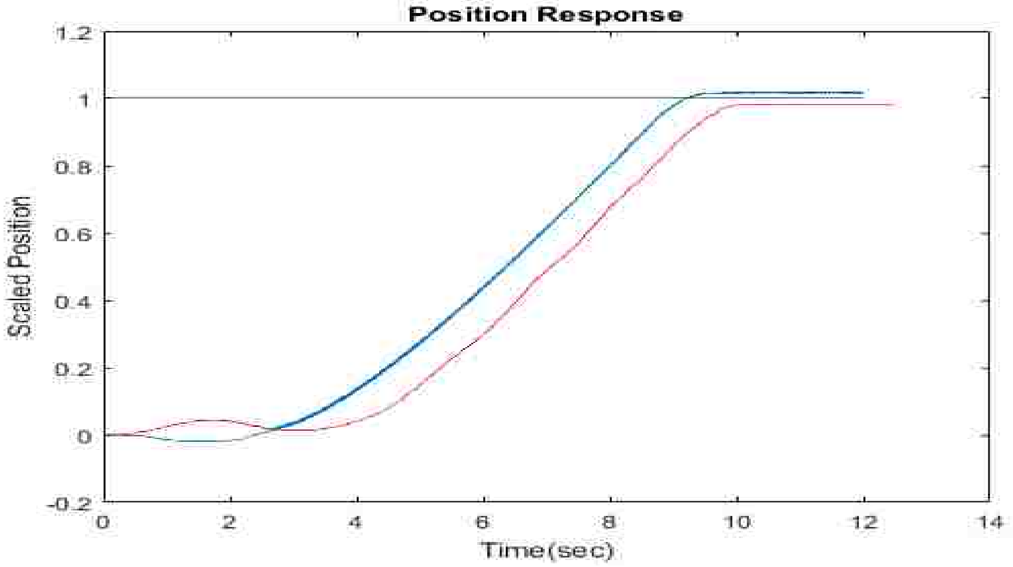

Figure 6.12: Comparison between both impedance controllers. The blue line is the position based impedance controller and the red line is the velocity impedance controller. Again the black line is the goal.

As shown in the simulation model, the velocity impedance controller has a larger range of stability with respect to the controller's stiffness. Let us look at the improvement of the accuracy of the robot if we increase the stiffness values for the pose. Figures 6.14 and 6.15 show the response of the velocity impedance controller when the pose stiffness is increased by a factor of five ($K_{\theta x} = K_{\theta y} = K_{\theta z} = 5$).

For Figure 6.14 we see that the accuracy of the position does increase a slight amount. Figure 6.15 shows a substantial amount of improvement in the accuracy in the pose of the robot. By increasing the pose stiffness by a factor of five we were

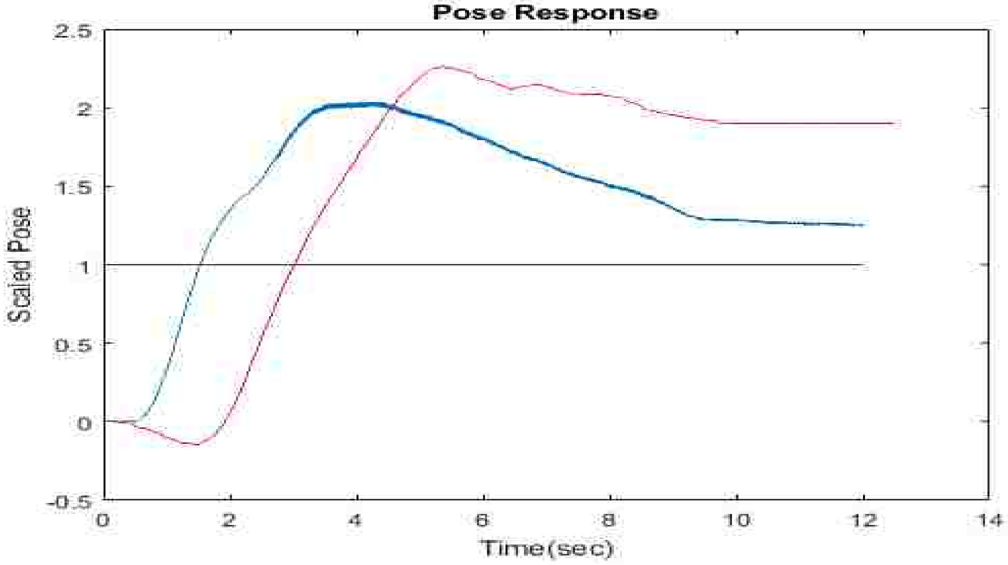

Figure 6.13: Comparison between both impedance controllers. The blue line is the position based impedance controller and the red line is the velocity impedance controller. Again the black line is the goal.

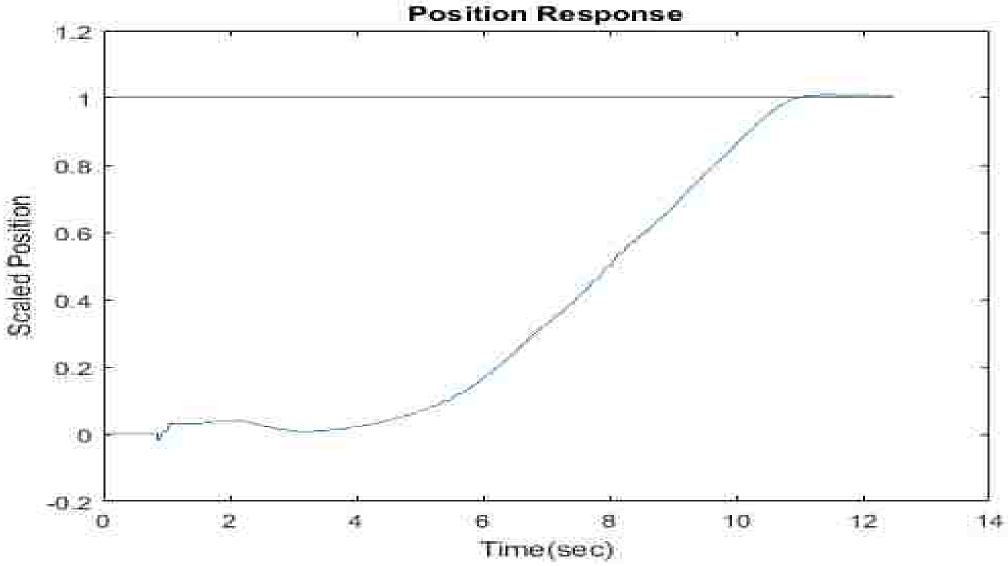

Figure 6.14: Velocity impedance position response at higher stiffness values. $K_{\theta x} = K_{\theta y} = K_{\theta z} = 5$

able to decrease the error in the pose by 90%. We cannot compare the position based impedance controller response at these same compliance parameters since the controller becomes unstable at these values.

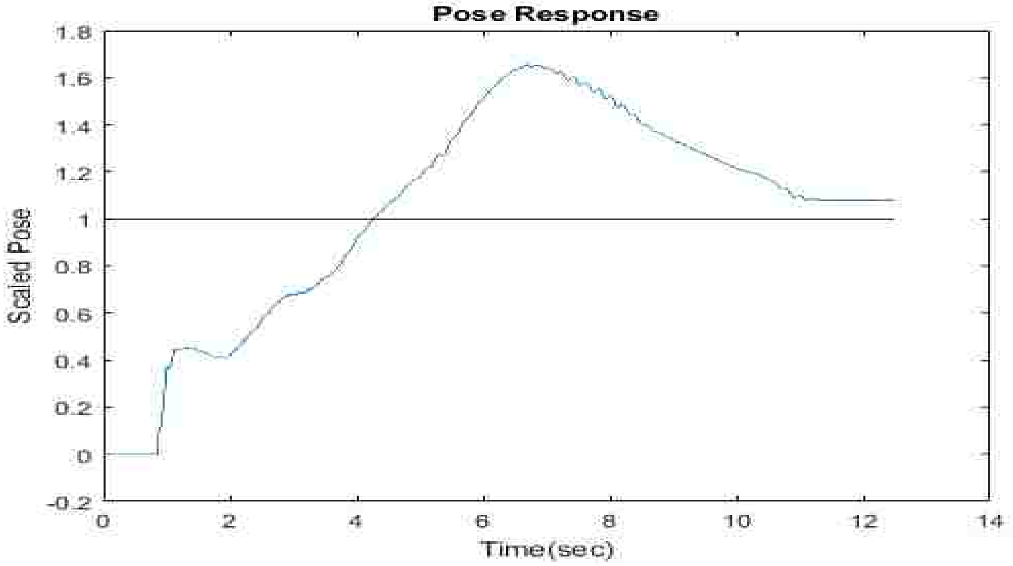

Figure 6.15: Velocity impedance position response at higher stiffness values. $K_{\theta x} = K_{\theta y} = K_{\theta z} = 5$

### 6.2.2 External Force Response

Next we are going to look at the force response of the velocity impedance controller when the robot collides with an object in its path.

As for the velocity impedance response, in Figure 6.16, we can see that the initial collision, at $t = 0$, causes the force to dip down then continue linearly. This mostly linear response is the same as the high stiffness response from the position impedance controller, which makes sense since they both have the same stiffness values. However, we can see that this response remains stable past $20N$ where the position controller started to go unstable. We can see this difference in Figure 6.17. Again from the simulation results we expect both controllers to maintain some sort

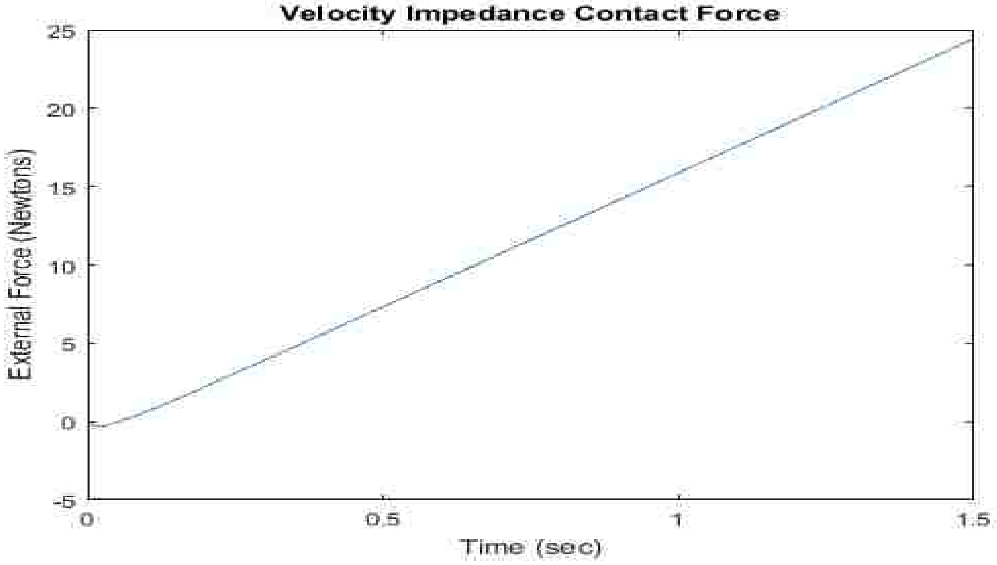

Figure 6.16: The velocity impedance controller contact force. The stiffness were set at $K_x = K_y = K_z = 1000, K_{\theta x} = K_{\theta y} = K_{\theta z} = 1.0$

of similar response. The main difference being we expect the velocity impedance controller to maintain stability.

Figure 6.18 shows the force response for higher stiffness values, same stiffness values used in Figures 6.14 and 6.15.

Figure 6.18 compares the two velocity impedance controller responses. Again we increase the pose stiffness by a factor of 5 and we can see the slight increase in the force response. We should also note that both controllers have the small initial dip once contact is made. This is likely an impulse response from the high stiffness in the collision. Both responses remain stable for the high stiffness collision whereas the position based impedance controller became unstable.

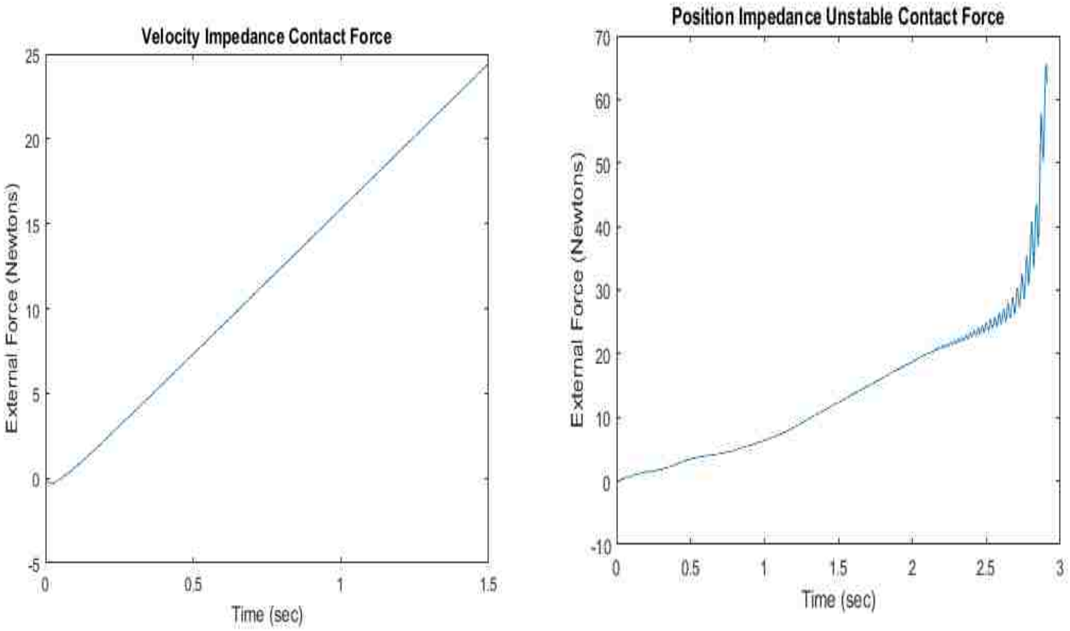

(a) Velocity impedance force response

(b) Position based impedance controller force response

Figure 6.17: Comparison of force response for same stiffness values.

### 6.2.3 Visual Control Response

Next, let us look at a visual velocity impedance controller response using the same stiffness as the impedance controller in chapter 5. In Figure 6.19 we see that the position accuracy improves for a bit and goes back to its original position. As for the pose accuracy we see the error decrease slowly but substantially. In Figure 6.20 we compare both impedance controllers. We can see that the position based impedance controller initially has more pose error but has a faster response to this error. However, we can see the velocity controller has less error for both the position and the pose overall. It is also worth noting that the velocity controller has a faster response at high stiffness values, a consequence of its large range of stability.

Let us look at the pose response for both controllers, as shown in Figure 6.20. Here we can see the larger initial error for the position impedance controller but it

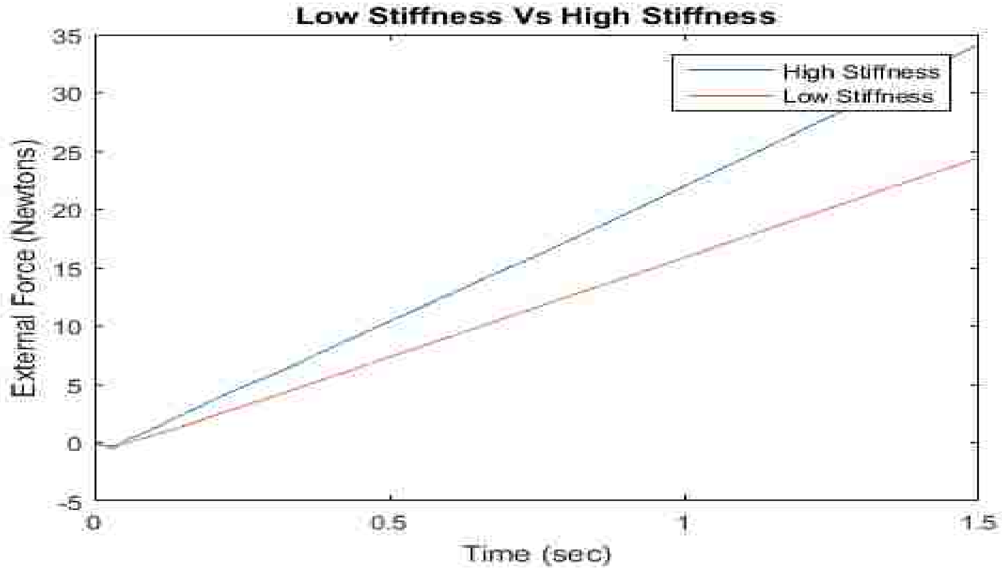

Figure 6.18: The velocity impedance controller with high and lower stiffness values. The high stiffness are set at $K_x = K_y = K_z = 1000, K_{\theta x} = K_{\theta y} = K_{\theta z} = 1.0$ (blue) and $K_x = K_y = K_z = 1000, K_{\theta x} = K_{\theta y} = K_{\theta z} = 5.0$ (red)

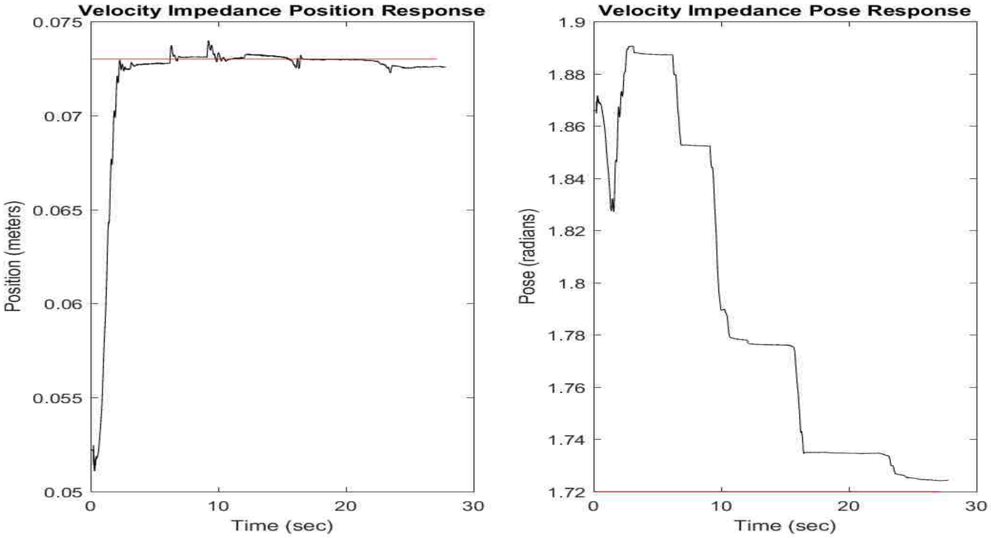

Figure 6.19: Visual velocity impedance controller response. Stiffness values were set at $K_x = K_y = K_z = 1000, K_{\theta x} = K_{\theta y} = K_{\theta z} = 1.0$.

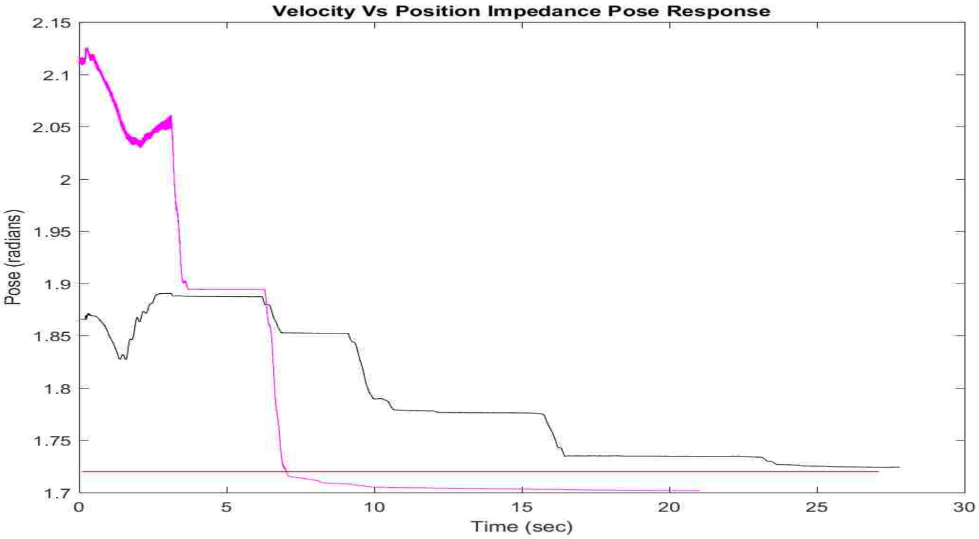

Figure 6.20: Comparison of the velocity and position controller pose response. The position controller response is in magenta and the velocity controller response is in black.

has the faster response to the goal. For the velocity controller we see a much slower but accurate response when compared to the position controller response. In Figure 6.13 we saw both controllers with low stiffness values having large errors but now with a vision controller in place it is possible to substantially improve the pose of the robot. As seen in the insertion results from the position based impedance controller, the increase in pose accuracy will increase the chances of the objects insertion. If the pose has too much error then the insertion will fail. As we have seen for both controllers, the inclusion of a vision controller increases the accuracy in the response of the robot without having to sacrifice its stability.

Again we saw in the simulation results that the position impedance controller will respond faster than the velocity impedance controller. Even with vision control we see that both controllers' accuracy is similar and they behave as simulated.

## 6.3 Insertions Testing

In this section we will be doing all of the same insertions from chapter 5 at the same stiffness values. In for each insertion we will be directly comparing the insertion results from the velocity impedance controller with the position based impedance controller.

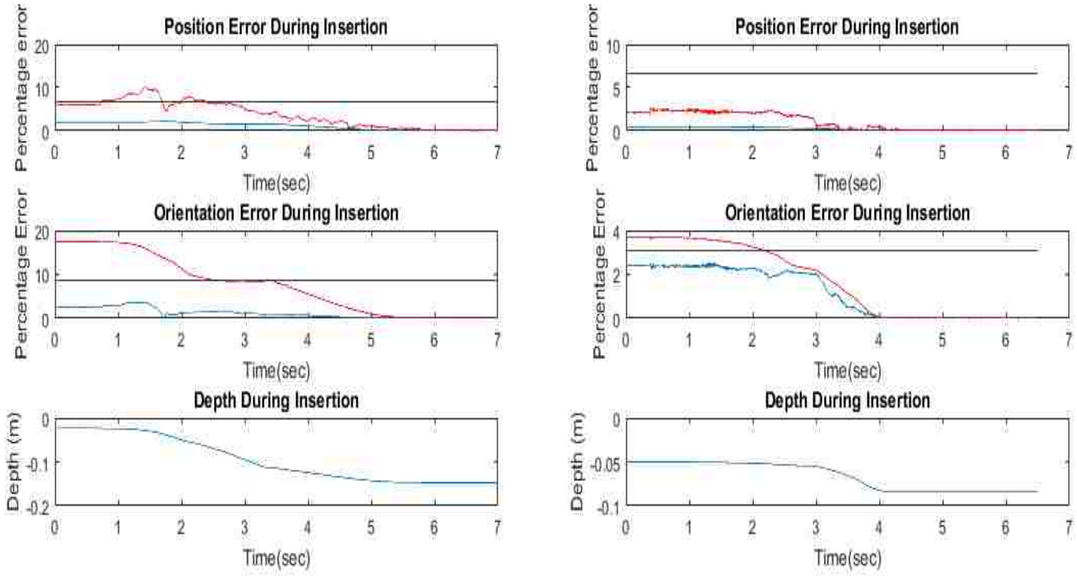

(a) Velocity Impedance Controller (b) Position based Impedance Controller

Figure 6.21: Circle peg insertion errors. The top graph shows position error, the middle graph shows orientation error, and last graph is the depth during insertion. The red lines correspond the $Y$ and $\theta_Y$ for the top and bottom graphs, respectively. The blue line corresponds to the $X$ and $\theta_X$ coordinate. The black horizontal lines are the maximum allowable wedging value.

### 6.3.1 Circular Peg

First let us look at the insertion error response for both impedance controller insertions, Figure 6.21. We can notice that both the position and pose exceed the allowable error for the velocity impedance controller. As for the position based

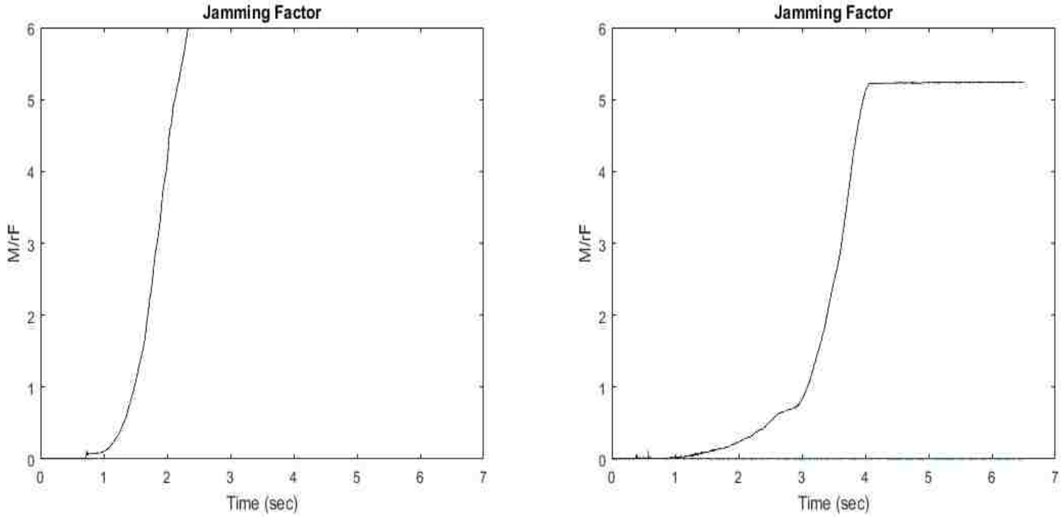

(a) Velocity Impedance Controller (b) Position based Impedance Controller

Figure 6.22: Circle peg jamming response. The black line is the modeled maximum jamming parameter and the blue line is the jamming response.

impedance controller, only the pose exceeds this tolerance initially. For the velocity impedance controller the insertion begins while this error is still outside this tolerance where as the position based impedance controller does not start insertion until the error is smaller than this tolerance.

Figure 6.22 shows the jamming parameter response of both impedance controllers. For the velocity impedance we see no visible jamming response whereas the position based impedance controller does have some initial response. For both controllers we see that jamming is the least likely mode of failure due to the compliance controllability of the controllers. As seen from the simulation, the velocity impedance controller responds better to external forces acting on the controller than the position based impedance controller.

Finally Figure 6.23 shows the insertion force profile for both impedance controllers. The velocity impedance controller follows the insertion force model better than the position based impedance controller method. The velocity impedance

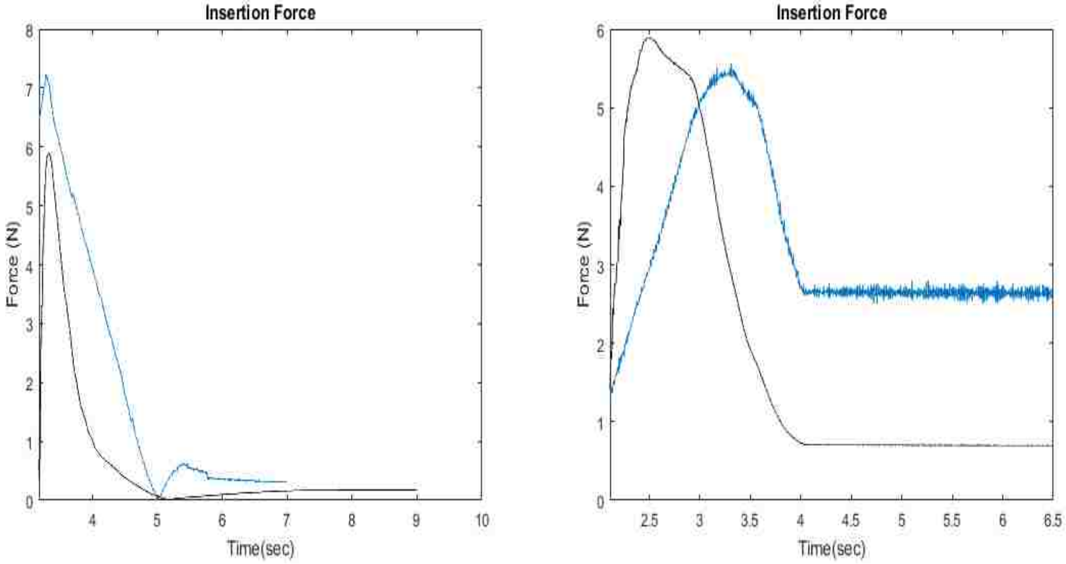

(a) Velocity Impedance Controller (b) Position based Impedance Controller

Figure 6.23: Circle peg insertion force. The black line is the modeled insertion force while blue line is the actual response.

controller does not have delay associated with it but does seem to significantly overshoot the model when compared to the position based impedance controller. Both controllers seem to have larger steady state responses than the modeled profiles.

### 6.3.2 Square Peg

For the square peg case the insertion error response for both impedance controllers is shown in Figure 6.24. For this insertion we can see that the pose error is initially large for one dimension when compared to the position based impedance response. The major difference between these two controllers is the lack of noise or chattering from the velocity impedance method. As discussed before, the position based impedance method has less stability when interacting with high stiffness environments compared to the velocity impedance controller. This can be seen in the difference in responses from this difficult insertion.

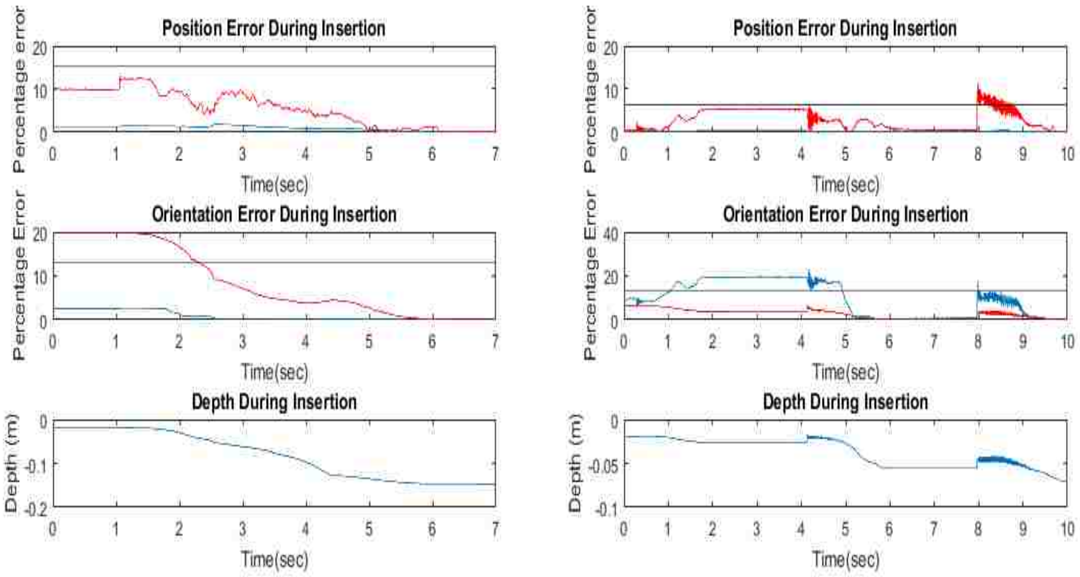

(a) Velocity Impedance Controller

(b) Position based Impedance Controller

Figure 6.24: Square peg insertion errors. The top graph shows position error, the middle graph shows orientation error, and last graph is the depth during insertion. The red lines correspond the $Y$ and $\theta_Y$ for the top and bottom graphs, respectively. The blue line corresponds to the $X$ and $\theta_X$ coordinate. The black horizontal lines are the maximum allowable wedging value.

Figure 6.25 shows the jamming parameter response for both controllers. As seen from the last insertion response, the velocity impedance controller has no visible jamming response when compared to the position based impedance controller. Again we see the difference in the smoothness from the actual response between the two controllers.

For the insertion force, Figure 6.26 shows the response of the two impedance controllers. Again we see that the velocity impedance controller is more similar to the modeled insertion response than the position based impedance controller. For this insertion we even see that the velocity impedance controller has less overshoot than the position based impedance controller. We also see that the insertion force settles down faster than the insertion model. There is also a noticeable difference in

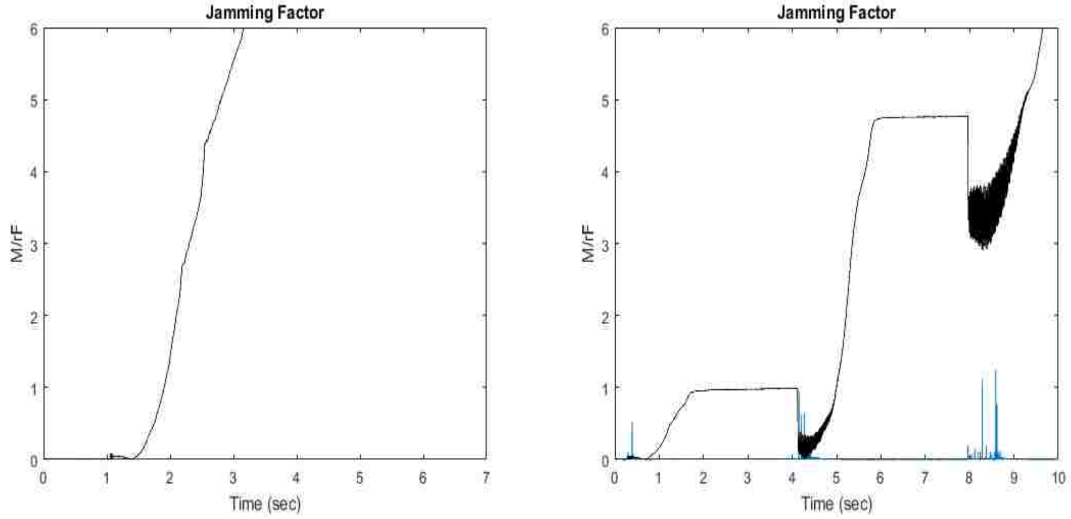

(a) Velocity Impedance Controller

(b) Position based Impedance Controller

Figure 6.25: Square peg jamming response. The black line is the modeled maximum jamming parameter and the blue line is the jamming response.

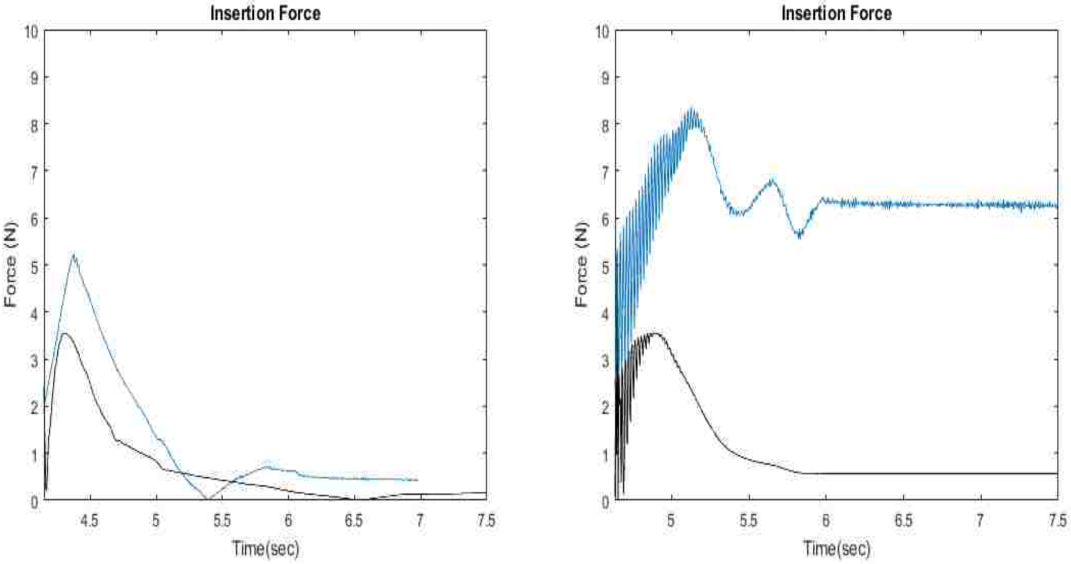

(a) Velocity Impedance Controller

(b) Position based Impedance Controller

Figure 6.26: Square peg insertion force. The black line is the modeled insertion force while blue line is the actual response.

the amount of overshoot for the position based impedance controller when compared to the overshoot from velocity impedance controller.

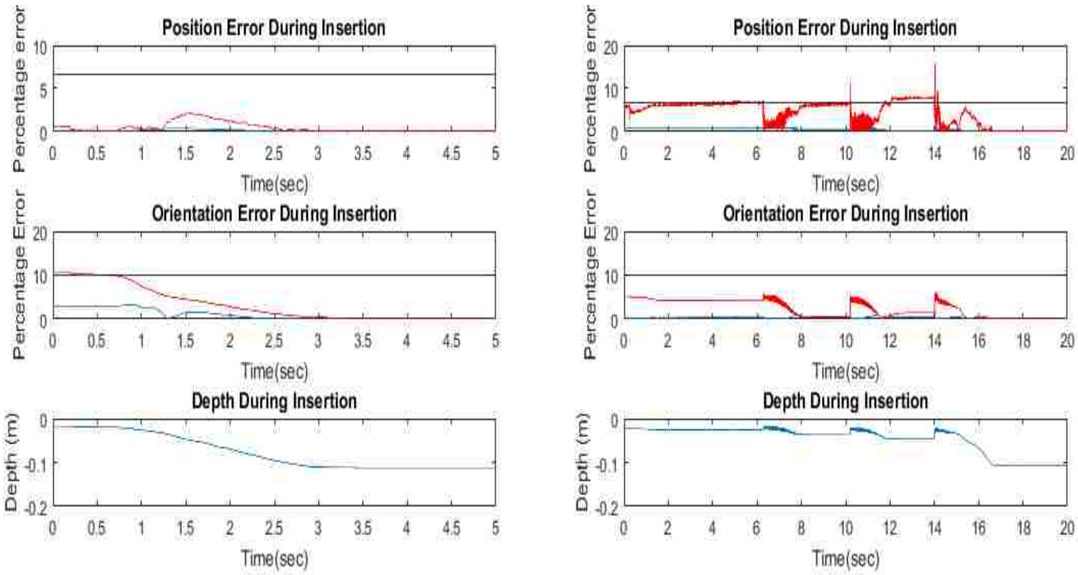

(a) Velocity Impedance Controller (b) Position based Impedance Controller

Figure 6.27: Cross peg insertion errors. The top graph shows position error, the middle graph shows orientation error, and last graph is the depth during insertion. The red lines correspond the $Y$ and $\theta_Y$ for the top and bottom graphs, respectively. The blue line corresponds to the $X$ and $\theta_X$ coordinate. The black horizontal lines are the maximum allowable wedging value.

### 6.3.3 Cross Peg

Starting with Figure 6.27, we see that the initial error is much smaller for the velocity impedance controller than for the other insertions. This does not follow the insertion model from section 4.2, since the cross geometry should be a more difficult insertion, with respect to wedging. We see this high error response from the position based impedance controller in its position response. When comparing the overall error between the two controllers, the velocity impedance controller method quickly falls within the wedging tolerance and begins the insertion quickly.

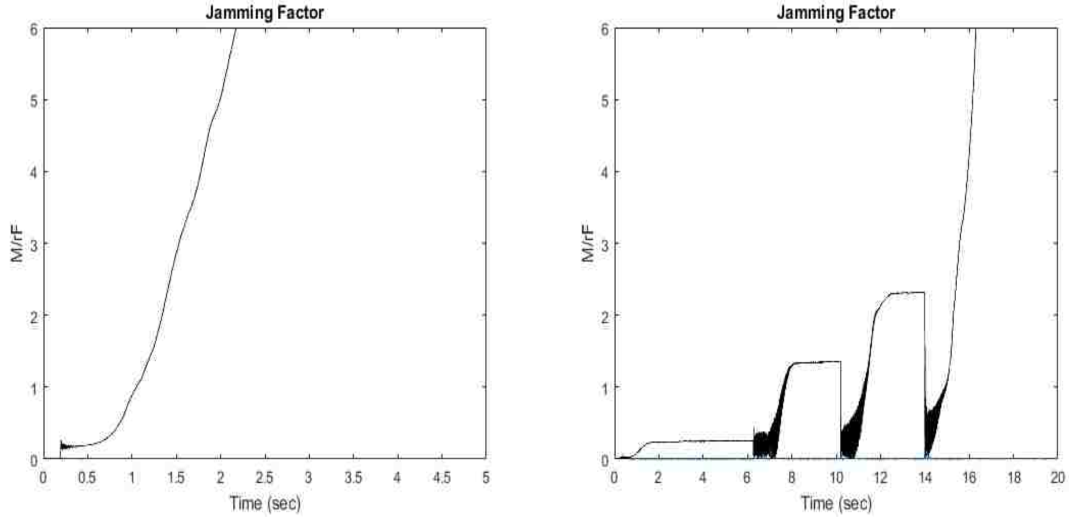

(a) Velocity Impedance Controller (b) Position based Impedance Controller

Figure 6.28: Cross peg jamming response. The black line is the modeled maximum jamming parameter and the blue line is the jamming response.

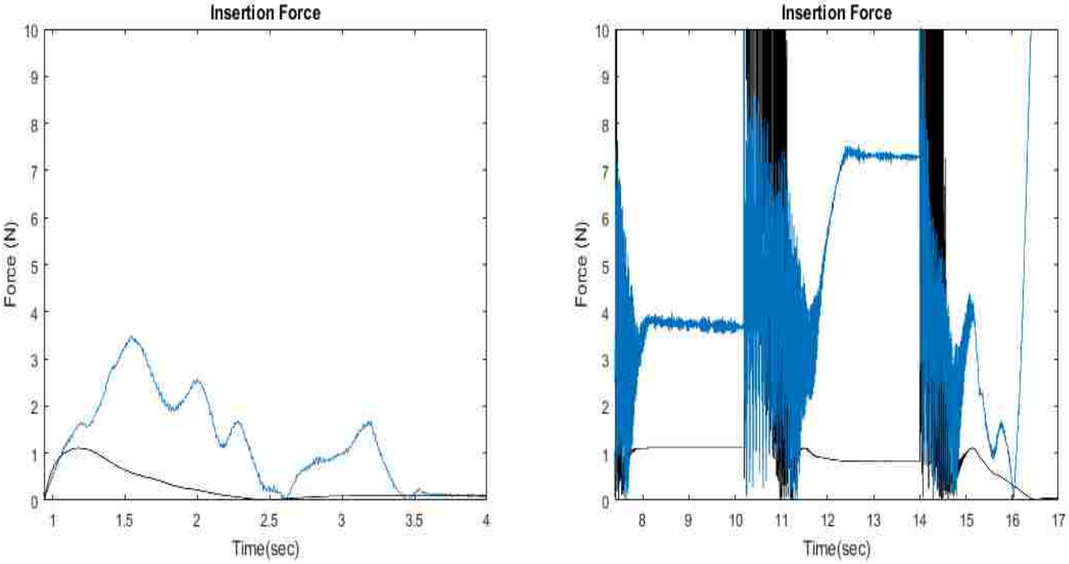

(a) Velocity Impedance Controller (b) Position based Impedance Controller

Figure 6.29: Cross peg insertion force. The black line is the modeled insertion force while blue line is the actual response.

Figure 6.28 shows the jamming responses between the two impedance controllers. For both controllers we see no visible jamming response. However, the velocity impedance controller has the more stable and smooth profile. This is due to the position based impedance controller needing three motions to complete the insertion. After the insertion finally begins for the position based impedance controller the jamming model quickly becomes similar to the velocity impedance controllers jamming model.

Finally, the insertion force response for both controllers is shown in Figure 6.29. Both insertion forces seem to be the least smooth for this insertion when compared to the previous insertions. Again for this insertion we see the velocity impedance controller follows the insertion force model better. There is a noticeable delay and overshoot in the velocity impedance controller. As for the position based impedance controller, the response is very noisy and on the final motion the insertion force has a similar shape but seems to settle at a very large force. Based off these two insertion force responses, it appears that the velocity impedance controller follows the insertion force model better than the position based impedance controller.

### 6.3.4 Against Gravity Peg

For this insertion the difficulty of the insertion is increased as gravity will be pulling down on the peg. As mentioned in chapter 5, the addition of gravity acting in the peg insertion is not modeled in the compliance model. We expect to have some additional noise introduced in the system from un-modeled external forces acting on our system. Figure 6.30 shows the response of the insertion errors of both impedance controllers. As we expected both the position and the pose errors are the largest for all the insertions for both controllers. The major difference between the two controllers is that the velocity impedance controller is able to quickly compensate for this error and insert the peg; whereas, the position based impedance controller

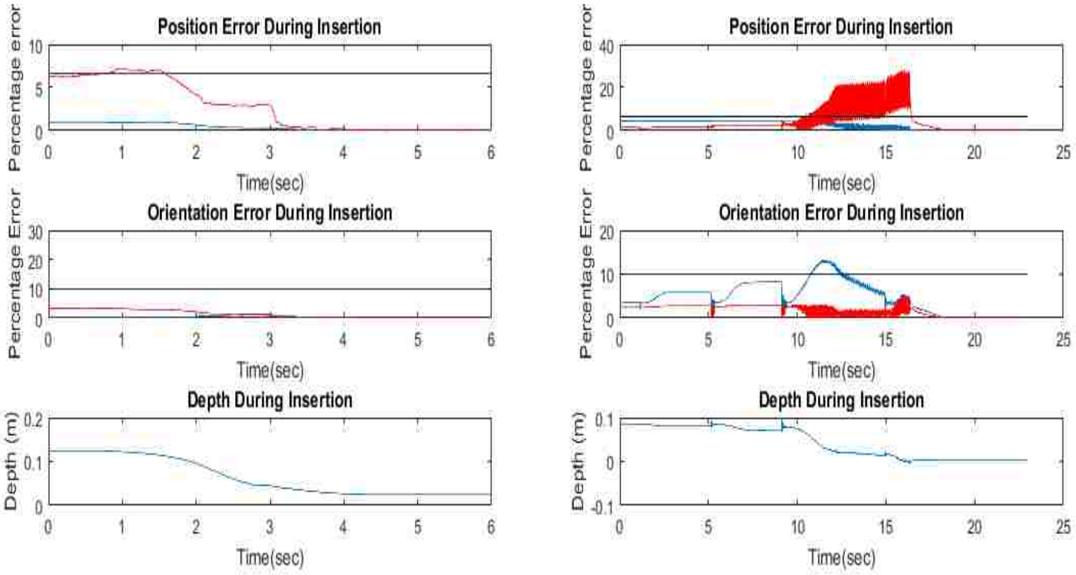

(a) Velocity Impedance Controller

(b) Position based Impedance Controller

Figure 6.30: Cross peg against gravity insertion errors. The top graph shows position error, the middle graph shows orientation error, and last graph is the depth during insertion. The red lines correspond the $Z$ and $\theta_Z$ for the top and bottom graphs, respectively. The blue line corresponds to the $X$ and $\theta_X$ coordinate. The black horizontal lines are the maximum allowable wedging value.

nearly loses stability inserting the peg. The addition of gravity acting on the peg during insertion is similar to increasing the stiffness of the environment acting on the peg. We see that this nearly causes the position impedance controller to become unstable. We also see that the additional presence of gravity acting on the peg does not affect the stability or the insertion.

Figure 6.31 shows the jamming parameter response between the two controllers. For the velocity impedance controller we still see no noticeable jamming response. The position based impedance controller does have some significant jamming response but this is well within the modeled tolerance.

The insertion forces for both controllers are shown in Figure 6.32. For this insertion we see the noisiest insertion force response for the velocity impedance controller.

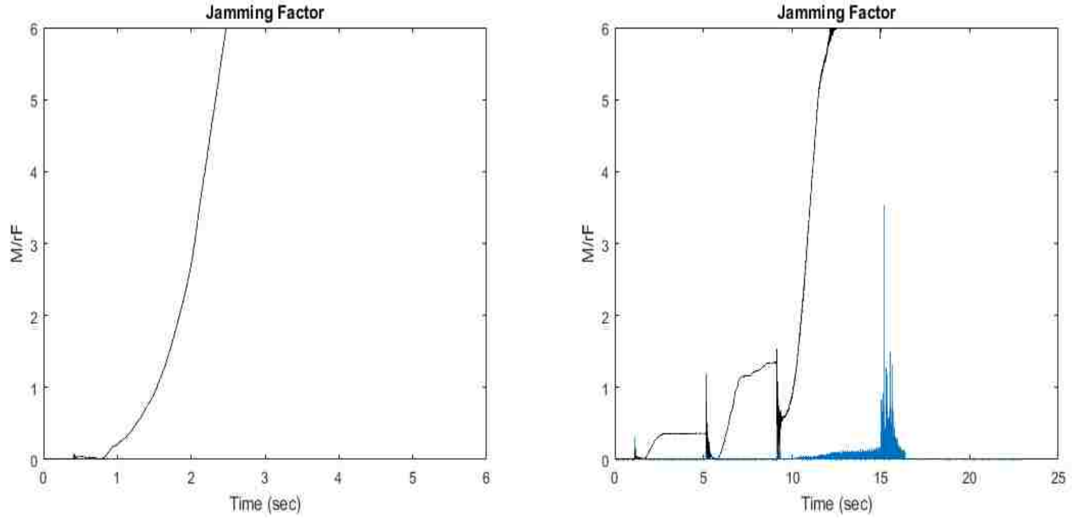

(a) Velocity Impedance Controller (b) Position based Impedance Controller

Figure 6.31: Cross peg against gravity jamming response. The black line is the modeled maximum jamming parameter and the blue line is the jamming response.

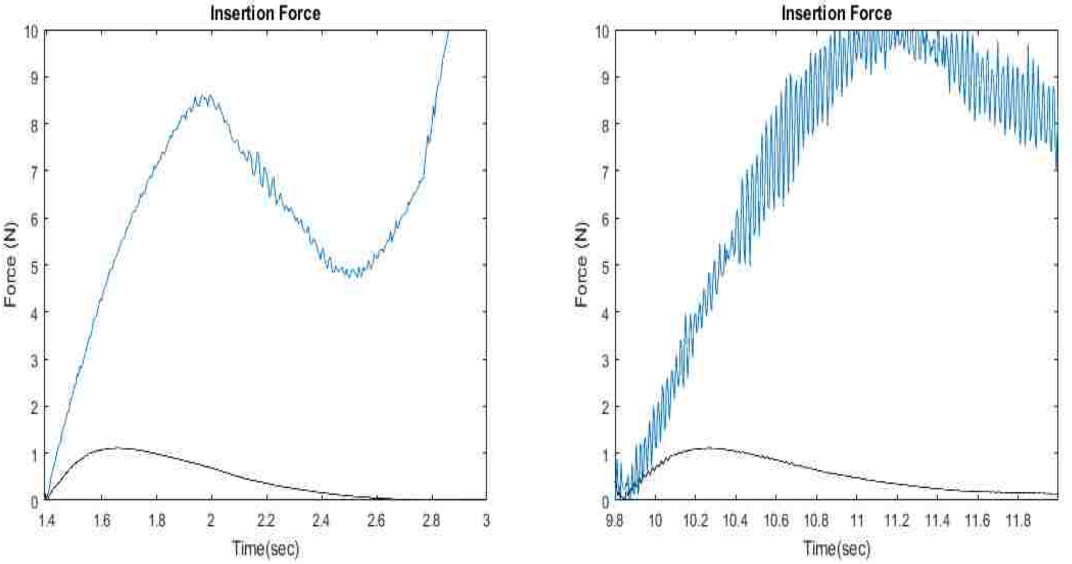

(a) Velocity Impedance Controller (b) Position based Impedance Controller

Figure 6.32: Cross peg against gravity insertion force. The black line is the modeled insertion force while blue line is the actual response.

Both impedance controllers have a significant delay and overshoot in response when compared to the models. The velocity impedance controllers insertion force seems to settle at a significantly larger force than the position based impedance controller.

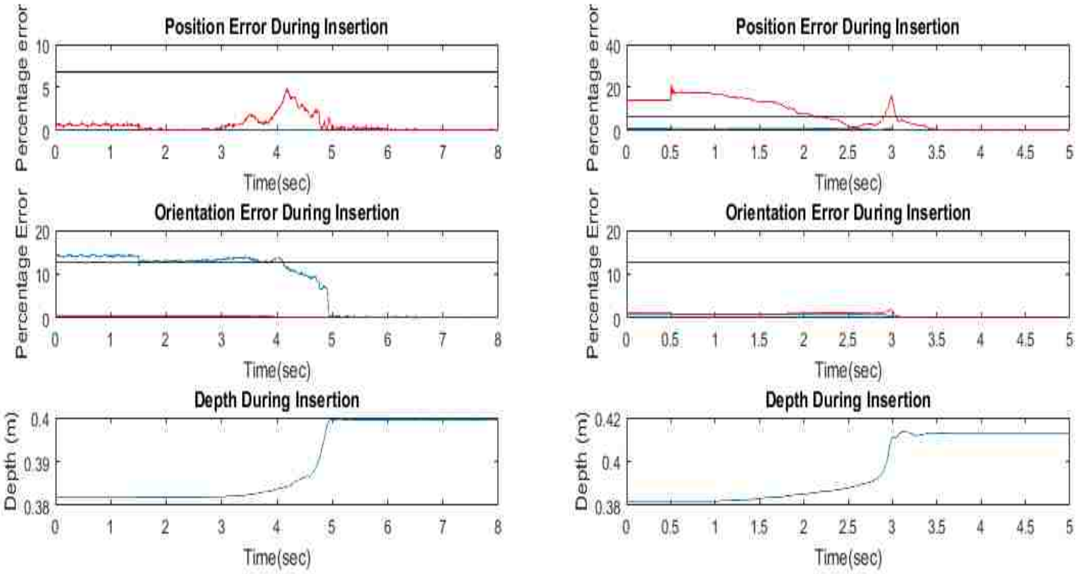

(a) Velocity Impedance Controller (b) Position based Impedance Controller

Figure 6.33: Key insertion errors. The top graph shows position error, the middle graph shows orientation error, and last graph is the depth during insertion. The red lines correspond the $Y$ and $\theta_Y$ for the top and bottom graphs, respectively. The blue line corresponds to the $Z$ and $\theta_Z$ coordinate. The black horizontal lines are the maximum allowable wedging value.

### 6.3.5 Key Insertion

For the key insertion we expect wedging to be the most difficult aspect of the insertion; in particular the axis gravity acts on, the $Z$-axis. From the position based impedance controller's insertion, we saw that the accuracy was the main factor to prevent the insertion of the key. We can see the response of both controllers key insertion in Figure 6.33. Instead, the velocity impedance controllers cause of error comes from the orientation of $\theta_Y$, the pose acting against gravity. Once this

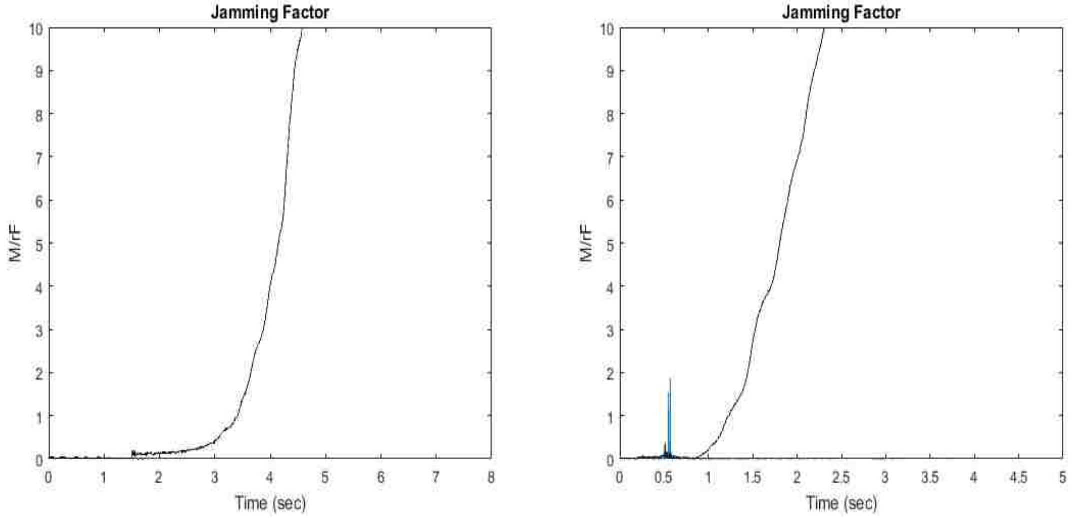

(a) Velocity Impedance Controller

(b) position based Impedance Controller

Figure 6.34: Key jamming response. The black line is the modeled maximum jamming parameter and the blue line is the jamming response.

pose becomes corrected by the vision system the insertion quickly happens. Both impedance controllers have similar quick insertion for this key insertion.

The jamming response for both controllers is shown in Figure 6.34. Here we again see initial spikes of jamming at the beginning of the position based impedance insertion and nearly no response from the velocity impedance controller. As we have expected for the key insertion model done in chapter 4, a jamming failure is very unlikely for these compliance controllers.

Finally we will look at the odd behavior from the insertion forces shown in Figure 6.35. Here we see that both insertion forces have some sort of delay, also see in the cross insertion against gravity. Similar to the cross insertion acting against gravity, the velocity impedance model approaches a larger force than the insertion model. From both of these responses we can see that not including the effects of gravity acting on the peg in the Whitney model is causing noticeable errors for the insertion force model.

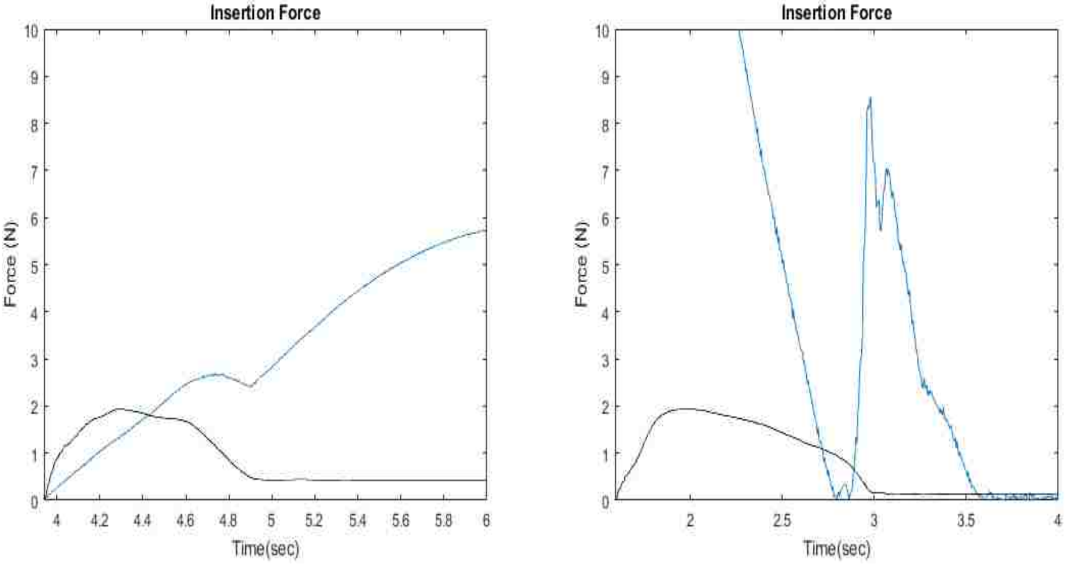

(a) Velocity Impedance Controller (b) position based Impedance Controller

Figure 6.35: Key insertion force. The black line is the modeled insertion force while blue line is the actual response.

As we have seen for all of the insertions, the velocity impedance controller maintains better stability than the position based impedance controller. Particularly in the cross insertion acting against gravity, we see the position impedance controller nearly become unstable. For all of the insertions, we see similar levels of initial insertion accuracy but faster insertion results compared to the position based impedance controller. This is due to the stable response from an external environment and having a closer response to the insertion force as modeled by Whitney. From these insertion results we see that the velocity impedance controller is a more stable compliant controller than the position based impedance controller that will improve object insertion results when compared to the position based impedance controller.

# Chapter 7

# Velocity Impedance Controller with Kinetic Friction Cone

In this chapter we will model the kinetic friction cone based upon the friction cone model presented in chapter 4. We will then simulate the improvement of insertion using this compliance model. After simulation, we will show experimentally the velocity impedance controller responses at higher stiffness values than the experiments done in chapter 5 and 6. We will show how varying the stiffness for the controller changes the accuracy and response of the system. Finally, we will look at some of the same insertions using the kinetic friction cone compliance model and compare the results with the simulation model and the previous insertion results.

## 7.1 Kinetic Friction Cone Insertion Model

The kinetic friction cone differs from the typical friction cone by its force limit and dynamically changing size. Equation (7.1) shows the friction cone angle relationship with respect to the normal force and the kinetic friction force. The kinetic friction cone has the same physical relationships as the static friction cone, in that there is a friction force acting against an object on contact. The two differences from the static case are that the frictional force has a linear relationship with the velocity of the object and that we want the force vector outside of the cone. Classically there is a velocity limit in kinetic friction where Coulomb friction will start to dominate; this is called the Stribeck effect. We will call these limits $v_{min}$ for the velocity and $F_c$ for the kinetic friction.

$$tan(\theta) = \frac{\mu_s v}{F_x} \tag{7.1}$$

Equation (7.1) shows the kinetic friction cone equation that is similar to the static friction cone. In this model we are going to ensure that our force vector, $F = [F_x, F_z]$, is outside of the cone. This is the major point of the kinetic friction cone model. This means that the insertion force is always larger than the kinetic friction force $F_z > \mu_s v$.

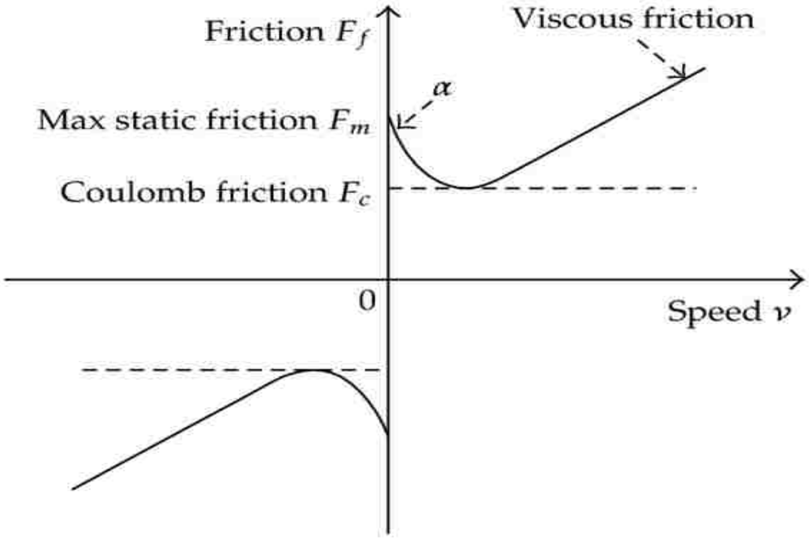

Figure 7.1: Kinetic friction model, where $F_m$ is the static friction force and $F_c$ is the minimum friction before the onset of the Stribeck effect

Figure 7.1 shows the velocity limit at the onset of the Stribeck effect, or $F_c =$

$\mu_s v_{min}$ where $\mu_s$ is the kinetic coefficient for kinetic friction. For the kinetic friction cone model we need the model to be able to prevent both modes of failure, jamming and wedging. Starting with wedging prevention, we will use the same Whitney wedging model to determine the compliance required to prevent wedging while moving. To prevent jamming we need to ensure that the insertion force is larger than the resistant kinetic friction force. Therefore, to prevent failure for the kinetic friction model we will use the following relationships.

Using equation (7.1) and the fact that $\tan(\theta) = \frac{L}{d}$ and $L\tan(\theta) = cD$, from section 4.1, we can solve for a minimum orientation error for the wedging model. Using the small angle approximation we get the following orientation relationship with the kinetic friction.

$$\theta < \frac{F_x cD}{\mu_s v d} \tag{7.2}$$

The major difference between the kinetic friction cone wedging model and the Whitney quasi-static model is that the orientation, $\theta$, is now a function of lateral force and velocity. So by this definition we see that decreasing the insertion velocity and increasing the lateral force prevents wedging.

For jamming, we will calculate Whitney's jamming parameter with respect to the kinetic forces acting on the peg during insertion.

$$\lambda = \frac{F_x z}{\mu_s v D} \tag{7.3}$$

The last two restrictions for the kinetic friction cone model will ensure that the robot is constantly moving during insertion. This means that the robot never encounters the Stribeck effect until the insertion is completed.

$$F_z > F_c \tag{7.4}$$

$$v > v_{min} \tag{7.5}$$

From equations (7.2) and (7.3) we see that the jamming and wedging model will now be affected by the velocity of the insertion and the lateral force of the insertion. Equation (7.4) determines the minimum insertion force to maintain motion during insertion and equation (7.5) restricts the insertion velocity to never reach the minimum.

### 7.1.1 Kinetic Friction Wedging Model

The main difference in the wedging model is in the increased upper bounds in allowable orientation error with respect to lateral insertion force and decreased bounds with respect to the insertion velocity. To show this we need to again look at the Whitney wedging error model and compare this to the kinetic friction cone (KFC) model. As the lateral error $(R - r) > |\epsilon|$ does not change between the two models we will only be looking at how the orientation, $\theta$, changes.

$$\begin{aligned} \theta_{KFC} &< \frac{F_x cD}{\mu_s v d} \\ \theta_{Whitney} &< \frac{cD}{\mu d} \end{aligned} \tag{7.6}$$

From Equation (7.6) we can see that the Whitney orientation error remains constant for all lateral forces and insertion velocities. This means that the allowable orientation error can vary with changes to the insertion velocity and the lateral force during insertion. To see how the orientation error can change with respect to the insertion velocity and lateral we will look at Figure 7.2.

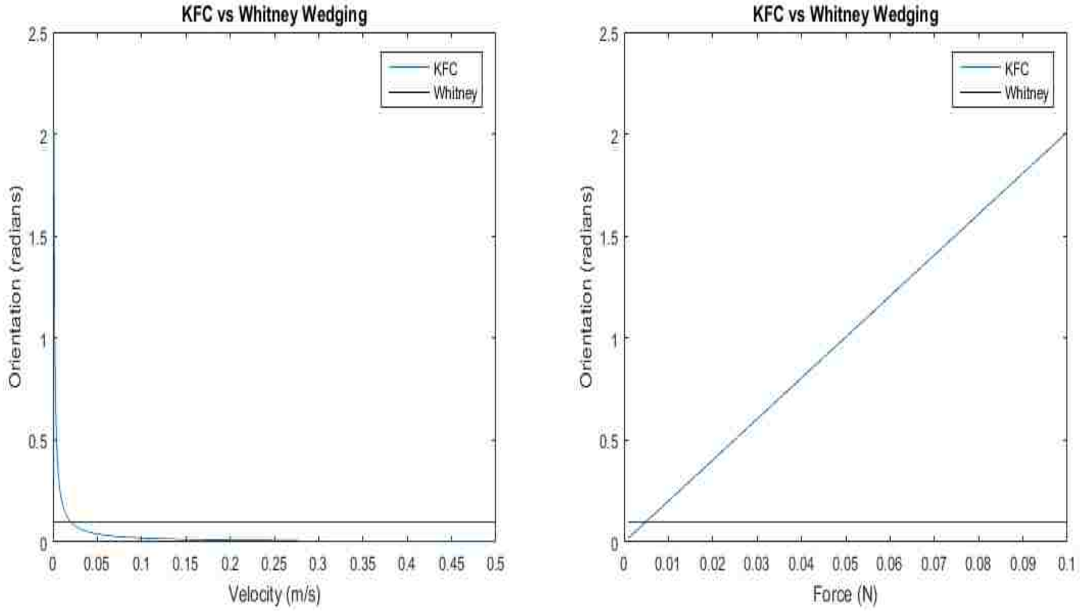

(a) Insertion Velocity

(b) Lateral Force

Figure 7.2: Comparison of the KFC model and Whitney model while varying the insertion velocity or the lateral force

We can see that in the case where the force is held constant that the lower velocities allow for more orientation errors than the Whitney model. Looking at the lateral force, with a constant velocity, the force linearly improves the allowable orientation error. In both cases we can see that the KFC model intersects the Whitney model at some force and velocity, this intersection is defined by $\mu F_X = \mu_s v$. For the insertions testing the KFC model we will try to maintain this relationship. We will do this to compare the Whitney wedging model and the KFC wedging model. Although we will try to maintain that $\mu F_X = \mu_s v$ is true, there will actually be variance so we will compare the KFC model to show that this variance improves the wedging model.

### 7.1.2 Kinetic Friction Jamming Model

We will again compare the difference in the jamming model between the KFC and the Whitney model. For the jamming model's force relationship, we first get the relationship between the lateral and insertion force $\frac{F_x}{F_z} < \frac{F_x}{\mu_s v}$. From this we get a familiar requirement to prevent jamming $F_z > \mu_s v$, which ensures that equation (7.3) is true at even the lowest allowable velocity, $v_{min}$. We see that we have the same upper bound relationship as the wedging model. The following equation shows the difference between the jamming parameter for the KFC model and the Whitney model.

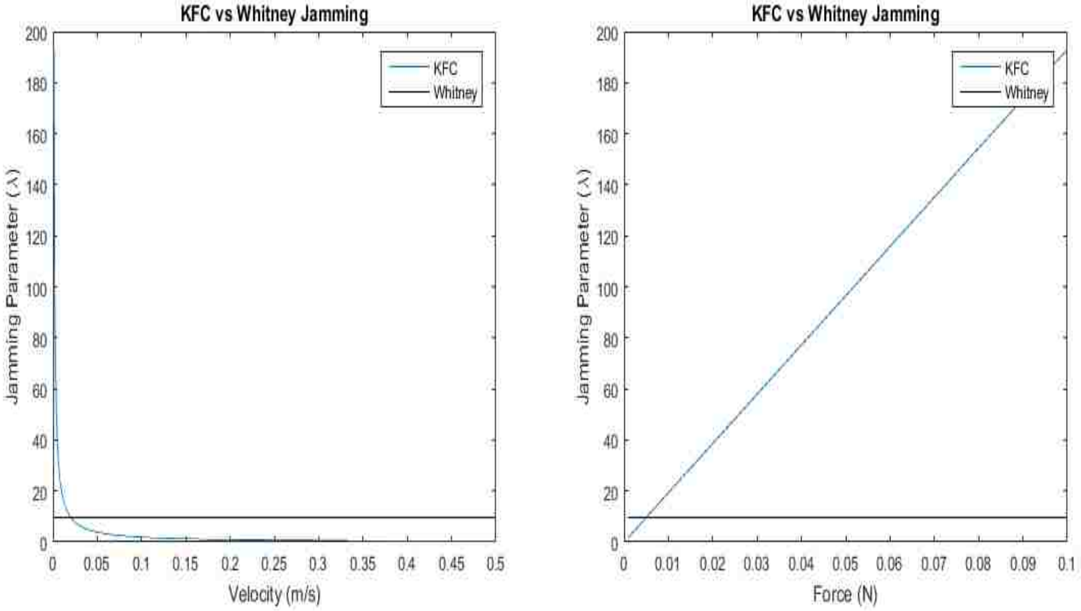

(a) Insertion Velocity

(b) Lateral Force

Figure 7.3: Comparison of the KFC model and Whitney model while varying the insertion velocity or the lateral force

$$\begin{aligned}\lambda_{KFC} &= \frac{F_x z}{\mu_s v D} \\ \lambda_{Whitney} &= \frac{z}{\mu D}\end{aligned} \tag{7.7}$$

Similar to equation (7.6) we see that the jamming parameter will behave similar to the wedging. Figure 7.3 shows this relationship between the KFC and the Whitney jamming parameter. From Figure 7.3 we see the same type of profile for how the jamming parameter varies for insertions velocities and lateral forces. We also see that the jamming parameter has the same intersection point between the Whitney and KFC model where $\mu F_X = \mu_s v$. This means that now the impedance controllers now have two methods of preventing jamming. The controller can now vary the compliance to minimize $\frac{M}{rF_z}$ or also control the insertion velocity and lateral force.

### 7.1.3 Kinetic Friction Cone Compliance Model

The Whitney model for insertion assumes quasi-static force interaction. We will impose an extra kinetic friction constraint. In particular we will set the kinetic friction to be approximately the same as the static friction force. From Figures 7.2 and 7.3 this is the point where the KFC model intersects the Whitney model.

$$\mu F_x \approx \mu_s v \tag{7.8}$$

Equation (7.6) can be rewritten as $F_x \approx \frac{\mu_s v}{\mu}$. By setting this constraint we can preserve the Whitney jamming model. To relate this back to the reaction forces the robot and peg would expect to experience from the insertion we have to split the analysis into the one-point contact and two-point contact conditions. Once again for

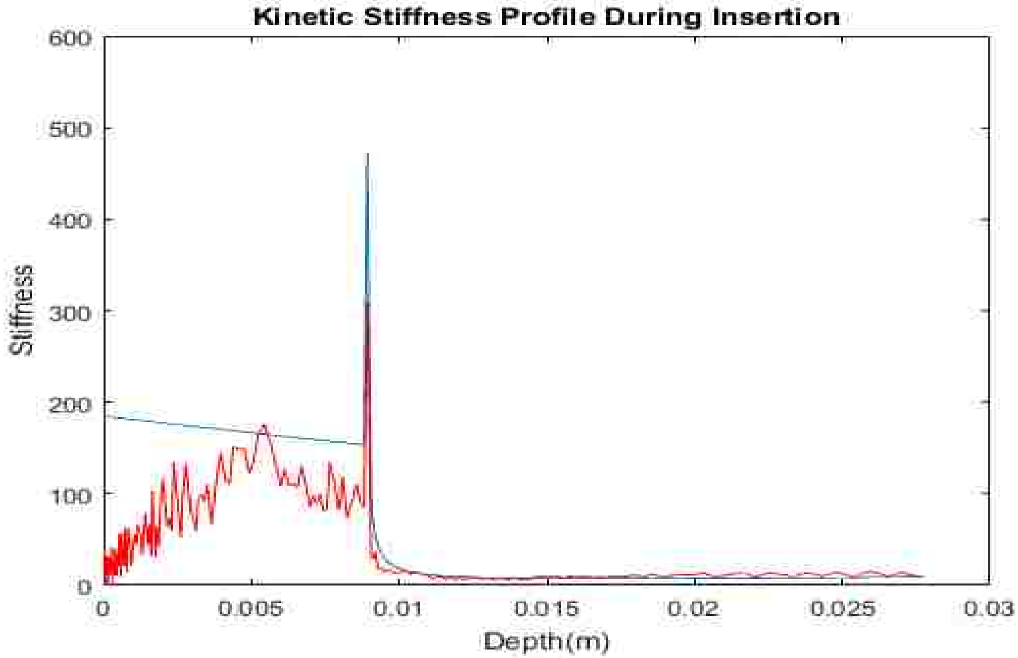

Figure 7.4: Minimum stiffness profile during Cross peg insertion. The blue line is estimating the profile with a constant velocity and the red line is calculating the velocity.

both stages we have a predetermined $\frac{K_\theta}{K_x}$. Finding the control stiffness for the one point contact we will combine (4.21) with $F_z > \mu_s v$.

$$K_x > \frac{\mu_s v}{\mu}[\frac{\frac{K_x}{K_\theta}(L - z - \frac{\mu d}{2})(L - z) + 1}{\epsilon_0 - \frac{cD}{2} + l\theta_0}] \tag{7.9}$$

We can see that as the depth increases the stiffness required decreases. Solving for the stiffness for the two-point contact, we will combine (4.28) and $F_z > \mu_s v$.

$$K_x > \tfrac{\mu_s v}{a} \tag{7.10}$$

$$a = \frac{2\mu}{z}[(L^2 + \frac{K_\theta}{K_x}) \quad (\theta_0 - \tfrac{cD}{z}) + L(\epsilon_0 + \tfrac{cD}{2})] + \mu(1 + \tfrac{\mu d}{z})[-L(\theta_0 - \tfrac{cD}{z}) - (\epsilon_0 + \tfrac{cD}{2})] \tag{7.11}$$

For this model we will look at the differences when we treat $v$ as constant vs. when it is used as a variable for insertion. To do this we will take an insertion profile from one of the previous insertions, in particular the cross insertion for the velocity impedance controller. Figure 7.4 shows the minimum stiffness needed for the kinetic friction model. Here we compare the response using a constant velocity model with dynamically calculating the velocity during the insertion. From Figure 7.4, we can see that the constant velocity profile is either very close to the actual velocity profile or larger than the actual profile. The profile we are calculating is the minimum stiffness required for a successful insertion. For our insertions we will be using compliance parameters much larger than these values so we do not need to worry about jamming.

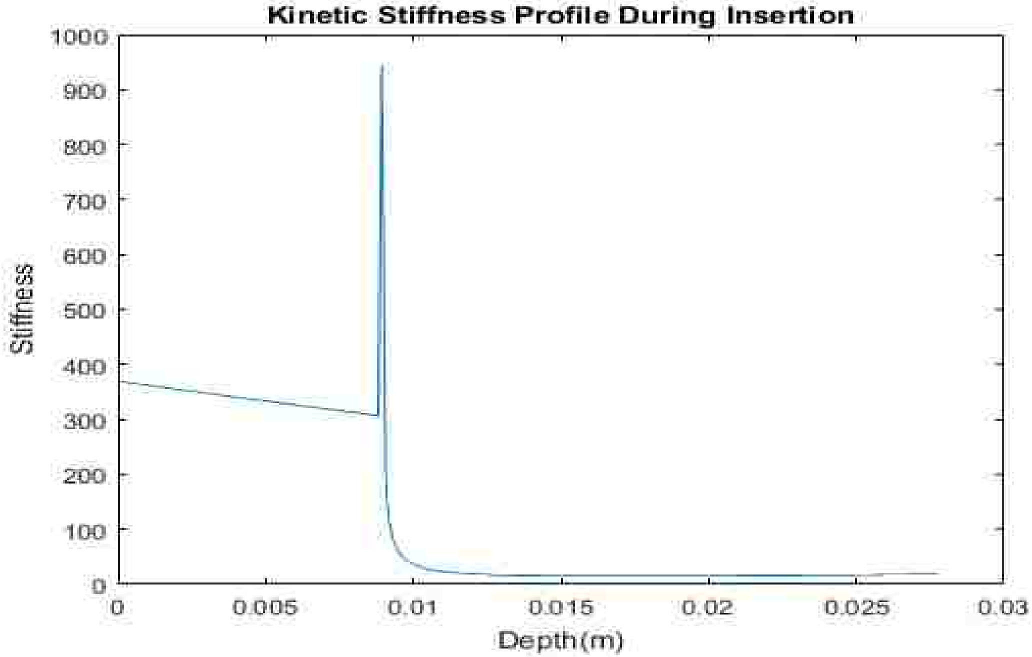

Figure 7.5: Stiffness profile during insertion.

This explains why there is no jamming in all of the insertions for both impedance controllers. The largest value from the minimum required stiffness profile during the two point contact is about $K_X \approx 475\frac{N}{m}$. Since all insertions were done well above this value, with the insertion stiffness set at $K_X = 500\frac{N}{m}$, we never saw any jamming issues after the initial point of contact. For insertion testing using this compliance model we will use the same profile as the minimum stiffness profile. However, we will be doubling the stiffness values for our controller during the insertion. This stiffness profile is shown in Figure 7.5

For wedging, we can see that the differences made to the model is the allowable orientation error, $\theta < \frac{F_x c D}{\mu_s v d}$. In the general case we can see that the best wedging prevention strategy would be to insert as slowly as possible and to provide the most amount of lateral force. The issue with this strategy is that increasing the lateral force requires more energy from the robot during insertion. For jamming, we have already established that jamming will be prevented as long as $F_z > \mu_s v$. In other words, as long as the insertion force is larger than the kinetic friction force then increasing the lateral force during insertion will not cause jamming. Finally we also see that the jamming parameter, $\lambda = \frac{F_x z}{\mu_s v D}$, decreases as we increase the insertion velocity and decrease the lateral force. This means that the likelihood of jamming will increase as we increase the velocity during insertion. This is the draw back to high speed insertions, but with an active complaint controller we can vary the compliance during insertion to prevent jamming. Finally we note that by setting $F_x \approx \frac{\mu_s v}{\mu}$, the wedging and jamming parameters return to the same Whitney parameters determined in chapter 4.

## 7.2 Insertion Testing with Kinetic Friction Cone Model

Shown in Figure 7.6 is the kinetic friction cone control model. We will use the kinetic friction cone restrictions to control the velocity through the path planner and we will prevent jamming using the kinetic friction compliance parameters. For

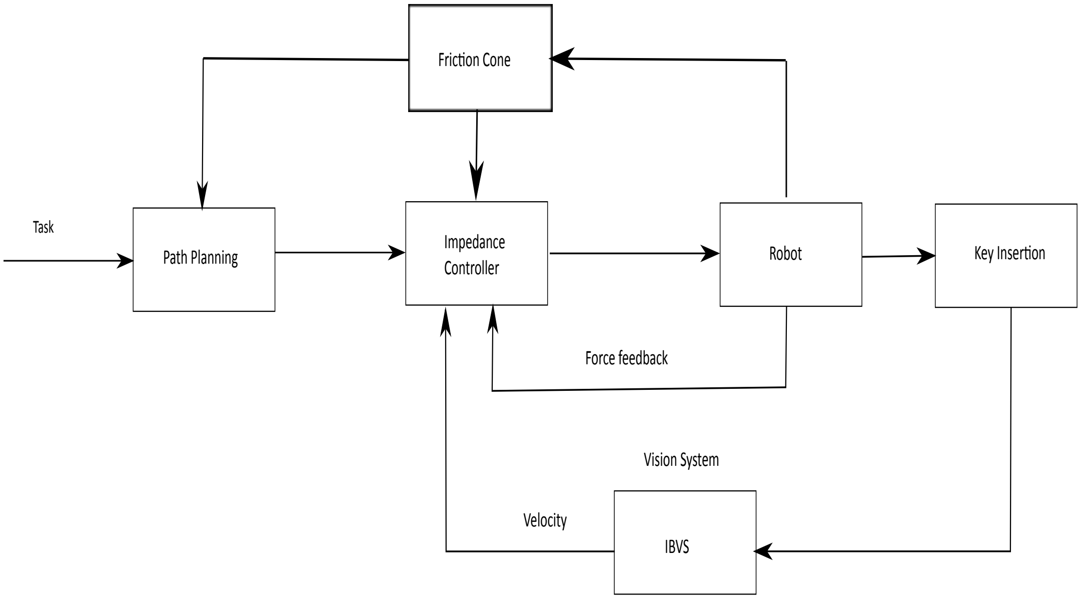

Figure 7.6: Model of kinetic friction cone controller. (KFC-VIC)

the compliance parameters we will complete all of the insertions using the stiffness values from equations (7.9)-(7.11). To accomplish this we can only use the velocity impedance controller since the position based impedance controller will lose stability at these compliance values. We will call this enhanced velocity impedance compliance controller the kinetic friction cone velocity impedance controller (KFC-VIC) and the velocity impedance controller (VIC).

To be able to compare the insertion results from the quasi-static model to the dynamic model we will set the lateral force to $F_x \approx \frac{\mu_s v}{\mu}$ to be able to compare the difference in the models. When we compare the Whitney wedging model, $\theta < \frac{cD}{\mu d}$, with the kinetic friction cone model wedging, $\theta < \frac{F_x cD}{\mu_s v d}$, we expect insertions to be possible when the Whitney model predicts wedging failure. In the Whitney model we always need the error to be below a set value but for the kinetic friction cone model the error tolerance can be increased as the insertion velocity and lateral force vary. This explains why multiple insertions succeeded in chapters 5 and 6 when the

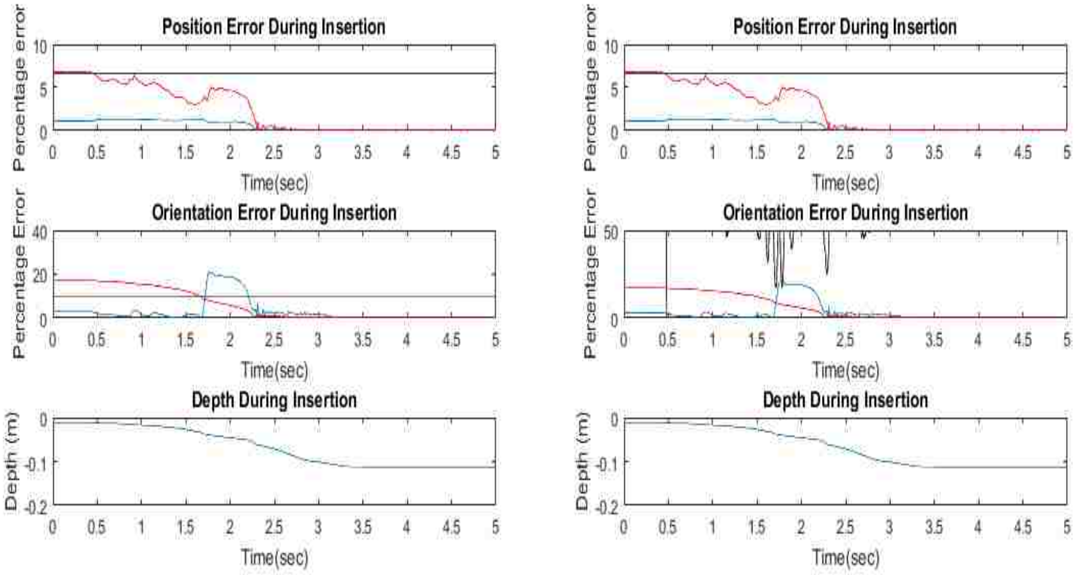

(a) Whitney Model

(b) KFC Model

Figure 7.7: Cross peg insertion with KFC-VIC. The top graph is position error, the middle graph orientation error, and the last graph depth of insertion.The red lines correspond the $Y$ and $\theta_Y$ for the top and bottom graphs, respectively. The blue line corresponds to the $X$ and $\theta_X$ coordinate. The black lines are the maximum allowable wedging value, Whitney model for (a) and KFC model for (b).

insertions should have failed due to wedging. In this section we will only compare the velocity impedance controller's response without the kinetic friction cone compliance and with its compliance model. This will show that the Whitney model predicts a failure when the insertion will actually succeed. We will also display the KFC wedging model during these insertions to display how the insertions are able to succeed.

### 7.2.1 Cross Insertion

First, let us look at the error response between the Whitney and the KFC wedging model. Figure 7.7 shows the response of the cross insertion for the KFC-VIC and Figure 7.8 shows the response for the VIC. In both figures we see that the KFC

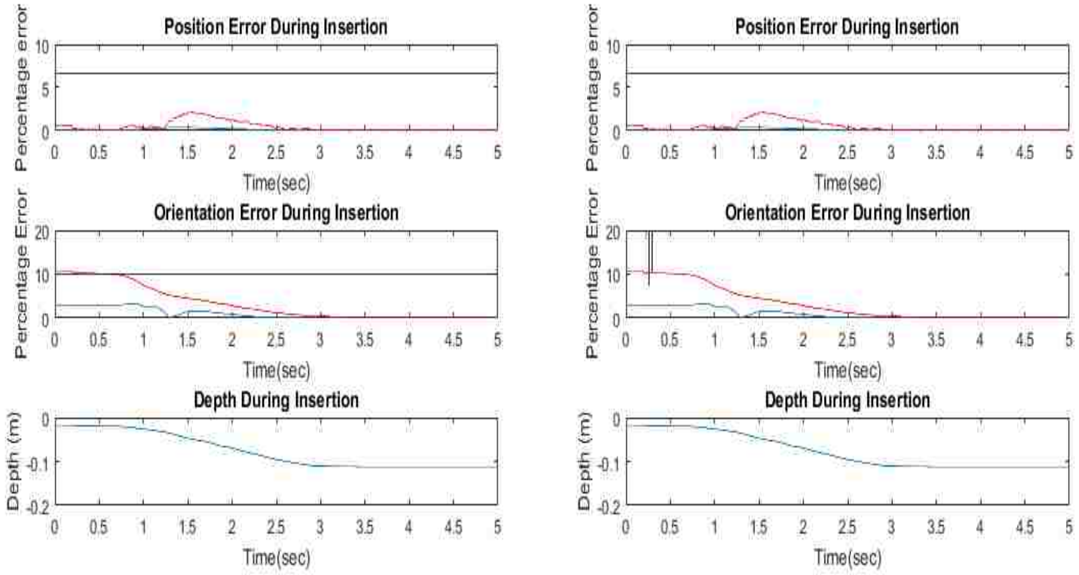

(a) Whitney Model

(b) KFC Model

Figure 7.8: Cross peg insertion with VIC. The top graph is position error, the middle graph orientation error, and the last graph depth of insertion.The red lines correspond the $Y$ and $\theta_Y$ for the top and bottom graphs, respectively. The blue line corresponds to the $X$ and $\theta_X$ coordinate. The black lines are the maximum allowable wedging value, Whitney model for (a) and KFC model for (b)

model only intersects with the error at a few points during the insertion. In Figure 7.7 we see that the Whitney model has multiple points in the orientation error where the insertion should fail whereas the KFC model barely intersects at this point. In Figure 7.8 we see that the Whitney model has a better initial model of the error, as the insertion does not begin until the error drops below this threshold. This is due to the fact that at the beginning of the insertion the peg is hardly moving and this would make the allowable error to become incredibly large, as shown in Figure 7.2(a).

The first noticeable difference between the controllers is how the KFC-VIC has multiple points where the error is greater than the maximum wedging error predicted by the Whitney model. This shows that while we increase the velocity of the insertion

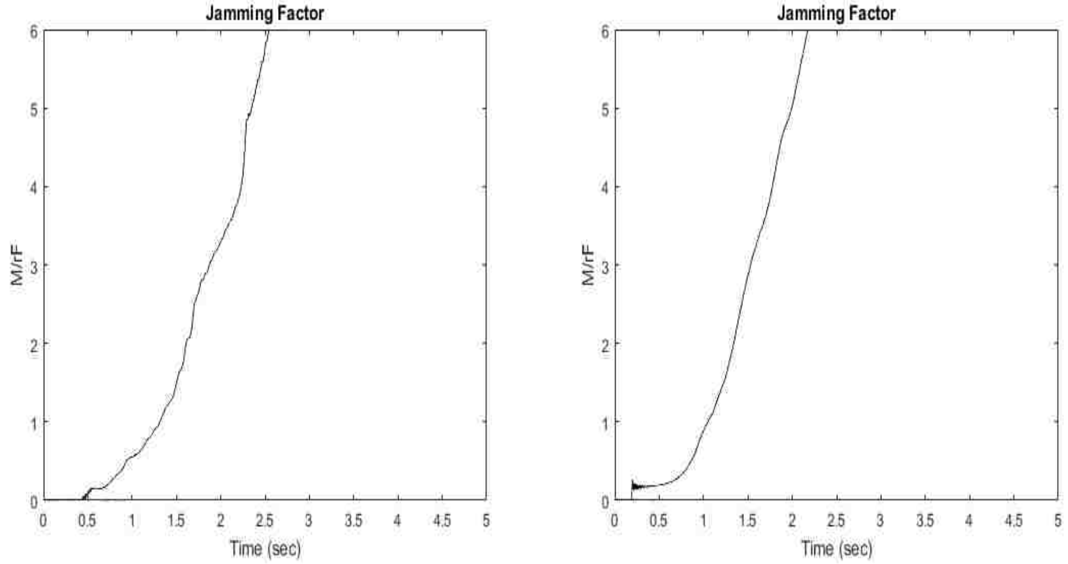

(a) KFC-VIC

(b) Velocity Impedance Controller

Figure 7.9: Cross peg jamming response. The black line is the modeled maximum jamming parameter and the blue line is the jamming response.

we also increase the position and orientation error.

In Figure 7.9 we see the jamming response generated by both controllers. As we have seen in all insertions for both the position based impedance controller and the velocity impedance controllers and again in Figure 7.9, there is no noticeable jamming response when compared to the maximum allowable jamming parameter, the black line in Figure 7.9. This is very important because increasing the velocity also increases the likelihood for jamming, as shown in Figure 7.3 (a). Both compliance models are good enough to prevent causes for concern with jamming. For the rest of the insertions we will not look at the jamming responses since the compliance controllers significantly reduces the likelihood of failure from jamming.

In Figure 7.10 we compare the experimental insertion force to the modeled insertion force. The profiles of the actual insertion forces are very similar between the two controllers. The kinetic friction cone model has a larger error but this is mostly due

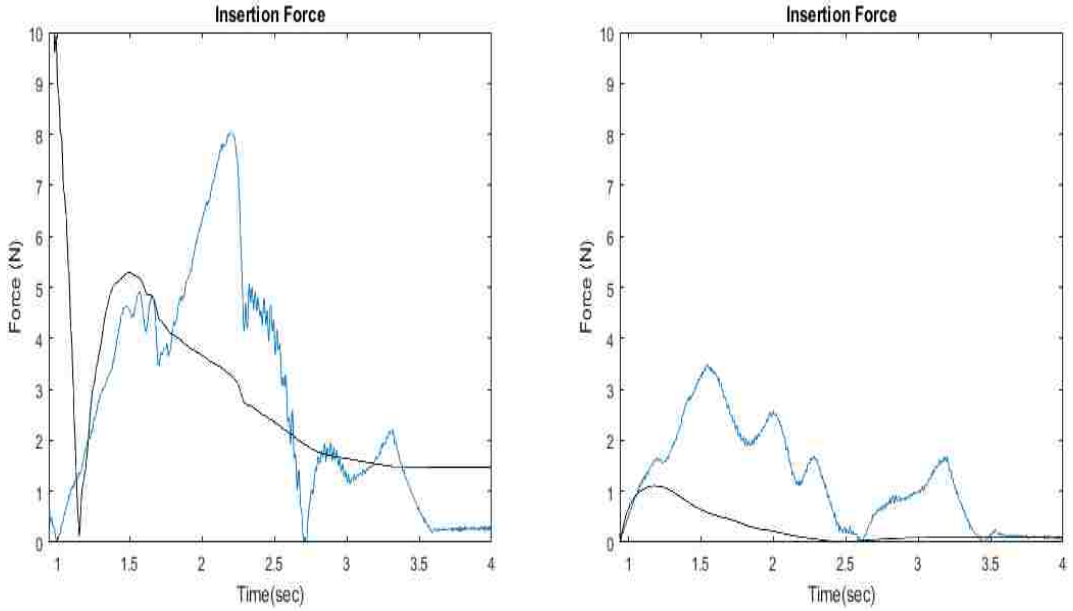

(a) KFC-VIC

(b) Velocity Impedance Controller

Figure 7.10: Cross peg insertion force. The black line is the modeled insertion force while blue line is the actual response.

to the fact that this insertion force model uses the Whitney insertion force model. This means that there are dynamic responses from the reaction forces during insertion not modeled, such as damping forces from the robot and the environment. This also explains why the initial insertion force response closely resembles the Whitney model as the velocities are small enough where kinetic friction force starts to become $\mu F_X = \mu_s v$.

Based on Figures 7.7 and 7.8 we can see that the the KFC model predicts successful insertions even when the Whitney model predicts the insertion to fail. The caveat is that this requires the robot to push against the environment more than the regular model. For the position based impedance controller this additional force to the environment will likely cause the controller to become unstable which makes the KFC model only possible with the velocity impedance controller.

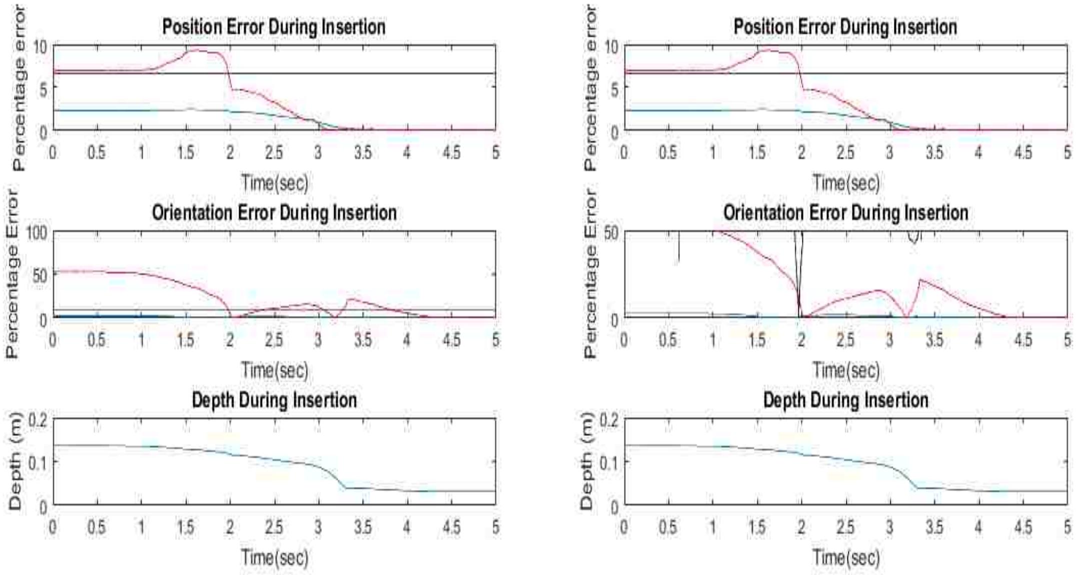

(a) Whitney Model

(b) KFC Model

Figure 7.11: Cross peg insertion against gravity for KFC-VIC. The top graph is position error, the middle graph orientation error, and the last graph depth of insertion. The red lines correspond the $Z$ and $\theta_Z$ for the top and bottom graphs, respectively. The blue line corresponds to the $X$ and $\theta_X$ coordinate. The black lines are the maximum allowable wedging value, Whitney model for (a) and KFC model for (b)

### 7.2.2 Cross Insertion Against Gravity

Now let us look at the error response from the cross insertion acting against gravity, Figures 7.11 and 7.12 shows this error response for the cross peg insertion against gravity. In both figures we see that the KFC models the wedging failure threshold better than the Whitney model. We also see that the KFC-VIC has much larger errors than the VIC again.

As in the previous insertion, we see the KFC-VIC has significant error during the insertion, which should cause it to fail. We also have similar insertion profiles from the previous cross insertion with the velocity impedance controller. Again we see from the KFC model, the insertion is able to be successful even with errors where

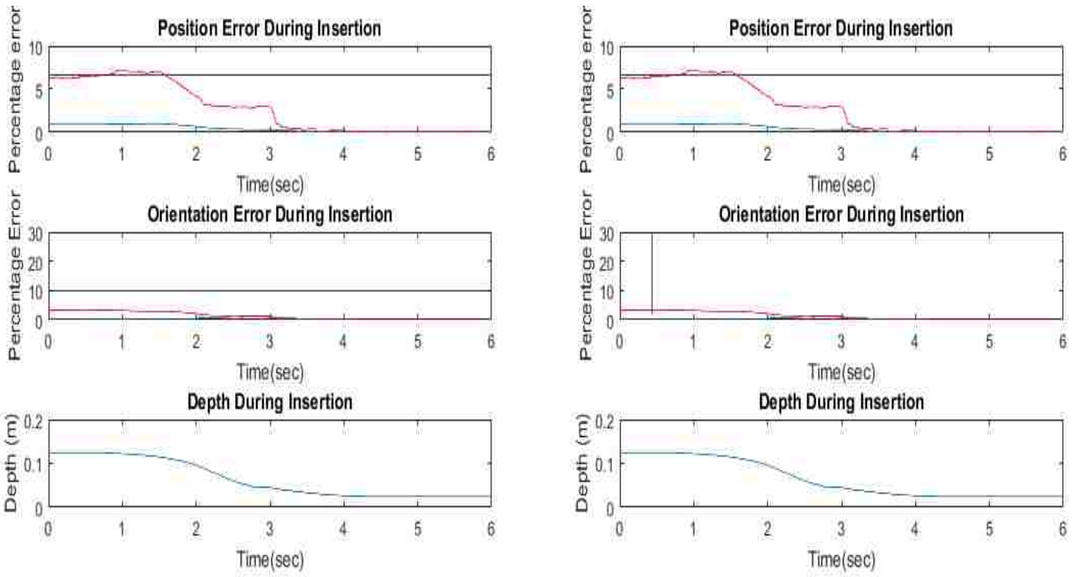

(a) Whitney Model

(b) KFC Model

Figure 7.12: Cross peg insertion against gravity for VIC. The top graph is position error, the middle graph orientation error, and the last graph depth of insertion. The red lines correspond the $Z$ and $\theta_Z$ for the top and bottom graphs, respectively. The blue line corresponds to the $X$ and $\theta_X$ coordinate. The black lines are the maximum allowable wedging value, Whitney model for (a) and KFC model for (b)

the Whitney model predicts wedging failure.

Figure 7.13 shows the insertion force response for cross peg insertion against gravity. For this insertion the KFC-VIC is more similar to the insertion model than the VIC. As was the case for the position based impedance controller, both insertion forces settle at much larger values than those predicted by the Whitney insertion force model. This is likely due to the gravity acting on the peg because gravity causes the peg to experience an additional moment and force not modeled in the Whitney model. We also see that the insertion force required for the KFC-VIC for this insertion is still larger than the velocity impedance controller.

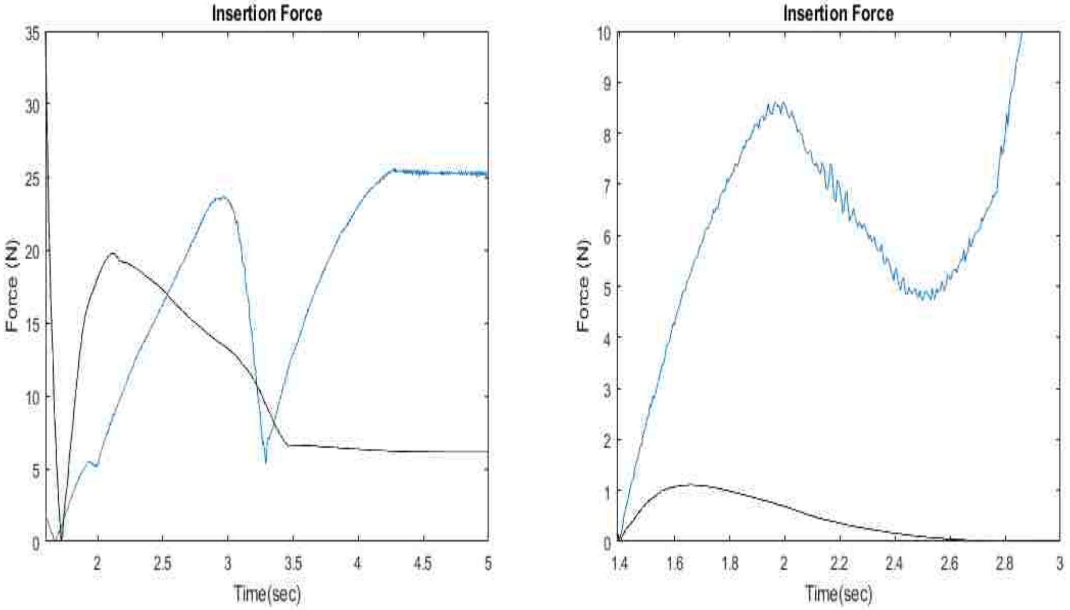

(a) KFC-VIC

(b) Velocity Impedance Controller

Figure 7.13: Cross peg insertion force against gravity. The black line is the modeled insertion force while blue line is the actual response.

### 7.2.3 Key Insertion

The final insertion we will compare for the KFC model is the key insertion. Figures 7.14 and 7.15 show the errors from the experimental response for the key insertion. For this insertion we see a few points where the error intersects with the maximum allowable wedging value. There is a point where the KFC-VIC passes the error threshold and the insertion still continues for the KFC model. We see the KFC model has multiple points of intersection for the VIC. Interesting enough the last points where the error intersects with the KFC model the insertion hastens. In the Whitney model, we see that the insertions begin when the errors fall below the Whitney models threshold. The insertion velocity for this experiment is low enough where the Whitney model is the more accurate model.

Figure 7.16 shows the insertion force responses during key insertion. In this image

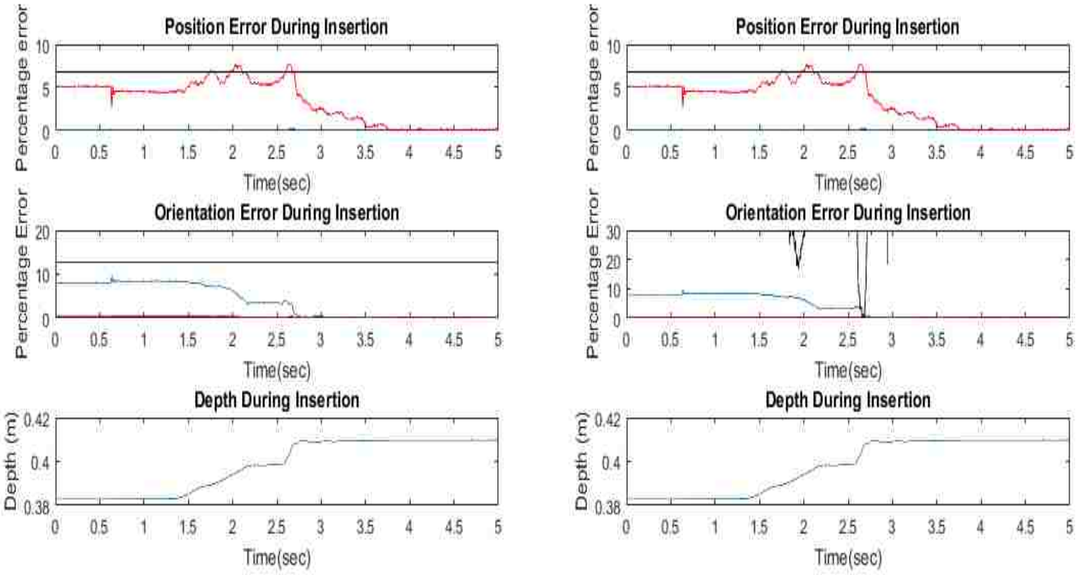

(a) Whitney Model

(b) KFC Model

Figure 7.14: Key insertion for the KFC-VIC. The top graph is position error, the middle graph orientation error, and the last graph depth of insertion. The red lines correspond the $Y$ and $\theta_Y$ for the top and bottom graphs, respectively. The blue line corresponds to the $Z$ and $\theta_Z$ coordinate. The black lines are the maximum allowable wedging value, Whitney model for (a) and KFC model for (b)

we see the initial insertion force response is similar in both responses. The KFC-VIC is again closer to the insertion model. Both responses settle at a larger value than the Whitney model due to the gravity acting on the key. Finally we also see that the insertion force required for the KFC-VIC is about 3 times as much as the VIC.

These three insertion responses have shown that the KFC model does increase the allowable error for successful insertion when the velocity is large enough for the quasi-static assumption to break down. We saw that at lower velocities, where the quasi-static assumption can remain true, the Whitney model is a more accurate wedging model. The issue with increasing the velocity during insertion is that all three KFC-VIC responses have produced larger, but comparable, errors than the normal velocity impedance controller method. We also see that the KFC-VIC requires a much larger

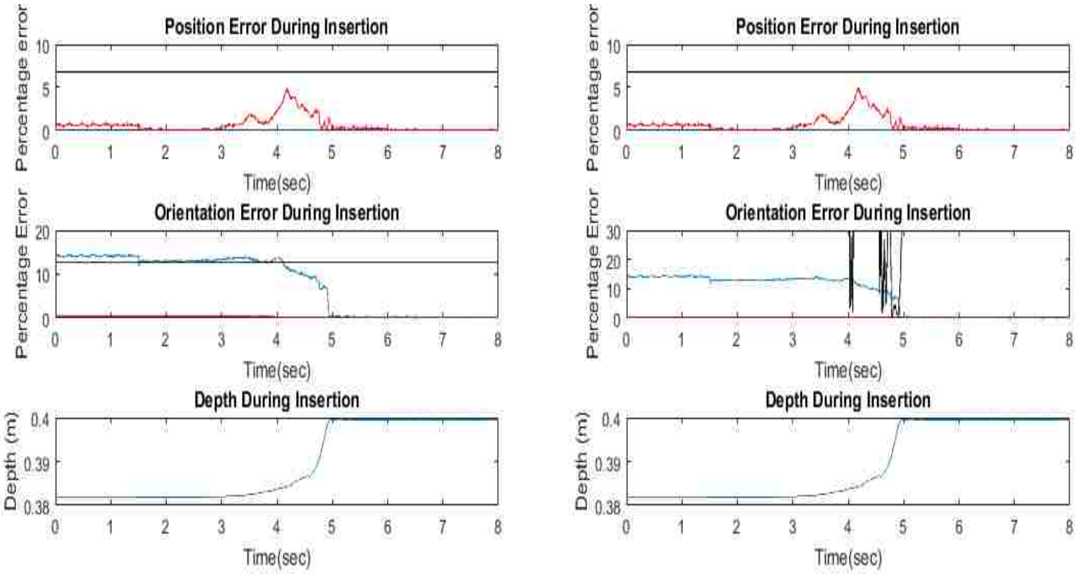

(a) Whitney Model

(b) KFC Model

Figure 7.15: Key insertion for the VIC. The top graph is position error, the middle graph orientation error, and the last graph depth of insertion. The red lines correspond the $Y$ and $\theta_Y$ for the top and bottom graphs, respectively. The blue line corresponds to the $Z$ and $\theta_Z$ coordinate. The black lines are the maximum allowable wedging value, Whitney model for (a) and KFC model for (b)

insertion force than the standard insertion method. This increased insertion force can cause the position based impedance controller to become unstable. From these results we see that the KFC model does increase the allowable orientation error to prevent wedging. We also saw that increasing the velocity will decrease the jamming parameter but any compliance controller will be enough to prevent jamming. In turn, using the kinetic friction cone compliance model for insertion will provide more reliable insertions with the larger threshold for orientation error.

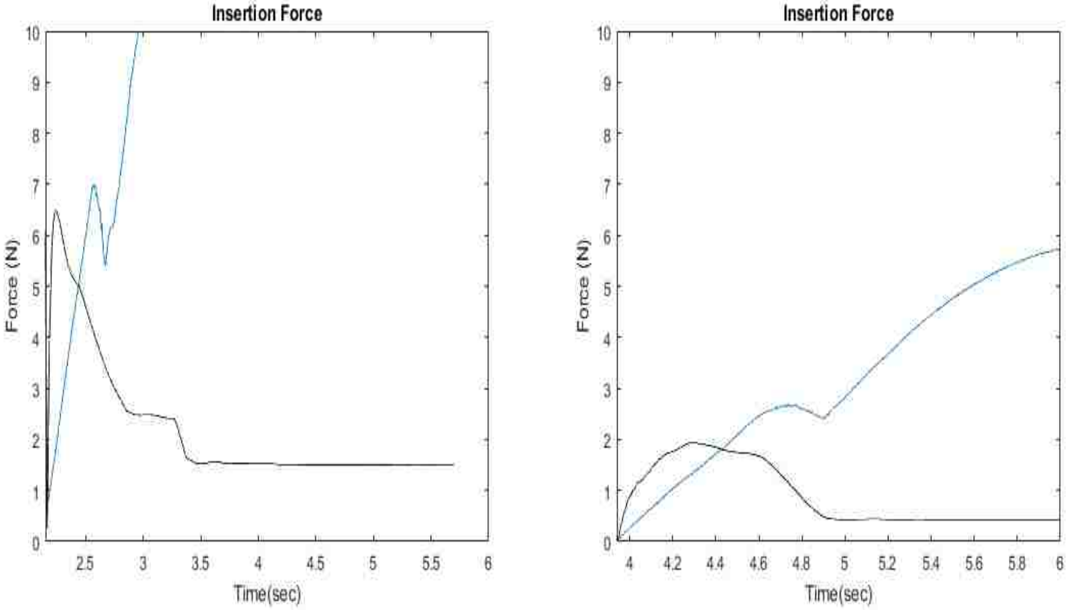

(a) KFC-VIC

(b) Velocity Impedance Controller

Figure 7.16: Key insertion force. The black line is the modeled insertion force while blue line is the actual response.

## 7.3 Summary

From the KFC model, we saw that at velocities where $\mu F_X < \mu_s v$ the KFC model better predicts the orientation tolerance for wedging. At velocities below this threshold we saw that the Whitney model was reliable and better modeled the orientation tolerance. This is due to the fact that at these lower velocities we can use the quasi-static assumption. We also saw that the jamming tolerance would decrease as we increased the insertion velocities but this was never an issue as our compliance controllers effectively prevent jamming.

We noticed that the KFC-VIC insertion force response was more similar to the Whitney model than the response of the VIC. The main difference is that all of the insertion forces from the KFC-VIC are much larger than the insertion forces from the VIC.

From these results we saw that the KFC-VIC provides a closer insertion profile to what we expect. We also saw that the KFC-VIC has faster insertions than the VIC. The issue with the KFC-VIC is that it also generates larger position and pose errors than the VIC. The KFC-VIC also demands higher insertion forces than the VIC. From these results the benefit to using the KFC-VIC is that the insertion forces will be closer to the expected value and that the insertions will be faster.

From the kinetic friction cone model results, we saw that as we increase the velocity we need to increase the lateral force to ensure we have a large enough orientation tolerance. Regarding the position impedance controller we know that increasing this lateral force during insertion will likely cause it to become unstable. We did see that the position impedance controller has the smaller initial errors than the VIC. This implies that the position impedance controller is a preferable impedance controller to use for insertions at lower velocities where the Whitney model is still accurate. However, for high speed insertions, which are clearly advantageous, the KFC-VIC is the preferred controller due to its insertion and compliance model.

From these results we see that using the kinetic friction cone model for insertion modeling improves the accuracy in the allowable wedging and jamming for the insertion. We saw that this model falls apart when $\mu F_X > \mu_s v$ and the Whitney model is the better insertion model at these lower velocities. We also saw that the kinetic friction cone compliance controller, KFC-VIC, improves the insertion force and the rate of insertion. However, we saw an increase in position and pose error and that the insertion requires a larger insertion force than the velocity impedance controller.

# Chapter 8

# Conclusion

In this thesis we introduced a new compliance controller to rival the well-known position impedance controller. We compared the stability of the two controllers and demonstrated the response of both controllers with the inclusion of a vision controller to improve both impedance controllers accuracy. We then tested both controllers' response to various insertion geometries in various configurations. While the position impedance controller has the faster and slightly more accurate response at the same stiffness values as the velocity impedance controller, the velocity impedance controller has a larger range of stability with respect to  higher stiffness values . The velocity impedance controller also stays stable when interacting with high stiffness environments. During the insertion experiments we saw the limitations of using the position impedance controller at higher stiffness values with respect to stability.

We also introduced the idea of kinetic friction cone compliance model to improve upon insertions for the velocity impedance controller. We saw that the velocity impedance controller was capable of using the kinetic friction model due to its larger range of stability, whereas the position impedance controller would become unstable. This is because of the larger insertions forces required for the kinetic friction cone model which was found to be three to fives times larger than the normal insertion force. We saw that KFC-VIC was capable of successful insertions for errors that would cause wedging. From these results we can conclude that the proposed velocity based visual impedance controller is a viable compliance controller with the benefit of having more stability at higher stiffness values than the position impedance controller.

Another important aspect of the velocity based visual impedance controller is that the compliance can also be controlled using the damping parameters. These damping control responses were not explored in this thesis work since the position impedance controller was not able to reliably vary these parameters. As we needed to compare the improvements using the velocity impedance controller over using the position based impedance controller we needed to compare the two controllers using the same compliance values. Since this work has shown the difference of the velocity and position based impedance controllers while using similar parameters, future research would look at the improvement of the compliance model by including the damping response into the model. By including the damping as an active force into the compliance model we can further extend the kinetic friction cone compliance model and model additional dynamic insertion forces. By doing this it may be possible to develop a dynamic controllable object insertion model.

# References

[1] N. Andreff, R. Horaud, and B. Espiau. On-line hand-eye calibration. In *Proceedings. Second International Conference on 3-D Digital Imaging and Modeling,*, pages 430–436, 1999.

[2] S. Babaci, Y. Amirat, J. Pontnau, and C. Francois. Fuzzy adaptation impedance of a 6 dof parallel robot: application to peg in hole insertion. In *Fuzzy Systems, 1996., Proceedings of the Fifth IEEE International Conference on*, volume 3, pages 1770–1776 vol.3, Sep 1996.

[3] A. Becker, C. Ertel, and J. McLurkin. Crowdsourcing swarm manipulation experiments: A massive online user study with large swarms of simple robots. In *2014 IEEE International Conference on Robotics and Automation (ICRA)*, pages 2825–2830, May 2014.

[4] F. Chaumette. Visual servoing. In K. Ikeuchi, editor, *Computer Vision: A Reference Guide*, pages 869–874. Springer, 2014.

[5] Chao-Jen Chen, Ming-Yang Cheng, and Ke-Han Su. Observer-based impedance control and passive velocity control of power assisting devices for exercise and rehabilitation. In *Industrial Electronics Society, IECON 2013 - 39th Annual Conference of the IEEE*, pages 6502–6507, Nov 2013.

[6] M. Erdmann. A configuration space friction cone. In *Intelligent Robots and Systems '91. 'Intelligence for Mechanical Systems, Proceedings IROS '91. IEEE/RSJ International Workshop on*, pages 455–460 vol.2, Nov 1991.

[7] B. Espiau, F. Chaumette, and Patrick Rives. A new approach to visual servoing in robotics. *Robotics and Automation, IEEE Transactions on*, 8(3):313–326, 1992.

[8] S. E. Everett, T. F. Chan, and R. V. Dubey. Diagonalization of telerobotic hand controller impedance for accurate force and velocity transmission. In *Robotics*

*and Automation, 1997. Proceedings., 1997 IEEE International Conference on*, volume 3, pages 2198–2203 vol.3, Apr 1997.

[9] Cheng Gao, Xingzhe Piao, and Weiyan Tong. Optimal motion control for ibvs of robot. In *Intelligent Control and Automation (WCICA), 2012 10th World Congress on*, pages 4608–4611, July 2012.

[10] M. Gendrin, J. Y. Gauthier, and X. Lin-Shi. An impedance control using a finite control set model predictive controller. In *2015 IEEE International Symposium on Predictive Control of Electrical Drives and Power Electronics (PRECEDE)*, pages 85–90, Oct 2015.

[11] M. Gilli and Pastorelli S. Lumia, R. Precision robotic assembly using attractive regions. In *International Journal of Recent Advances in Mechanical Engineering*, volume 3, pages 109–128, August 2014.

[12] K. P. Hawkins, S. Bansal, N. N. Vo, and A. F. Bobick. Anticipating human actions for collaboration in the presence of task and sensor uncertainty. In *2014 IEEE International Conference on Robotics and Automation (ICRA)*, pages 2215–2222, May 2014.

[13] C Ho, C Basdogan, and M Srinivasan. Efficient point-based rendering techniques for haptic display of virtual objects. *Presence*, 8(5):477–491, Oct 1999.

[14] N. Hogan. Impedance control: An approach to manipulation. In *American Control Conference, 1984*, pages 304–313, June 1984.

[15] Seung kook Yun. Compliant manipulation for peg-in-hole: Is passive compliance a key to learn contact motion? In *Robotics and Automation, 2008. ICRA 2008. IEEE International Conference on*, pages 1647–1652, May 2008.

[16] D. Kotake, S. Uchiyama, and H. Yamamoto. A marker calibration method utilizing a priori knowledge on marker arrangement. In *Mixed and Augmented Reality, 2004. ISMAR 2004. Third IEEE and ACM International Symposium on*, pages 89–98, Nov 2004.

[17] X. Lamy, F. Colledani, and P. O. Gutman. Identification and experimentation of an industrial robot operating in varying-impedance environments. In *Intelligent Robots and Systems (IROS), 2010 IEEE/RSJ International Conference on*, pages 3138–3143, Oct 2010.

[18] F. Lange, M. Frommberger, and G. Hirzinger. Impedance-based smoothing for visual servoing along edges. In *Joint Conference on Roboticvs*, January 2006.

[19] B. Lara, K. Althoefer, and L.D. Seneviratne. Automated robot-based screw insertion system. In *Industrial Electronics Society, 1998. IECON '98. Proceedings of the 24th Annual Conference of the IEEE*, volume 4, pages 2440–2445 vol.4, Aug 1998.

[20] D. A. Lawrence. Impedance control stability properties in common implementations. In *Robotics and Automation, 1988. Proceedings., 1988 IEEE International Conference on*, pages 1185–1190 vol.2, Apr 1988.

[21] M. Lendermann, B. R. P. Singh, F. Stuhlenmiller, P. Beckerle, S. Rinderknecht, and P. V. Manivannan. Comparison of passivity based impedance controllers without torque-feedback for variable stiffness actuators. In *2015 IEEE International Conference on Advanced Intelligent Mechatronics (AIM)*, pages 1126–1131, July 2015.

[22] V. Lippiello, B. Siciliano, and L. Villani. A position-based visual impedance control for robot manipulators. In *Robotics and Automation, 2007 IEEE International Conference on*, pages 2068–2073, April 2007.

[23] A.R Locks. Cylinder locks, 2015.

[24] B. Maldonado, M. Mendoza, I. Bonilla, and I. Reyna-Gutirrez. Stiffness-based tuning of an adaptive impedance controller for robot-assisted rehabilitation of upper limbs. In *2015 37th Annual International Conference of the IEEE Engineering in Medicine and Biology Society (EMBC)*, pages 3578–3581, Aug 2015.

[25] M.T. Mason. *Complaint Motion*. MIT Press, 1983.

[26] Wim Meeussen, M. Wise, S. Glaser, S. Chitta, C. McGann, P. Mihelich, E. Marder-Eppstein, M. Muja, Victor Eruhimov, T. Foote, J. Hsu, R.B. Rusu, B. Marthi, G. Bradski, K. Konolige, B. Gerkey, and E. Berger. Autonomous door opening and plugging in with a personal robot. In *Robotics and Automation (ICRA), 2010 IEEE International Conference on*, pages 729–736, May 2010.

[27] D. Meike, M. Pellicciari, and G. Berselli. Energy efficient use of multirobot production lines in the automotive industry: Detailed system modeling and optimization. *IEEE Transactions on Automation Science and Engineering*, 11(3):798–809, July 2014.

[28] TH. Meitinger and F. Pfeiffer. The spatial peg-in-hole problem. In *IEEE/RSJ Cong. on Intelligent Robots & Systems*, pages 54–59, 1995.

[29] N. Melder and W.S. Harwin. Improved rendering for multi-finger manipulation using friction cone based god-objects. In *Proc. Eurohaptics Conference*, pages 82–85, 2003.

[30] N. Melder and W.S. Harwin. Extending the friction cone algorithm for arbitrary polygon based haptic objects. In *Haptic Interfaces for Virtual Environment and Teleoperator Systems, 2004. HAPTICS '04. Proceedings. 12th International Symposium on*, pages 234–241, March 2004.

[31] H.B Morgenbesser and M.A. Srinivasan. Force shading and bump mapping using the friction cone algorithm. In *Proceedings of the ASME Dynamics Systems and Control Division*, volume 58, pages 407–412, 1996.

[32] Y. Nakabo and M. Ishikawa. Visual impedance using 1 ms visual feedback system. In *Robotics and Automation, 1998. Proceedings. 1998 IEEE International Conference on*, volume 3, pages 2333–2338 vol.3, May 1998.

[33] B.J. Nelson, J.D. Morrow, and P.K. Khosla. Improved force control through visual servoing. In *American Control Conference, Proceedings of the 1995*, volume 1, pages 380–386 vol.1, Jun 1995.

[34] V. Nevarez and R. Lumia. Image jacobian estimation using structure from motion on a centralized point. In *Intelligent Robots and Systems (IROS 2014), 2014 IEEE/RSJ International Conference on*, pages 773–778, Sept 2014.

[35] E. Nichols and W. Franklin. *The Elements of Physics.* Macmillan, 1898.

[36] R. Oboe and D. Pilastro. Stability analysis of a non-linear adaptive impedance controller for rehabilitation purposes. In *Mechatronics (ICM), 2015 IEEE International Conference on*, pages 454–459, March 2015.

[37] S. Oh and Y. Hori. Fractional order impedance control by particle swarm optimization. In *Control, Automation and Systems, 2008. ICCAS 2008. International Conference on*, pages 1936–1941, Oct 2008.

[38] M.D. O'Leary, C. Simone, T. Washio, K. Yoshinaka, and A.M. Okamura. Robotic needle insertion: effects of friction and needle geometry. In *Robotics and Automation, 2003. Proceedings. ICRA '03. IEEE International Conference on*, volume 2, pages 1774–1780 vol.2, Sept 2003.

[39] F. Parietti and H. H. Asada. Supernumerary robotic limbs for aircraft fuselage assembly: Body stabilization and guidance by bracing. In *2014 IEEE International Conference on Robotics and Automation (ICRA)*, pages 1176–1183, May 2014.

[40] F. Parietti, K. Chan, and H. H. Asada. Bracing the human body with supernumerary robotic limbs for physical assistance and load reduction. In *2014 IEEE International Conference on Robotics and Automation (ICRA)*, pages 141–148, May 2014.

[41] M. Pelletier and M. Doyon. On the implementation and performance of impedance control on position controlled robots. In *Robotics and Automation, 1994. Proceedings., 1994 IEEE International Conference on*, pages 1228–1233 vol.2, May 1994.

[42] M.A. Peshkin. Programmed compliance for error corrective assembly. *Robotics and Automation, IEEE Transactions on*, 6(4):473–482, Aug 1990.

[43] J. Pomares, G. J. Garcia, L. Paya, and F. Torres. Adaptive visual servoing and force control fusion to track surfaces. In *Proceedings of the 2005 WSEAS International Conference on Dynamical Systems and Control*, volume 5, January 2006.

[44] J. Pomares, G. J. Garcia, and F. Torres. Impedance control for fusing multisensorial systems in robotic manipulation tasks. In *Proceedings of the 2005 WSEAS International Conference on Dynamical Systems and Control*, pages 357–362, Stevens Point, Wisconsin, USA, 2005. World Scientific and Engineering Academy and Society (WSEAS).

[45] Craig J. J. Raibert, M. H. Hybrid position/force control of manipulators. In *ASME Journal of Dynamic Systems Measurement and Control*, volume 102, pages 126–133, 1981.

[46] C. Richard, M.R. Cutkosky, and K. MacLean. Friction identification for haptic display. In *Proceedings of the ASME Dynamics Systems and Control Division*, volume 67, November 1999.

[47] L. Roveda, F. Vicentini, N. Pedrocchi, F. Braghin, and L. M. Tosatti. Impedance shaping controller for robotic applications in interaction with compliant environments. In *Informatics in Control, Automation and Robotics (ICINCO), 2014 11th International Conference on*, volume 02, pages 444–450, Sept 2014.

[48] Kevin Ruybal. A variable compliance controller for cooperative vision guided robotic assembly. Master's thesis, University of New Mexico. Dept. of Mechanical Engineering, May 2011.

[49] J.D. Schutter and H.V Brussel. Compliant robot motion i. a formalism for specifying complaint motion tasks. In *International Journal of Robotics Research*, volume 7, pages 3–17, August 1988.

[50] Y. Shirai and H. Inoue. Guiding a robot by visual feedback in assembling tasks. *Pattern Recognition*, 5(2):99 – 108, 1973.

[51] J. Simmon. *Force Feedback in Robot Assembly Using an Active Wrist with Adaptive Compliance*. PhD thesis, Univ. Leuven (Belgium), Dept. of Mechanical Engineering, 1980.

[52] R.Y. Tsai. A versatile camera calibration technique for high-accuracy 3d machine vision metrology using off-the-shelf tv cameras and lenses. *Robotics and Automation, IEEE Journal of*, 3(4):323–344, August 1987.

[53] T. Tsumugiwa, R. Yokogawa, and K. Hara. Variable impedance control with virtual stiffness for human-robot cooperative peg-in-hole task. In *Intelligent Robots and Systems, 2002. IEEE/RSJ International Conference on*, volume 2, pages 1075–1081 vol.2, 2002.

[54] T. Watanabe, K. Harada, Zhongwei Jiang, and T. Yoshikawa. Object manipulation under hybrid active/passive closure. In *Robotics and Automation, 2005. ICRA 2005. Proceedings of the 2005 IEEE International Conference on*, pages 1013–1020, April 2005.

[55] Daniel E. Whitney. Historical perspective and state of the art in robot force control. In *Robotics and Automation. Proceedings. 1985 IEEE International Conference on*, volume 2, pages 262–268, Mar 1985.

[56] S. Xiao and Y. Li. Visual servo feedback control of a novel large working range micro manipulation system for microassembly. *Journal of Microelectromechanical Systems*, 23(1):181–190, Feb 2014.

[57] Q. Xu. Robust impedance control of a compliant microgripper for high-speed position/force regulation. *IEEE Transactions on Industrial Electronics*, 62(2):1201–1209, Feb 2015.

[58] Q. Zhang and R. Pless. Extrinsic calibration of a camera and laser range finder (improves camera calibration). In *Intelligent Robots and Systems, 2004. (IROS 2004). Proceedings. 2004 IEEE/RSJ International Conference on*, volume 3, pages 2301–2306 vol.3, Sept 2004.

[59] Zhengyou Zhang. Flexible camera calibration by viewing a plane from unknown orientations. In *Computer Vision, 1999. The Proceedings of the Seventh IEEE International Conference on*, volume 1, pages 666–673 vol.1, 1999.

[60] Zhengyou Zhang. A flexible new technique for camera calibration. *Pattern Analysis and Machine Intelligence, IEEE Transactions on*, 22(11):1330–1334, Nov 2000.

[61] Zhuyingqingfen. Firction approximation, 2014.